

Radio Wave Propagation and Wireless Channel Modeling 2013

Guest Editors: Bo Ai, Thomas Küerner, César Briso Rodríguez,
and Hsiao-Chun Wu





Radio Wave Propagation and Wireless Channel Modeling 2013

International Journal of Antennas and Propagation

Radio Wave Propagation and Wireless Channel Modeling 2013

Guest Editors: Bo Ai, Thomas Küerner, César Briso Rodríguez,
and Hsiao-Chun Wu



Copyright © 2014 Hindawi Publishing Corporation. All rights reserved.

This is a special issue published in "International Journal of Antennas and Propagation." All articles are open access articles distributed under the Creative Commons Attribution License, which permits unrestricted use, distribution, and reproduction in any medium, provided the original work is properly cited.

Editorial Board

M. Ali, USA
Charles Bunting, USA
Felipe Cátedra, Spain
Dau-Chyrh Chang, Taiwan
Deb Chatterjee, USA
Z. N. Chen, Singapore
Michael Yan Wah Chia, Singapore
Shyh-Jong Chung, Taiwan
Lorenzo Crocco, Italy
Tayeb A. Denidni, Canada
Antonije R. Djordjevic, Serbia
Karu P. Esselle, Australia
Miguel Ferrando, Spain
Vincenzo Galdi, Italy
Wei Hong, China
Hon Tat Hui, Singapore
Tamer S. Ibrahim, USA
Nemai Karmakar, Australia
Se-Yun Kim, Republic of Korea
Ahmed A. Kishk, Canada

Selvan T. Krishnasamy, India
Tribikram Kundu, USA
Francisco Falcone Lanas, Spain
Ju-Hong Lee, Taiwan
Byungje Lee, Republic of Korea
L. Li, Singapore
Yilong Lu, Singapore
Atsushi Mase, Japan
Andrea Massa, Italy
Giuseppe Mazzeola, Italy
Derek McNamara, Canada
C.Mecklenbräuker, Austria
Michele Midrio, Italy
Mark Mirotznik, USA
Ananda Mohan, Australia
P. Mohanan, India
Pavel Nikitin, USA
A. D. Panagopoulos, Greece
Matteo Pastorino, Italy
Massimiliano Pieraccini, Italy

Sadasiva M. Rao, USA
Sembiam R. Rengarajan, USA
Ahmad Safaai-Jazi, USA
Safieddin Safavi-Naeini, Canada
Magdalena Salazar-Palma, Spain
Stefano Selleri, Italy
Zhongxiang Shen, Singapore
John J. Shynk, USA
Mandeep Singh Jit Singh, Malaysia
Seong-Youp Suh, USA
Parveen Wahid, USA
Yuanxun Ethan Wang, USA
Daniel S. Weile, USA
Tat Soon Yeo, Singapore
Young Joong Yoon, Korea
Jong-Won Yu, Republic of Korea
Wenhua Yu, USA
Anping Zhao, China

Contents

Radio Wave Propagation and Wireless Channel Modeling 2013, Bo Ai, Thomas Kürner, César Briso Rodríguez, and Hsiao-Chun Wu
Volume 2014, Article ID 670564, 2 pages

Line-of-Sight Obstruction Analysis for Vehicle-to-Vehicle Network Simulations in a Two-Lane Highway Scenario, Taimoor Abbas and Fredrik Tufvesson
Volume 2013, Article ID 459323, 9 pages

Modeling, Real-Time Estimation, and Identification of UWB Indoor Wireless Channels, Mohammed M. Olama, Seddik M. Djouadi, Yanyan Li, and Aly Fathy
Volume 2013, Article ID 467670, 8 pages

A TD-LTE Based Non-WSSUS Vehicle-to-Vehicle Channel Model, Yan Li, Bo Ai, Xiang Cheng, Siyu Lin, and Zhangdui Zhong
Volume 2013, Article ID 103461, 8 pages

A Novel Transformation Electromagnetic Theory-Based Coverage Optimization Method for Wireless Network, Yuanxuan Li, Gang Zhu, Siyu Lin, Ke Guan, and Yan Li
Volume 2013, Article ID 896906, 8 pages

Propagation and Wireless Channel Modeling Development on Wide-Sense Vehicle-to-X Communications, Wenyi Jiang, Ke Guan, Zhangdui Zhong, Bo Ai, Ruisi He, Binghao Chen, Yuanxuan Li, and Jia You
Volume 2013, Article ID 981281, 11 pages

Improved Pilot-Aided Channel Estimation for MIMO-OFDM Fading Channels, J. Mar, Chi-Cheng Kuo, and M. B. Basnet
Volume 2013, Article ID 978420, 10 pages

Editorial

Radio Wave Propagation and Wireless Channel Modeling 2013

Bo Ai,¹ Thomas Kürner,² César Briso Rodríguez,³ and Hsiao-Chun Wu⁴

¹ State Key Lab of Rail Traffic Control and Safety, Beijing Jiaotong University, Beijing 100044, China

² Institute of Telecommunications, Technical University of Braunschweig, 38106 Braunschweig, Germany

³ Institute of Telecommunications, Technical University of Madrid, 28031 Madrid, Spain

⁴ Department of Electrical and Computer Engineering, Louisiana State University, Baton Rouge, LA 70803, USA

Correspondence should be addressed to Bo Ai; aibo@ieee.org

Received 1 January 2014; Accepted 1 January 2014; Published 9 February 2014

Copyright © 2014 Bo Ai et al. This is an open access article distributed under the Creative Commons Attribution License, which permits unrestricted use, distribution, and reproduction in any medium, provided the original work is properly cited.

Mechanisms about radio wave propagation are the basis for the research of wireless channel modeling. Typical wireless channel models for typical scenarios are of great importance to the physical and higher layers design. With the development of some new techniques such as vehicle-to-vehicle communications, wireless relay technique, wireless chip technique, wireless body area network (WBAN), and massive multi-input multi-output (MIMO) technique, novel wireless channel models should be developed to cater for these new situations.

Unlike the traditional views, a more general concept of wide-sense V2X (WSV2X) communications was proposed in the article titled “*Propagation and wireless channel modeling development on wide-sense vehicle-to-X communications.*” WSV2X includes not only V2V and vehicle-to-infrastructure (V2I) communications, but also train-to-train (T2T) and train-to-infrastructure (T2I) communications. The review of propagation scenarios, wireless channel features, the channel standardization, and modeling philosophies related to WSV2X is presented in this paper to give some rough inspirations of the joint research of the V2X and T2X scenarios.

Different from the traditional assumption that the wireless channel is wide-sense stationary uncorrelated scattering (WSSUS), Dr. Y. Li et al. propose a non-WSSUS channel model for V2V communication systems. The model is based on the tapped-delay line (TDL) structure and considers the correlation between taps both in amplitude and phase. Using the relationship between the correlation coefficients of complex Gaussian, Weibull, and uniform random variables (RVs), the model is used to reflect the non-WSSUS properties of V2V channels.

As for the research on the vehicular ad hoc networks (VANETs), the impact of vehicles as obstacles has been neglected. In the article titled “*Line-of-sight obstruction analysis for vehicle-to-vehicle network simulations in a two-lane highway scenario.*” Dr. T. Abbas et al. considered the LOS obstruction caused by other vehicles in a highway scenario. A car-following model is used to characterize the motion of the vehicles driving in the same direction on a two-lane highway. The position of each vehicle is updated by using car following rules together with the lane-changing rules for the forward motion. The presented traffic mobility model together with the shadow fading path loss model takes into account the impact of LOS obstruction on the total received power in the multiple-lane highway scenarios.

Dr. M. M. Olama et al. talk about the wireless channel modeling for ultrawideband (UWB) indoor wireless channels. In their article, a general scheme for extracting mathematical UWB indoor channel models from the noisy received signal measurements is presented. The UWB channel models are represented in a stochastic state-space form with high approximation to the measured data.

As for the key techniques related to wireless channels, Dr. Y. Li et al. present a special rectangular cloak design based on the transformation electromagnetic (TE) technique to improve the signal coverage under serious wireless channel conditions. TE technique paves a new way for controlling the propagation direction of the radio signal. A cloak covering the surface of the obstacle is designed to improve the coverage performance in a shadow area. The material parameters of the cloak are calculated by the TE technique. This scheme can

be used to improve the reliability of the radio coverage in a shadow area.

Dr. J. Mar et al. present a pilot-aided channel estimation scheme to enhance the channel estimation accuracy under multiple-input multiple-output orthogonal frequency division multiplexing (MIMO-OFDM) fading channels. Based on the adaptive path number selection mechanism, the number of paths can be scalable and adaptively changed with the characteristics of MIMO-OFDM fading channels. The fine channel estimation formulas for all data subcarriers can be derived.

By compiling these papers, we hope to enrich our readers and researchers with respect to these particularly common, yet usually highly treatable, wireless channel modeling techniques and the channel models.

Bo Ai
Thomas Kürner
César Briso Rodríguez
Hsiao-Chun Wu

Research Article

Line-of-Sight Obstruction Analysis for Vehicle-to-Vehicle Network Simulations in a Two-Lane Highway Scenario

Taimoor Abbas and Fredrik Tufvesson

Department of Electrical and Information Technology, Lund University, P.O. Box 118, 22 100 Lund, Sweden

Correspondence should be addressed to Taimoor Abbas; taimoor.abbas@eit.lth.se

Received 12 July 2013; Revised 5 November 2013; Accepted 23 November 2013

Academic Editor: Thomas Kürner

Copyright © 2013 T. Abbas and F. Tufvesson. This is an open access article distributed under the Creative Commons Attribution License, which permits unrestricted use, distribution, and reproduction in any medium, provided the original work is properly cited.

In vehicular ad-hoc networks (VANETs) the impact of vehicles as obstacles has largely been neglected in the past. Recent studies have reported that the vehicles that obstruct the line-of-sight (LOS) path may introduce 10–20 dB additional loss, and as a result reduce the communication range. Most of the traffic mobility models (TMMs) today do not treat other vehicles as obstacles and thus cannot model the impact of LOS obstruction in VANET simulations. In this paper the LOS obstruction caused by other vehicles is studied in a highway scenario. First a car-following model is used to characterize the motion of the vehicles driving in the same direction on a two-lane highway. Vehicles are allowed to change lanes when necessary. The position of each vehicle is updated by using the car-following rules together with the lane-changing rules for the forward motion. Based on the simulated traffic a simple TMM is proposed for VANET simulations, which is capable to identify the vehicles that are in the shadow region of other vehicles. The presented traffic mobility model together with the shadow fading path-loss model can take into account the impact of LOS obstruction on the total received power in the multiple-lane highway scenarios.

1. Introduction

Vehicle-to-vehicle (V2V) communication is an emerging technology that has been recognized as a key communication paradigm for safety and infotainment applications in future intelligent transportation systems (ITS). In recent years extensive research efforts have been made to design reliable and fault tolerant vehicular ad-hoc network (VANET) communication protocols. However, the propagation channel is one of the key performance limiting factor which is not yet completely understood [1]; several aspects such as the impact of antenna placement on vehicles [2] and line-of-sight obstruction by other vehicles on V2V communication have largely been neglected in the past. In [3, 4], it is stated that a vehicle that obstructs the LOS path between the transmitter (TX) and receiver (RX) vehicle may introduce 10 dB additional loss in the received power and as a result cause 3 times reduced communication range. This additional power loss can increase up to 20 dB if the obstructing vehicle is tall and close to the RX vehicle [5].

Several network simulators suitable for VANET simulations exist today, for example, ns-2 [6], OMNet++ [7], ns-3 [8], and JiST/SWANS [9]. These simulators are different from each other in terms of run-time performance and memory usage [10]. Most of these simulators do not consider the impact of neighboring vehicles on the packet reception probabilities. To evaluate this impact in these simulators, a traffic mobility model (TMM) should be implemented having at least the ability to identify and categorize the vehicles into the following groups:

- (i) line-of-sight (LOS)—when the TX vehicle has optical line-of-sight from the RX vehicle;
- (ii) obstructed-line-of-sight (OLOS)—when the optical LOS between the TX and RX is obstructed by another vehicle.

In the VANET simulators the role of the TMM is very vital in order to perform a realistic system simulations. Today there are a number of traffic models that can be used in the VANET simulators. Some of them are very

advanced but equally complex, for example, Simulation of Urban Mobility (SUMO) [11], which can be implemented in any of the aforementioned VANET simulators. However, using such an advanced mobility model is not desired if the purpose of the VANET simulations is to perform a simple system analysis. Therefore, for basic packet level performance evaluations less detailed but realistic traffic flow models, for example, the optimal velocity (OV) car-following model without or with the lanechange capabilities, [12, 13], respectively, can be used in the VANET simulators.

In this paper a TMM is discussed that is capable to identify vehicles being in LOS and OLOS. The TMM is implemented in MATLAB in which the car-following model, which is used to formulate the forward motion of vehicles, is used. The car-following model is of low complexity but gives a realistic traffic flow. The interaction between the lanes is also taken into account by allowing vehicles to perform lane changes when necessary conditioned that the considered vehicles fulfill certain lane change requirements. The model is used to identify the vehicles being in LOS and OLOS from the TX at each time instant. Moreover, the instantaneous position, headway distance, state, distance traveled in each state, and number of transitions from one state to another are logged to calculate the probability of vehicles being in the LOS and OLOS states with respect to distance between them. The traffic simulations are performed based on realistic parameters and the results are compared with the measurement results collected during an independent measurement campaign (for details, see [3]).

The main contribution of this paper is a TMM that is straight-forward to integrate with VANET simulators in order to study the impact of vehicles as obstruction. We do not derive the TMM itself, but we adapt models in the literature to be used for VANET simulations. As mentioned above the TMM is capable to distinguish vehicles that are in LOS and OLOS states on a two-lane highway where the traffic flow is generated by using the lanechanging rules in the car-following model. In addition to that, analytical expressions to find the packet reception probability (PRP) are also provided. The PRP can easily be estimated by utilizing the probability of being in LOS or in OLOS calculated from the TMM into the LOS/OLOS path-loss model proposed in [3]. Finally, the corresponding results for PRP are calculated and compared for three different V2V channel models for highway scenario: (1) the LOS only path-loss model by Karedal et al. [14], (2) the Nakagami-m based path-loss and fading model by Cheng et al. [15], and (3) the LOS/OLOS path-loss model in [3].

The remainder of the paper is organized as follows; the TMM including the car-following model and lane change rules are discussed in Section 2. Section 3 explains the method to distinguish between the LOS and OLOS situations. The simulation setup for the traffic mobility model and probabilities of vehicles being in LOS and OLOS states are given in Section 4. In Section 5 the analytical expressions for packet reception probabilities are analyzed for completeness, while in Section 6 conclusions are given.

2. Traffic Mobility Model

In recent years, a number of research efforts have been made to understand and model complex traffic phenomena by using the concepts from statistical physics [16]. Experimental studies have also been performed to analyze traffic and lane change behaviors [17]. Among all these models, the car-following model is one of the most frequently used models to describe vehicle motion. The car-following model is capable of describing real traffic as it takes into account the velocities, headway distances, relative speeds, and the attitude of the drivers to model the traffic flow. The optimal velocity (OV) car-following model, first introduced by Bando et al. [12], was extended for two-lanes in [13]. Tang et al. [18] further extended the model to incorporate the effect of potential lane changing and analyzed the traffic flow stability. The car-following model for two-lane traffic flow is discussed underneath, in which the lane changing is also allowed. The model is modified such that the probabilities of vehicles being in LOS and OLOS situations can be obtained using simple geometric manipulations that can further be integrated into the VANET simulators.

2.1. The Car-Following Model. Consider a highway with two lane traffic in each direction of travel and assume that the vehicles in each lane move along a straight line. Let $l = \{1, 2\}$ be the lane index for the outer (fast) and inner (slow) lanes, respectively. Vehicles in lane l are labeled as $(\dots, n_{l,a-1}, n_{l,a}, n_{l,a+1}, \dots)$, where a is a lane specific vehicle index, their instantaneous positions are $(\dots, x_{l,a-1}(t), x_{l,a}(t), x_{l,a+1}(t), \dots)$, and the headway between any two vehicles moving in the same lane is labeled as $(\dots, \Delta x_{l,a-1}(t), \Delta x_{l,a}(t), \Delta x_{l,a+1}(t), \dots)$ at time instant t , as described in Figure 1. At each time instant t each of the two lanes will be classified as subject-lane or target-lane with respect to each subject vehicle. A subject-lane is the lane where the vehicle $n_{l,a}$ drives, and target-lane is the lane on which the vehicle $n_{l,a}$ intends to drive after the possible lane change.

A microscopic simulation model, the car-following model, is used to describe the movement of vehicles on the same lane. It explains a one-by-one following process of vehicles and incarnate human behaviors which in turn reflects realistic traffic conditions. It has been shown that the car-following model is a better way to model traffic flow compared to the other common traffic-flow models [19]. Tang et al. [13, 18] developed a car-following model for two-lane traffic-flow in the forward direction, expressed as follows:

$$\frac{d^2 x_{l,a}(t)}{dt^2} = \alpha_l \left(V_l \left(\Delta x_{l,a}(t), \Delta x_{l,a}^p(t) \right) - \frac{dx_{l,a}(t)}{dt} \right) + \kappa_l \Delta v_{l,a}(t), \quad (1)$$

where $\Delta v_{l,a}(t)$ is the relative velocity between two vehicles $n_{l,a}$ and $n_{l,a+1}$, $\Delta x_{l,a}^p(t)$ is the distance between the vehicle $n_{l,a}$ and the preceding vehicle in the target-lane, α_l is the driver's sensitivity coefficient, and $\kappa_l = \lambda_l / \tau_l$ is the sensitivity coefficient due to difference in velocity, in the lane l at time instant t , respectively. The delay τ_l is the time delay in

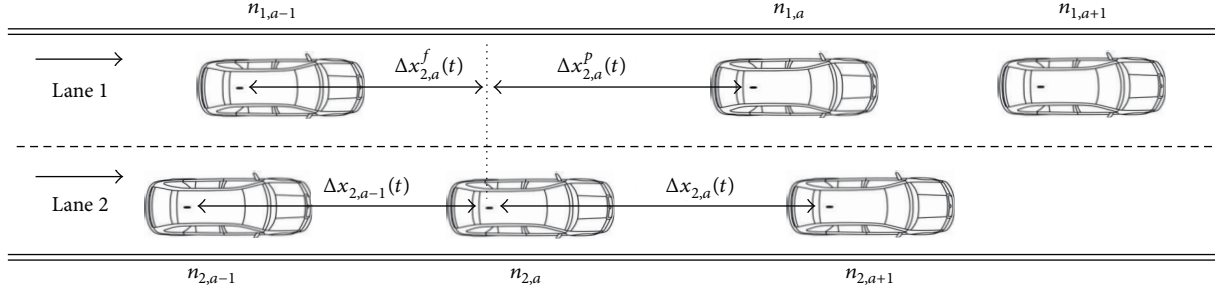


FIGURE 1: The car-following traffic model for two-lane traffic. $\Delta x_{2,a}(t)$, $\Delta x_{2,a-1}(t)$, $\Delta x_{2,a}^p(t)$, and $\Delta x_{2,a}^f(t)$ are the headway distances from the vehicle $n_{2,a}$ to the vehicles $n_{2,a+1}$, $n_{2,a-1}$, $n_{1,a}$, and $n_{1,a-1}$, respectively, where $n_{l,a}$ is vehicle label, l is lane number, and a is lane specific vehicle index.

which a vehicle attains its optimal velocity and $\lambda_l \in (0, 1)$ is the sensitivity factor for the relative velocities which is independent of time, position, and velocity. However, it is assumed that the driving condition is better in the outer (fast) lane 1 compared to the inner (slow) lane 2, and thus $\lambda_1 > \lambda_2$.

The continuous model in (1) can be discretized using forward difference to find the position of vehicle n_l at any time $t + 2\tau_l$ [18] as given below:

$$x_{l,a}(t + 2\tau_l) = x_{l,a}(t + \tau_l) + \tau_l V_l(\Delta \tilde{x}_{l,a}(t)) + \lambda_l \tau_l (x_{l,a}(t + \tau_l) - x_{l,a}(t)). \quad (2)$$

The above equation can also be written in terms of headways as

$$\begin{aligned} \Delta x_{l,a}(t + 2\tau_l) &= \Delta x_{l,a}(t + \tau_l) + \tau_l V_l(\Delta \tilde{x}_{l,a+1}(t)) \\ &\quad - V_l(\Delta \tilde{x}_{l,a}(t)) + \lambda_l \tau_l (x_{l,a+1}(t + \tau_l) - x_{l,a+1}(t)) \\ &\quad - (x_{l,a}(t + \tau_l) - x_{l,a}(t)), \end{aligned} \quad (3)$$

where $V_l(\Delta \tilde{x}_{l,a}(t))$ is the headway induced optimal velocity function (OVF). The OVF is given as follows:

$$\begin{aligned} V_l(\Delta \tilde{x}_{l,a}(t)) &= V_l(\Delta x_{l,a}(t), \Delta x_{l,a}^p(t)) \\ &= \frac{1}{2} v_{l,\max} \left(\tanh(\tilde{x}_{l,a}(t) - d_l^p) + \tanh(d_l^p) \right), \end{aligned} \quad (4)$$

where d_l^p and $v_{l,\max}$ are the minimum safety distance from the preceding vehicle in the target-lane and the maximum velocity in the lane l , respectively. Finally the weighted headways $\tilde{x}_{l,a}(t)$ are defined as

$$\tilde{x}_{l,a}(t) = \beta_1 \Delta x_{l,a} + \beta_2 \Delta x_{l,a}^p(t), \quad (5)$$

where β_1 and β_2 are the weights for the headways from the preceding vehicles in same lane and the target-lane, respectively, and $\beta_1 > \beta_2$ given that $\beta_1 + \beta_2 = 1$. The car

following model previously explained is used to formulate the forward motion of vehicles.

The forward difference equations, (2) and (3), used to find the positions and headways of the vehicles, respectively, do take the driver sensitivity coefficients and sensitivity factor for the relative velocity into account. However, many other factors (e.g., weather condition, road bumps, and driver mood) can also influence the traffic flow. Moreover, the vehicles are assumed to be moving along a straight line, which means no variations along the vertical axis and this is not the case in reality. To summarize, we can say that the generated traffic flow is realistic but due to simplifications it is noise free in the sense that the vehicles follow the center point of the lanes. Hence, it is important to introduce some randomness to make the result of the TMM more realistic, which is done in Section 5 when the TMM is integrated with the LOS/OLOS path-loss model.

2.2. Lane Change Rules. To characterize realistic traffic in a multilane highway scenario it is important to consider interaction between lanes and the lane change activities as it affects stability of the traffic flow. In [18] it is concluded that if lane changes are not allowed then the system has a stable flow, but when the vehicles are allowed to change lanes then the system flow can become metastable or unstable depending upon the frequency of lane change activities.

In our simulator each vehicle is allowed to perform lane changes when necessary, conditioned that the vehicle fulfills all lane change requirements. During a lane change event both the lanes are categorized either as the subject-lane or the target-lane. Whenever a vehicle changes lane from the subject to target-lane it becomes a vehicle in the target-lane, and thus the position, number, and identity of each vehicle in both lanes are updated accordingly. It is assumed that the lane change process is instantaneous, so when a vehicle changes lane its longitudinal location remains the same as it was prior to the lane change.

In [18, 20, 21] several lane changing rules are defined that can either be used independently or all together to model the lane change behavior. The lane-changing rule based on

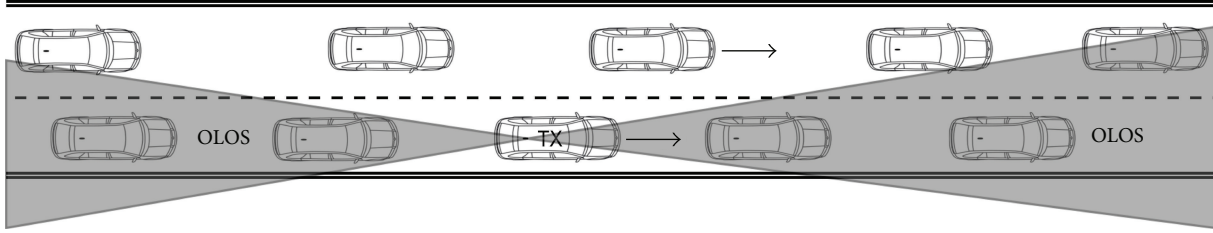


FIGURE 2: Identification of vehicles being in LOS and in OLOS of the TX vehicle; vehicles in the shaded-area are considered to be in OLOS whereas all other vehicles have LOS from the TX.

the incentive and safety criterion defined in [18] states that the vehicle is allowed to change lane only if it fulfills the following three criteria.

- (i) The distance of the vehicle $n_{l,a}$ from the preceding vehicle $n_{l,a+1}$ should be smaller than twice the safety distance d_l^p ; that is,

$$\Delta x_{l,a}(t) < 2d_l^p. \quad (6)$$

- (ii) The distance of the vehicle $n_{l,a}$ from the preceding vehicle in the target-lane should be greater than the distance of the vehicle $n_{l,a}$ from the preceding vehicle $n_{l,a+1}$ in the same lane; that is,

$$\Delta x_{l,a}^p(t) > \Delta x_{l,a}(t). \quad (7)$$

- (iii) Finally the distance $\Delta x_{l,a}$ of the vehicle $n_{l,a}$ from the vehicle in the target-lane following this vehicle $n_{l,a}$ should be greater than the corresponding safety distance of the following vehicles d_l^f ; that is,

$$\Delta x_{l,a}^f(t) > d_l^f. \quad (8)$$

In [22] it is stated that 0.9 s is the minimum legal time-gap during following, which gives the safety distance relative to the velocity of the vehicle. Their measurement results show that the time-gap during following is not fixed but it is relative to the speed of the vehicle and traffic density. Thus, we can say that the safety distance d_l^p and the corresponding safety distance of the following vehicles d_l^f are random parameters which depend on the velocity of the subject vehicle given a minimum time-gap. In general the so-called two-second rule is a rule of thumb to determine the correct following distance; that is, a driver should ideally keep at least two seconds of time-gap from any vehicle that is in front of the subject vehicle.

3. Line-of-Sight Obstruction Analysis

As mentioned before, to date most of the VANET simulators do not consider the impact of line-of-sight obstruction, caused by neighboring vehicles, on the packet reception probabilities. To evaluate this impact in the simulator the TMM is required to identify and label each vehicle as in LOS

or in OLOS situation with respect to TX and RX at each instant t . The identification of vehicles being in LOS or in OLOS states becomes fairly simple as the TMM discussed earlier provides the instantaneous position of each vehicle on the road. Thus, the position information of each vehicle together with some geometric manipulations give the state information of each vehicle being in LOS or in OLOS state as follows.

- (i) Model each vehicle as a screen or a strip with the assumption that each vehicle has the same size.
- (ii) Assumed that the *intended* communication range is a circle of a certain radius, that is, R_c . At each instant t the vehicles that are in this circle are only considered.
- (iii) Vehicles in each lane are assumed to be moving along a straight line. Thus only two vehicles in the same lane, one at the front and one in the back of the TX, will be in the LOS. The rest of the vehicles in the same lane are considered to be in the OLOS state.
- (iv) Draw straight lines starting from the antenna position of the TX vehicle touching the edges of the vehicles in the front and back to the edges of road (see Figure 2). All vehicles that are bounded by these lines are shadowed by other vehicles thus in the OLOS state.
- (v) Vehicles that are not bounded by these lines are analyzed individually to see if they are in LOS or in OLOS from the TX.
- (vi) The identification process is repeated for each vehicle and at each time instant t to find out whether the vehicles are in LOS or in OLOS states with respect to every other vehicle. The state information of each vehicle can then be used either for analytical performance evaluations or for packet level VANET simulations.

4. Simulations and Results

The TMM derived above is implemented in Matlab and simulations are carried out in order to analyze the movement of vehicles over time, their lane changing behavior, and the intensities by which the vehicles change states from LOS-to-OLOS and from OLOS-to-LOS states, respectively. The simulations are performed on a two-lane 14.4 km long circular highway. The circular highway refers to the fact that

any vehicle that departs from one end of the highway, that is, beyond 14.4 km, enters from the other end so that the traffic can flow for infinite amount of time. The simulation parameters are chosen as follows.

For the simulations, the initial positions $x_{l,a}(0)$ and the headways $\Delta x_{l,a}(0)$ of all the vehicles $n_{l,a}$ in lane l for ($a = 1, 2, \dots, N_l$) are determined by the rules given in [18] for both the lanes, $l = \{1, 2\}$. Initially it is assumed that the vehicles are distributed uniformly along each lane with the realistic flow rate given in the Highway Capacity Manual [23], that is, 1300 vehicles/hour/lane and 1600 vehicles/hour/lane at an average speed of 30.5 m/s (110 km/h) and 22.5 m/s (80 km/h) in the outer lane $l = 1$ and inner lane $l = 2$, which implies 1 vehicle per 3 s and 1 vehicle per 2.5 s, respectively.

The initial values of $\Delta x_{l,a}^p(0)$ and $\Delta x_{l,a}^f(0)$ are determined from the initial positions $x_{l,a}(0)$ of the vehicles. The position and headways at each instant are updated by (2) and (3).

Let $N_1 = 160$ and $N_2 = 200$ be the initial number of vehicles in each lane, $v_1 = 27.7$ m/s (100 km/h) and $v_2 = 19.44$ m/s (70 km/h) the average velocity, and $v_{1,\max} = 30.5$ m/s (110 km/h) and $v_{2,\max} = 22.2$ m/s (80 km/h) the maximum speed in the outer and inner lanes, respectively. The other parameters such as the delay time, sensitivity factors, and initial safety distances are $\tau_1 = \tau_2 = 0.5$ s, $\lambda_1 = 0.3$, and $\lambda_2 = 0.2$ and $d_1^p = d_1^f = 40.5$, and $d_2^p = d_2^f = 36$ m, respectively.

Practically, the driver's sensitivity α_1 is larger than α_2 because the driver's response in the outer (fast) lane is more sensitive than in the inner (slow) lane. Here we assume that $\alpha_1 = \alpha_2$ because for the simulations it is easy to compute headways at fixed intervals and it is anticipated in [18] that the effect of α_i is small and does not change final results.

We let the simulations run for 10800 simulation time steps or seconds that correspond to 3 hours of simulated time. The data obtained from the first 3600 s of simulation is not considered for analysis to ensure that steady-state conditions are obtained. Hence, the time 0 s in the final results corresponds to the time 3600 s of the simulation.

Once the traffic flow is stable the positions and headways of all the vehicles are logged for each time instant, for further analysis, with respect to the vehicles' identity. The vehicles are allowed to change lane so whenever a vehicle changes lane it exits from subject-lane and becomes part of the target-lane. Thus for every lane change event at each time instant t the position, headway distances of each vehicle in both lanes, and the subject and target-lanes, should be updated accordingly.

The headways for three vehicles numbered 60, 120, and 180 are shown as cumulative distribution function (CDF) in Figure 3. It can be seen that there is a huge variation in the headway distances and they may vary between 20 m up to 600 m.

Further, to record the lane change activities, the total number of lane changes, the position, and time at which lane change occurred were logged over the simulation time for each vehicle. A sample result is shown in Figure 4, where the lane change activities of the three vehicles numbered 60, 120, and 180 are shown over 15 min of time window. It can be seen

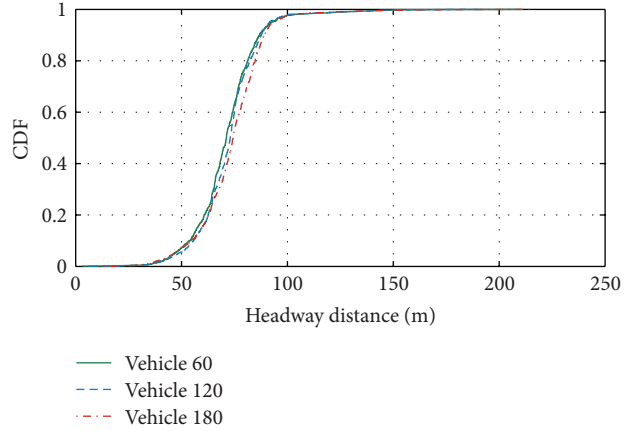


FIGURE 3: CDFs of the headway distances of vehicles at every second for total simulation time $T = 120$ min.

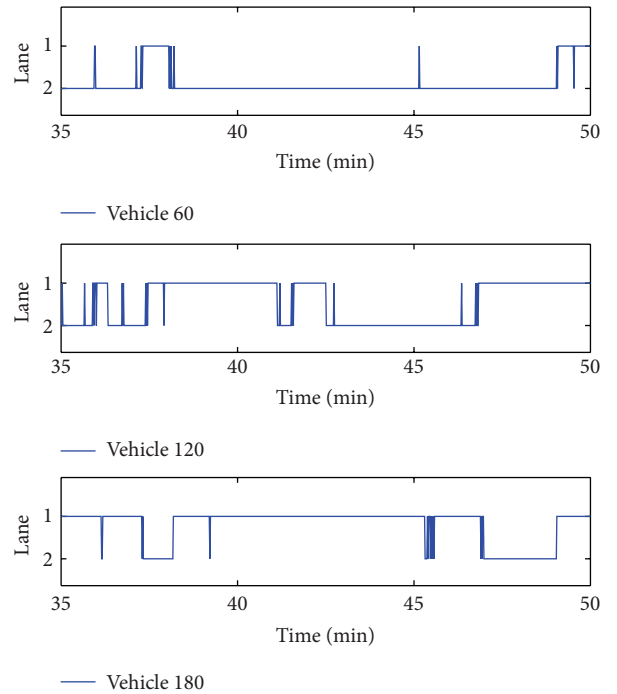


FIGURE 4: Three vehicles numbered 60, 120, and 180 changing lanes from lane 1 to lane 2 or vice versa between a time window of 35 min to 50 min.

that the lane change behavior for each vehicle is different at different times. The amount of time a vehicle stays in each lane depends very much on the driving conditions in that lane during that particular time window.

The main focus of this work is to identify the vehicles which are in OLOS from each other so that this information can be used for VANET simulations using the shadow fading path-loss model given in [3]. In order to analyze the LOS and OLOS situation and to find the intensities by which vehicles go from one state to another the following assumptions are made.

A vehicle numbered 20 is assumed to be the TX vehicle which is broadcasting the information within the intended communication range R_c , where R_c is a circle of radius 500 m with TX at its center. At each instant t the vehicles which lie in the R_c of the TX vehicle are identified and then categorized as vehicles being in LOS or in OLOS from the TX vehicle using the rules defined in Section 3. Any other vehicle that is outside this intended communication range R_c is treated as a vehicle out-of-range (OoR) from the TX. The states of vehicles being in LOS, OLOS, and OoR w.r.t. their identities are saved for each time instant. The CDF of the total number of vehicles in R_c and the number of vehicles in LOS and OLOS state at each time instant are shown in Figure 5, respectively. The OoR state is not interesting thus it is not discussed further.

Each time a vehicle is in LOS, or in OLOS, it remains in that state for a certain amount of time and travels a distance, $d_{l,a}^{\text{LOS}}(k)$ or $d_{n,a}^{\text{OLOS}}(k)$, where $k \in \{1, K\}$ is the index of that specific interval. The length of these intervals may vary over time as well as for each vehicle. So we log the count of these intervals and their corresponding distances $d_{l,a}^{\text{LOS}}(k)$ and $d_{n,a}^{\text{OLOS}}(k)$ for every vehicle over the whole simulation time. The CDFs of LOS and OLOS distance intervals for all vehicles are shown in Figure 6(a). We log the total distance traveled by each vehicle, $D_{l,a}$, during the simulation time and see how much of that distance is traveled in the LOS and OLOS state, $D_{l,a}^{\text{LOS}}$ and $D_{l,a}^{\text{OLOS}}$, by the vehicle $n_{l,a}$. The CDFs of total distance traveled in the LOS and OLOS by all vehicles are shown in Figure 6(b).

The number of state transitions, $N_{l,a}^{\text{LOS-OLOS}}$ and $N_{l,a}^{\text{OLOS-LOS}}$, from LOS-OLOS and OLOS-LOS states is counted for each vehicle. Thus the state transition intensities P and p from LOS-OLOS and OLOS-LOS for each vehicle can be calculated as

$$P = \frac{N_{l,a}^{\text{LOS-OLOS}}}{D_{l,a}^{\text{LOS}}}, \quad (9)$$

$$p = \frac{N_{l,a}^{\text{OLOS-LOS}}}{D_{l,a}^{\text{OLOS}}}.$$

The CDFs of the state transition intensities P and p for a given set of parameters are shown in Figure 7. The variations in the transition intensities are due to the fact that each vehicle has different moving and lane-changing patterns. The mean intensities μ_P and μ_p are calculated to be 0.0034 m^{-1} and 0.0026 m^{-1} , respectively. For comparison, sample state transition intensities are also calculated from the measurement data collected during a V2V measurement campaign conducted in the city of Lund and Malmö, Sweden, to analyze the shadow fading effects. The measurement data was separated for LOS and OLOS conditions (explained briefly in [3]). The separated data contains information about the number of state transitions between LOS and OLOS states and the distance traveled in each state. With this information the state transition intensities are calculated using (9); that is, $P_{\text{measured}} = 0.0035 \text{ m}^{-1}$ and $p_{\text{measured}} = 0.0020 \text{ m}^{-1}$, which are close to the mean values of the simulated intensities. The

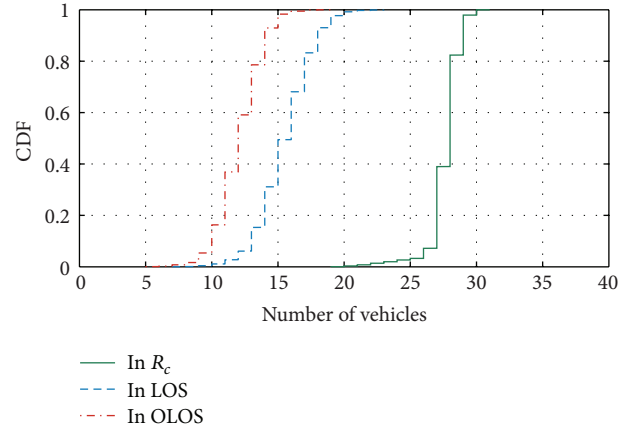


FIGURE 5: CDFs of the total number of vehicles in R_c and the number of vehicles in LOS and OLOS state at each time instant for total simulation time $T = 120$ min.

probability of vehicles being in LOS and in OLOS with respect to the distance can also be calculated from the simulation, as shown in Figure 8.

5. Analytical Performance Evaluation

In order to evaluate the impact of vehicle as an obstruction on V2V networks the proposed TMM together with the LOS/OLOS path-loss model given in [3] can be used in any VANET simulator. The LOS/OLOS path-loss model provides the deterministic and stochastic parameters of a dual slope distance dependent path-loss for both the LOS and OLOS situations. The stochastic part of the LOS/OLOS path-loss model comes from the large-scale fading, which is assumed to be Gaussian distributed. The packet reception probability (PRP) can be obtained by analytical expressions for all vehicles either in LOS or in OLOS states. Large-scale fading, or shadow fading, may refer to the signal variations that may not only be associated to blocked LOS but due to the blocking of many other significant reflected propagation paths. Therefore, it is associated to both the LOS and the OLOS state. The large-scale fading is a random process and it varies over time due to varying locations when the TX/RX vehicles are moving. The proposed TMM is assumed to be noise free; therefore the required noise due to randomness in driving behavior can be taken into account by large-scale fading process, which has a standard deviation σ that introduces variation in the received power due to variation in the position of each vehicle at each instant.

To study the performance differences in the PRP with and without considering vehicles as obstacles the LOS/OLOS model is compared with two other aforementioned path-loss models: (1) the LOS only single slope path-loss model by Karedal et al. [14] and (2) the Nakagami-m based path-loss and fading model by Cheng et al. [15] in which the data from LOS and blocked LOS cases is lumped together for modeling purpose.

To find an analytical expression for packet reception probability, it is assumed that each vehicle is a point source

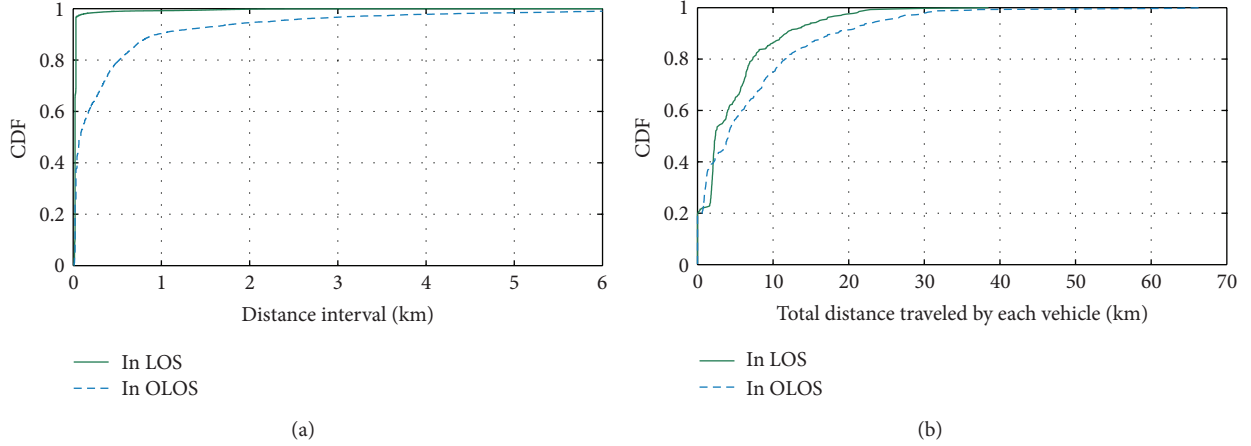


FIGURE 6: CDFs of (a) the LOS and OLOS intervals for all vehicles and (b) the total distance traveled in the LOS and OLOS by all vehicles.

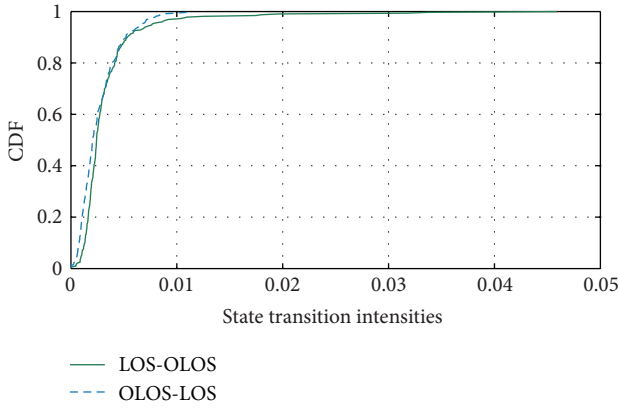


FIGURE 7: CDFs of the state transition intensities P and p from LOS-OLOS and OLOS-LOS, for each vehicle, respectively.

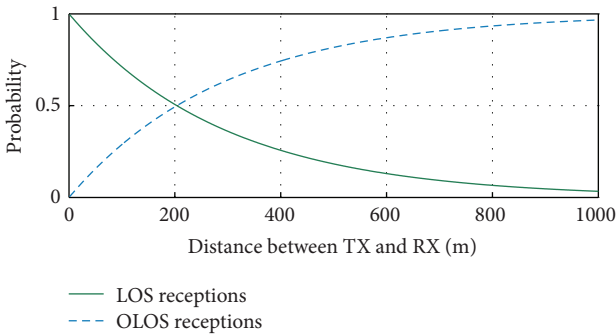


FIGURE 8: The probability of LOS and OLOS with respect to distance, and it can be seen that the probability of being in LOS decreases as the distance increases.

and vehicles are distributed along a straight line on both lanes of the highway and the probability of LOS and OLOS is known. The parameters of Karedal's LOS model, Cheng's Nakagami based model, and LOS/OLOS model are taken from [3, 14, 15], respectively. Then the received power Pw_{RX} for LOS-Karedal, LOS-Dual slope, OLOS-Dual slope, Cheng

model, and joint LOS/OLOS (LOS/OLOS model together with probability of LOS and OLOS) cases can individually be calculated as follows:

$$Pw_{RX}(d) = Pw_{TX} - PL(d), \quad (10)$$

where $PL(d)$ is a distance dependent mean power loss, given as

$$PL(d) = \begin{cases} PL_0 + 10n_1 \log_{10} \left(\frac{d}{d_0} \right) + X_\sigma, & \text{if } d_0 \leq d \leq d_b, \\ PL_0 + 10n_1 \log_{10} \left(\frac{d_b}{d_0} \right) \\ + 10n_2 \log_{10} \left(\frac{d}{d_b} \right) + X_\sigma, & \text{if } d > d_b, \end{cases} \quad (11)$$

where X_σ describes the large scale fading as zero mean Gaussian distributed random variable with standard deviation σ , PL_0 is the received power level at a reference distance $d_0 = 10$ m, and n_1 and n_2 are the path-loss exponents, respectively. The value of PL_0 , n_1 , n_2 , and σ for each of the aforementioned models are different and are obtained from the models given in [3, 14, 15]. The received power for all five cases is shown in Figure 9 for a transmitted power $Pw_{TX} = 20$ dBm. For the dual-slope LOS/OLOS model and Cheng's model the break point distance is provided; that is, $d_b = 104$ m; however for Karedal's single slope LOS model d_b is not required and thus it can assumed to be infinity.

From the above equations it is obvious that the received power is a Normally distributed with a distance dependent mean $\mu(d) = Pw_{TX} - PL(d)$ and standard deviation σ . The Gaussian probability density function is closely related to Q-function [24]; therefore, for a given distance d the probability of received power being greater than α , $P\{Pw_{RX}(d) > \alpha\}$, is calculated analytically as follows:

$$P\{Pw_{RX}(d) > \alpha\} = 1 - Q\left(\frac{\mu(d) - \alpha}{\sigma}\right), \quad (12)$$

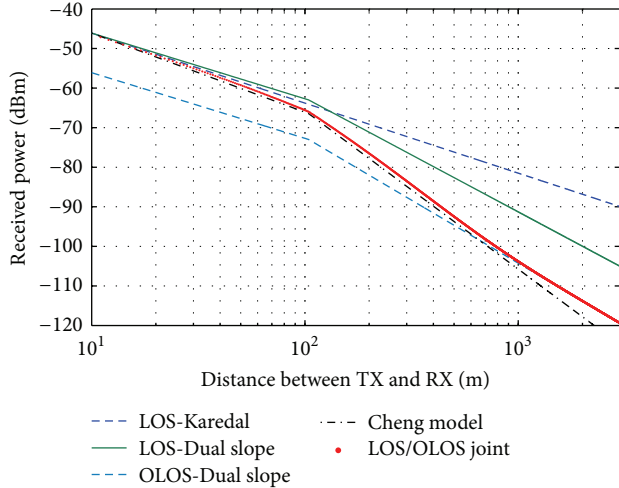


FIGURE 9: Received power as a function of distance. Breakpoint distance of $d_b = 104$ m is used for the LOS-Dual slope, OLOS-Dual slope, Cheng, and joint LOS/OLOS models.

where α is carrier sense threshold (CSTH). The parameters for each of these models can be used individually to find the probabilities $P^{\text{Karedal}}\{Pw_{\text{RX}}(d) > \alpha\}$, $P^{\text{Cheng}}\{Pw_{\text{RX}}(d) > \alpha\}$, $P^{\text{LOS}}\{Pw_{\text{RX}}(d) > \alpha\}$, and $P^{\text{OLOS}}\{Pw_{\text{RX}}(d) > \alpha\}$, respectively.

The probability of successful packet reception is shown in Figure 10, where CSTH = -91 dBm is assumed [25]. However the joint LOS/OLOS PRP is calculated by multiplying the probability of LOS and OLOS to the individual PRP, $P^{\text{LOS}}\{Pw_{\text{RX}}(d) > \alpha\}$, and $P^{\text{OLOS}}\{Pw_{\text{RX}}(d) > \alpha\}$, of LOS and OLOS as follows:

$$\begin{aligned} \text{PRP}^{\text{LOS/OLOS}} &= Pr^{\text{LOS}} \times P^{\text{LOS}}\{Pw_{\text{RX}}(d) > \alpha\} \\ &+ Pr^{\text{OLOS}} \times P^{\text{OLOS}}\{Pw_{\text{RX}}(d) > \alpha\}. \end{aligned} \quad (13)$$

From Figures 9 and 10, it can obviously be seen that the LOS and OLOS situations are fundamentally different. Comparing the PRP curves from the Karedal, Cheng and LOS/OLOS models, it can be observed that for the given vehicular traffic density the probabilities of LOS and OLOS vary which in turn affect the performance of the joint LOS/OLOS PRP. However, Karedal's path-loss model and Cheng's model do not take probabilities of LOS and OLOS into account and thus can not capture the effects of traffic density on the PRP. All models perform similarly up to $d = 100$ m approximately. However at the larger distances, where the probability of LOS obstruction increases, the behavior of these models differ.

6. Summary and Conclusions

In this paper the effect of line-of-sight (LOS) obstruction is analyzed for vehicle-to-vehicle (V2V) network simulations in a two-lane highway scenario using a traffic mobility model (TMM). A microscopic simulation model, the car-following model, is used to describe the movement of vehicles in the forward direction and the vehicles are allowed to change lane

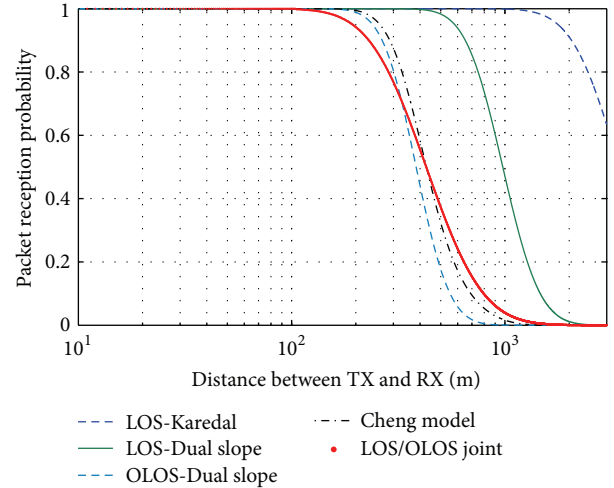


FIGURE 10: The probability of successful packet reception for a CSTH of -91 dBm.

when necessary. Realistic parameters are used for the simulations to achieve a traffic flow being as realistic as possible. Based on the simulated traffic the positions of all vehicles at each instant are recorded. The position information is then used to identify vehicles which are in LOS, obstructed-LOS (OLOS), or out-of-range (OoR) from a selected vehicle that is assumed to be a transmitter in the case of VANET simulations. Vehicles at each instant are defined either in one of the LOS, OLOS, or OoR states. The intensities of vehicles being in each state are logged which can be used to take into account the impact of OLOS in the VANET simulations. The proposed model is straight-forward to implement, gives realistic results, and is based on realistic assumptions for the traffic mobility. Analytical expressions for the packet reception probabilities are used together with the models. The results show the importance of including shadowing by other vehicles for realistic performance assessment.

Acknowledgments

This work was partially funded by the Excellence Center at Linköping-Lund In Information Technology (ELLIIT) and partially funded by the Higher Education Commission (HEC) of Pakistan.

References

- [1] J. Gozalvez, M. Sepulcre, and R. Bauza, "Impact of the radio channel modelling on the performance of VANET communication protocols," *Telecommunication Systems*, vol. 50, no. 3, pp. 149–167, 2012.
- [2] T. Abbas, J. Karedal, and F. Tufvesson, "Measurement-based analysis: the effect of complementary antennas and diversity on vehicle-to-vehicle communication," *IEEE Antennas and Wireless Propagation Letters*, vol. 12, no. 1, pp. 309–312, 2013.
- [3] T. Abbas, F. Tufvesson, K. Sjöberg, and J. Karedal, "Measurement based shadow fading model for vehicle-to-vehicle network simulations," <http://arxiv.org/abs/1203.3370v3>.

- [4] M. Boban, T. T. V. Vinhoza, M. Ferreira, J. Barros, and O. K. Tonguz, "Impact of vehicles as obstacles in vehicular ad hoc networks," *IEEE Journal on Selected Areas in Communications*, vol. 29, no. 1, pp. 15–28, 2011.
- [5] R. Meireles, M. Boban, P. Steenkiste, O. Tonguz, and J. Barros, "Experimental study on the impact of vehicular obstructions in VANETs," in *Proceedings of the IEEE Vehicular Networking Conference (VNC '10)*, pp. 338–345, December 2010.
- [6] The network simulator—ns-2, <http://www.isi.edu/nsnam/ns/>.
- [7] A. Varga and R. Hornig, "An overview of the omnet++ simulation environment," in *Proceedings of the 1st International Conference on Simulation Tools and Techniques for Communications, Networks and Systems & Workshops (Simutools '08)*, pp. 60:1–60:10, ICST (Institute for Computer Sciences, Social-Informatics and Telecommunications Engineering), Brussels, Belgium, 2008.
- [8] T. R. Henderson, S. Roy, S. Floyd, and G. F. Riley, "ns-3 project goals," in *Proceeding of the International Workshop on ns-2: The IP Network Simulator (WNS2 '06)*, ACM, Pisa, Italy, 2006.
- [9] R. Barr, Z. J. Haas, and R. van Renesse, "JiST: an efficient approach to simulation using virtual machines," *Software—Practice and Experience*, vol. 35, no. 6, pp. 539–576, 2005.
- [10] E. Weingärtner, H. vom Lehn, and K. Wehrle, "A performance comparison of recent network simulators," in *Proceedings of the IEEE International Conference on Communications (ICC '09)*, pp. 1–5, June 2009.
- [11] M. Behrisch, L. Bieker, J. Erdmann, and D. Krajzewicz, "SUMO—simulation of urban mobility: an overview," in *Proceedings of the 3rd International Conference on Advances in System Simulation (SIMUL '11)*, pp. 63–68, Barcelona, Spain, October 2011.
- [12] M. Bando, K. Hasebe, A. Nakayama, A. Shibata, and Y. Sugiyama, "Dynamical model of traffic congestion and numerical simulation," *Physical Review E*, vol. 51, no. 2, pp. 1035–1042, 1995.
- [13] T.-Q. Tang, H.-J. Huang, and Z.-Y. Gao, "Stability of the car-following model on two lanes," *Physical Review E*, vol. 72, Article ID 066124, 2005.
- [14] J. Karedal, N. Czink, A. Paier, F. Tufvesson, and A. F. Molisch, "Path loss modeling for vehicle-to-vehicle communications," *IEEE Transactions on Vehicular Technology*, vol. 60, no. 1, pp. 323–328, 2011.
- [15] L. Cheng, B. E. Henty, D. D. Stancil, F. Bai, and P. Mudalige, "Mobile vehicle-to-vehicle narrow-band channel measurement and characterization of the 5.9 GHz Dedicated Short Range Communication (DSRC) frequency band," *IEEE Journal on Selected Areas in Communications*, vol. 25, no. 8, pp. 1501–1516, 2007.
- [16] D. Chowdhury, L. Santen, and A. Schadschneider, "Statistical physics of vehicular traffic and some related systems," *Physics Report*, vol. 329, no. 4–6, pp. 199–329, 2000.
- [17] Y. Xuan and B. Coifman, "Identifying lane change maneuvers with probe vehicle data and an observed asymmetry in driver accommodation," *Journal of Transportation Engineering*, vol. 8, no. 138, pp. 1051–1061, 2012.
- [18] T. Tang, H. Huang, S. C. Wong, and R. Jiang, "Lane changing analysis for two-lane traffic flow," *Acta Mechanica Sinica*, vol. 23, no. 1, pp. 49–54, 2007.
- [19] Y. Weng and T. Wu, "Car-following model of vehicular traffic," in *Proceedings of the International Conferences on Info-Tech and Info-Net (ICII '01)*, vol. 44, pp. 101–106, Beijing, China, 2001.
- [20] S. Kurata and T. Nagatani, "Spatio-temporal dynamics of jams in two-lane traffic flow with a blockage," *Physica A*, vol. 318, no. 3–4, pp. 537–550, 2003.
- [21] L.-S. Jin, W.-P. Fang, Y.-N. Zhang, S.-B. Yang, and H.-J. Hou, "Research on safety lane change model of driver assistant system on highway," in *Proceedings of the IEEE Intelligent Vehicles Symposium*, pp. 1051–1056, June 2009.
- [22] B. Filzek and B. Breuer, "Distance behavior on motorways with regard to active safety comparison between adaptive-cruise-control (ACC) and driver," in *Proceedings of the International Technical Conference on Enhanced Safety of Vehicles*, Amsterdam, The Netherlands, 2001.
- [23] *Special Report 209: Highway Capacity Manual*, The Transportation Research Board National Research Council, Washington, DC, USA, 3rd edition, 1998.
- [24] J. Proakis, *Digital Communications*, McGraw-Hill, 5th edition, 2000.
- [25] K. Sjöberg, E. Uhlemann, and E. G. Ström, "How severe is the hidden terminal problem in VANETs when using CSMA and STDMA?" in *Proceedings of the 74th IEEE Vehicular Technology Conference (VTC '11)*, pp. 1–5, September 2011.

Research Article

Modeling, Real-Time Estimation, and Identification of UWB Indoor Wireless Channels

Mohammed M. Olama,¹ Seddik M. Djouadi,² Yanyan Li,² and Aly Fathy²

¹ Computational Sciences & Engineering Division, Oak Ridge National Laboratory, P.O. Box 2008, MS 6085, Oak Ridge, TN 37831, USA

² Electrical Engineering & Computer Science Department, University of Tennessee, 1520 Middle Drive, Knoxville, TN 37996, USA

Correspondence should be addressed to Mohammed M. Olama; olamahassem@ornl.gov

Received 12 July 2013; Accepted 1 November 2013

Academic Editor: Ai Bo

Copyright © 2013 Mohammed M. Olama et al. This is an open access article distributed under the Creative Commons Attribution License, which permits unrestricted use, distribution, and reproduction in any medium, provided the original work is properly cited.

Stochastic differential equations (SDEs) are used to model ultrawideband (UWB) indoor wireless channels. We show that the impulse responses for time-varying indoor wireless channels can be approximated in a mean-square sense as close as desired by impulse responses that can be realized by SDEs. The state variables represent the inphase and quadrature components of the UWB channel. The expected maximization and extended Kalman filter are employed to recursively identify and estimate the channel parameters and states, respectively, from online received signal strength measured data. Both resolvable and nonresolvable multipath received signals are considered and represented as small-scaled Nakagami fading. The proposed models together with the estimation algorithm are tested using UWB indoor measurement data demonstrating the method's viability and the results are presented.

1. Introduction

Ultrawideband (UWB) communication systems have recently attracted significant interest from both the research community and industry since the Federal Communications Commission (FCC) allowed limited unlicensed operation of UWB devices in the USA [1]. They are commonly defined as systems that have either more than 20% relative bandwidth or more than 500 MHz absolute bandwidth. UWB technology has many benefits, including high data rate, low interference, less sensitivity to multipath fading, low transmit power, and availability of low cost transceivers [2]. Industrial standards such as IEEE 802.15.3a and 802.15.4a have been established in recognizing these developments.

The ultimate performance limits of a communication system are determined by the channel it operates in [3]. Realistic channel models are thus of utmost importance for system design and testing. UWB propagation channels show fundamental differences from conventional (narrowband) ones in many respects [4, 5], and therefore the established (narrowband) channel models cannot be used. A number of UWB channel models have been proposed in the literature.

A model for frequency range below 1 GHz is suggested in [6]. A statistical model that is valid for a frequency range from 3 to 10 GHz is proposed in [7] and is accepted by the IEEE 802.15.4a task group as a standard model for evaluation of UWB system proposals. Significant experimental work in office, residential, and industrial environments has been reported in this field such as in [8, 9]. Most of the proposed channel models are based on characterizing the discrete multipath components. Although these models are able to capture the statistics of the channel, they cannot be specified by a finite number of parameters since their impulse responses are general functions of time and space and therefore are not easy to estimate directly from measurements.

A necessary and sufficient condition for representing any time-varying (TV) impulse response (IR) in stochastic state-space form is that it is factorizable into the product of two separate functions of time and space [10]. However, in general this is not the case for the IR of wireless channels. We show that the IR of indoor wireless channels can be approximated in the mean-square sense as close as desired by factorizable impulse responses that can be realized by stochastic differential equations (SDEs) in state-space form.

In particular, the SDEs are used to model UWB indoor channels and are combined with system identification algorithms to extract various parameters of the channel from received signal measurement data. The expected maximization (EM) and the extended Kalman filter (EKF) are employed in estimating channel parameters as well as the inphase and quadrature components, respectively. The EM and EKF are chosen since they are recursive and therefore can be implemented online. These algorithms have been recently utilized in [11–13] to estimate the channel parameters and states in narrowband environments, and therefore the formulations of these algorithms are not presented in this paper. Experiments are conducted in our UWB laboratory to collect received signal strength measured data, which are used to determine the applicability of the proposed models. These models can be used in the development of a practical channel simulator that replicates wireless channel characteristics and produces outputs that vary in a similar manner to the variations encountered in a real-world UWB channel environment.

Recently, there have been several papers on the application of SDEs to modeling propagation phenomena in radar scattering and wireless communications. SDEs have been successfully used to analyze K -distributed noise in electromagnetic scattering in [14]. Autoregressive stochastic models for the computer simulation of correlated Rayleigh fading processes are investigated in [15]. A first-order stochastic autoregressive model for a flat stationary wireless channel is introduced in [16]. Stochastic channel models based on SDEs for cellular and ad hoc networks have been presented in [12, 17, 18]. Some preliminary results using SDEs to model UWB channels were presented initially in [19]. The advantage of using SDE methods is based on the computational simplicity of the algorithm simply because estimation is done recursively. This means that there is no need to store and process all measurements; rather, at each time step, the estimator is updated using the previous estimator values and the new innovations.

The paper is organized as follows. In Section 2, the general TV narrowband and UWB indoor wireless channel impulse responses are introduced. In Section 3, we show that the impulse responses for TV indoor wireless channels can be approximated in a mean-square sense as close as desired by impulse responses that can be realized by SDEs. The stochastic UWB channel models are developed in Section 4. In Section 5, experimental setup and numerical results are presented. Finally, Section 6 provides concluding remarks.

2. The General Time-Varying Impulse Response for Indoor Wireless Channels

The general TV impulse response (in complex baseband) of an indoor wireless fading channel is typically represented by Saleh-Valenzuela (SV) model given as [20]

$$C(t; \tau) = \sum_{l=1}^L \sum_{k=1}^{K_l} a_{kl}(t, \tau) \exp(j\phi_{kl}(t, \tau)) \times \delta(t - T_l(t) - \tau_{kl}(t)), \quad (1)$$

where $C(t; \tau)$ is the impulse response of the channel at time t , due to an impulse applied at time $t - \tau$, $a_{kl}(t, \tau)$ and $\phi_{kl}(t, \tau)$ are, respectively, the random TV tap weight and phase of the k th component in the l th cluster, $T_l(t)$ is the delay of the l th cluster, $\tau_{kl}(t)$ is the delay of the k th multipath component (MPC) relative to the l th cluster arrival $T_l(t)$, $\delta(\cdot)$ is the Dirac delta function, K_l is the total number of MPCs within the l th cluster, and L is the total number of clusters that can either be assumed fixed [21] or considered to be a random variable [7]. Let $s(t)$ be the transmitted signal; the received signal is then given by

$$y(t) = \sum_{l=1}^L \sum_{k=1}^{K_l} a_{kl}(t, \tau) \exp(j\phi_{kl}(t, \tau)) \times s(t - T_l(t) - \tau_{kl}(t)) + v(t), \quad (2)$$

where $v(t)$ is the measurement noise process.

For narrowband systems, complex Gaussian fading is conventionally used to describe the small-scale fading. More precisely, the equivalent complex baseband representation consists of Rayleigh-distributed amplitude and uniformly distributed phase. This can be related theoretically to the fact that a large number of multipath components fall into each resolvable delay bin, so that the central limit theorem is valid [3]. Therefore, $a_{kl}(t, \tau)$ and $\phi_{kl}(t, \tau)$ are statistically independent Rayleigh and uniform (over $[0, 2\pi]$) random processes, respectively [20].

In UWB systems, the central limit theorem is not valid, and a number of alternative amplitude distributions have been proposed in the literature. The most common empirically determined amplitude distribution in many UWB environments is Nakagami distribution, which is observed in [6, 8] and considered in the IEEE 802.15.4a standard [7]. Therefore, in UWB systems, $a_{kl}(t, \tau)$ and $\phi_{kl}(t, \tau)$ are statistically independent Nakagami and uniform random processes, respectively. In the next section, the corresponding impulse response with $a_{kl}(t, \tau)$ and $\phi_{kl}(t, \tau)$ for the time-varying indoor wireless channels in (1) is approximated in a mean-square sense as close as desired by SDEs.

3. Approximating the Time-Varying Impulse Response for Indoor Wireless Channels by SDEs

Now, we want to represent the TV IR in (1) with a stochastic state-space form in order to allow well-developed tools of estimation and identification to be applied to this class of problems. The following theorem states a necessary and sufficient condition for the realization of the TV IR.

Theorem 1 (see [10]). *The impulse response $C(t; \tau)$ of a TV system has a stochastic state-space realization if and only if it is factorizable; that is, there exist functions $g(\cdot)$ and $f(\cdot)$ such that for all t and τ , one has*

$$C(t; \tau) = g(t) f(\tau). \quad (3)$$

It is readily seen from the expression of the IR $C(t; \tau)$ of the indoor wireless channels in (1) that in general it is not

factorizable in the form (3) since $a_{kl}(t, \tau)$ and $\phi_{kl}(t, \tau)$ are arbitrary functions of t and τ . However, one will show that in general $C(t; \tau)$ can be approximated as close as desired by a factorizable IR function.

Theorem 2. *In general, the IR $C(t; \tau)$ of the indoor wireless channel in (1) can be approximated as close as desired by a factorizable function.*

Proof. The IR $C(t; \tau)$ of the indoor wireless channel has finite energy; that is,

$$C(t; \tau) \in L^2([0, \infty) \times [0, \infty)), \quad (4)$$

where $L^2([0, \infty) \times [0, \infty))$ is the Hilbert space of square integrable complex valued functions defined on $[0, \infty) \times [0, \infty)$ with the norm

$$\|f\|_2^2 := \iint_{[0, \infty)[0, \infty)} |f(t; \tau)|^2 d\tau dt < \infty, \quad (5)$$

$$f(t; \tau) \in L^2([0, \infty) \times [0, \infty)).$$

Likewise define $L^2([0, \infty))$ as the standard Hilbert space of square integrable complex valued functions defined on $[0, \infty)$ under the norm

$$\|x\|_2^2 := \int_0^\infty |x(t)|^2 dt, \quad x \in L^2([0, \infty)). \quad (6)$$

The space $L^2([0, \infty))$ contains all finite energy signals defined on $[0, \infty)$. The IR $C(t; \tau)$ of the channel has a finite energy and belongs to $L^2([0, \infty) \times [0, \infty))$; that is,

$$\|C\|_2^2 := \iint_{[0, \infty)[0, \infty)} |C(t; \tau)|^2 d\tau dt < \infty. \quad (7)$$

Since the transmitted and received signals are finite energy signals, the IR can be viewed as an integral operator mapping transmitted signals in $L^2([0, \infty))$ into $L^2([0, \infty))$; that is, if $s \in L^2([0, \infty))$, then

$$y(t) = \int_0^\infty C(t; \tau) s(t - \tau) d\tau \in L^2([0, \infty)). \quad (8)$$

The tensor space

$$L^2([0, \infty)) \otimes L^2([0, \infty))$$

$$:= \left\{ F(t, \tau) \in L^2([0, \infty) \times [0, \infty)) : \right.$$

$$F(t, \tau) = \sum_{k=1}^n \alpha_k(t) \phi_k(\tau), \quad (9)$$

$$\alpha_k(t) \in L^2([0, \infty)),$$

$$\left. \phi_k(\tau) \in L^2([0, \infty)), \forall n \text{ integer} \right\}$$

is dense in $L^2([0, \infty) \times [0, \infty))$; that is, for any $\varepsilon > 0$, there exist $\{\alpha_k\}_1^n, \{\phi_k\}_1^n \subset L^2([0, \infty))$ such that [22]

$$\mu_n := \left\| C(t; \tau) - \sum_{k=1}^n \alpha_k(t) \phi_k(\tau) \right\|_2 \leq \varepsilon \quad (10)$$

and $\mu_n \rightarrow 0$. This implies that in the $\|\cdot\|_2$ -norm, $C(t; \tau)$ can be approximated to any desired accuracy by an IR of the form $\sum_{k=1}^n \alpha_k(t) \phi_k(\tau)$, which is factorizable by putting $g(t) := [\alpha_1(t) \alpha_2(t) \cdots \alpha_n(t)]$ and $f(\tau) := [\phi_1(\tau) \phi_2(\tau) \cdots \phi_n(\tau)]^T$, where T denotes vector or matrix transpose.

The optimal approximation of $C(t; \tau)$ by functions in $L^2([0, \infty)) \otimes L^2([0, \infty))$ corresponding to (10) can be written as

$$\mu_n^* := \inf_{\substack{\alpha_k(t) \in L^2([0, \infty)), \\ \phi_k(\tau) \in L^2([0, \infty))}} \left\| C(t; \tau) - \sum_{k=1}^n \alpha_k(t) \phi_k(\tau) \right\|_2. \quad (11)$$

For arbitrary n , expression (11) is nothing but the shortest distance between the impulse function $C(t; \tau)$ and the space $L^2([0, \infty)) \otimes L^2([0, \infty))$; that is, $\mu_n^* = \text{dist}(C(t; \tau), L^2([0, \infty)) \otimes L^2([0, \infty)))$. The problem is to find the minimizing functions $\{\alpha_k\}_1^n, \{\phi_k\}_1^n$. This problem has been solved in [22] for arbitrary positive n . However, for fixed positive n , the problem becomes the shortest distance, denoted by $\mu_n^o := \text{dist}(C(t; \tau), S)$, from $C(t; \tau)$ to the set

$$S := \left\{ F(t, \tau) = \sum_{k=1}^n \alpha_k(t) \phi_k(\tau), \alpha_k(t) \in L^2([0, \infty)), \right.$$

$$\left. \phi_k(\tau) \in L^2([0, \infty)), n > 0 \text{ fixed} \right\}. \quad (12)$$

Note that S is not a subspace and is not a convex set since it is not closed under addition. Therefore, the argument presented in [22] does not hold anymore since the orthogonal projection onto the set S is not linear. Following [22], the impulse response is viewed as an integral operator T mapping transmitted signals from $L^2([0, \infty))$ into $L^2([0, \infty))$; that is, if $s_i \in L^2([0, \infty))$, then $y_i(t) \in L^2([0, \infty))$, where

$$y_i(t) = (Ts_i)(t) := \int_0^\infty C(t; \tau) s_i(t - \tau) d\tau. \quad (13)$$

Since the impulse response is finite energy, the operator T is a Hilbert-Schmidt or a trace class 2 operator [22, 23]. Let us denote the class of Hilbert-Schmidt operators acting from $L^2([0, \infty))$ into $L^2([0, \infty))$ by C_2 and the Hilbert-Schmidt norm $\|\cdot\|_{\text{HS}}$ is defined by

$$\|T\|_{\text{HS}} = \sqrt{\iint_{[0, \infty)[0, \infty)} |C(t; \tau)|^2 d\tau dt}, \quad T \in C_2. \quad (14)$$

The operator T admits a spectral factorization of the form [22, 23]

$$T = \sum_{i=1}^{\infty} \lambda_i \nu_i \otimes \psi_i, \quad (15)$$

where \otimes is the tensor product, $\lambda_i > 0$ with $\lambda_i \geq \lambda_{i+1}$, $i = 1, 2, \dots$, and both $\{\nu_i\}_1^\infty$ and $\{\psi_i\}_{i=1}^\infty$ are orthonormal sequences in $L^2([0, \infty))$ and are given by

$$\nu_i(t) = \int_0^\infty C(t; \tau) \psi_i(\tau) d\tau, \quad \psi_i(\tau) = \int_0^\infty C(t; \tau) \nu_i(t) dt. \quad (16)$$

The sum (15) has either a finite or countably infinite number of terms. The above representation is unique. The Hilbert-Schmidt norm of T is also given by

$$\|T\|_{\text{HS}} = \sqrt{\sum_i \lambda_i^2} < \infty. \quad (17)$$

The spectral factorization (15) yields the following representation for the impulse response $C(t; \tau)$ [23]:

$$C(t; \tau) = \sum_{i=1}^{\infty} \lambda_i \nu_i(t) \psi_i(\tau). \quad (18)$$

It follows that the minimum in (11) is given by taking.

$$\alpha_k(t) = \lambda_k \nu_k(t), \quad \phi_k(\tau) = \psi_k(\tau), \quad k = 1, 2, \dots, n. \quad (19)$$

To further illustrate this result, note that $\{\nu_i\}_{i=1}^{\infty}$ and $\{\psi_i\}_{i=1}^{\infty}$ are orthonormal systems, and simple computations yield

$$\left\| C(t; \tau) - \sum_{k=1}^n \lambda_k \nu_k(t) \psi_k(\tau) \right\|_2^2 = \|C(t; \tau)\|_2^2 - \sum_{k=1}^n \lambda_k^2. \quad (20)$$

Schmidt in [24] showed that for any other functions $f_i(t), g_i(\tau) \in L^2([0, \infty))$, $i = 1, 2, \dots, n$, the following inequality holds:

$$\left\| C(t; \tau) - \sum_{k=1}^n f_k(t) g_k(\tau) \right\|_2^2 \geq \|C(t; \tau)\|_2^2 - \sum_{k=1}^n \lambda_k^2, \quad (21)$$

and therefore the minimum in (11) is given by (19). The optimal approximation follows as

$$\mu_n^o = \left\| C(t; \tau) - \sum_{k=1}^n \lambda_k \nu_k(t) \psi_k(\tau) \right\|_2 = \sqrt{\sum_{k=n+1}^{\infty} \lambda_k^2} \quad (22)$$

and $\mu_n^o \xrightarrow{n \rightarrow \infty} 0$. That is, by increasing n , the RHS of (22) can be made arbitrarily small. In other words, for large enough n , the following approximation is optimal in a mean-square sense:

$$C(t; \tau) \approx \sum_{i=1}^n \lambda_i \nu_i(t) \psi_i(\tau) \quad (23)$$

and is factorizable. \square

The corresponding SDE is then given by [10]

$$dX(t) = f(t) dW(t), \quad y(t) = g(t) X(t), \quad (24)$$

where $X(t)$ is the state of the channel and $W(t)$ is the standard Brownian motion. Since state-space realizations of impulse responses are not unique [10], a realization of the following form in terms of the inphase and quadrature components for the k th path within the l th cluster can be used as [12, 17]

$$\begin{aligned} dX_{kl}^I(t) &= A_{kl}^I(t) X_{kl}^I(t) dt + B_{kl}^I(t) dW_{kl}^I(t), \\ I_{kl}(t) &= H_{kl}^I(t) X_{kl}^I(t), \\ dX_{kl}^Q(t) &= A_{kl}^Q(t) X_{kl}^Q(t) dt + B_{kl}^Q(t) dW_{kl}^Q(t), \\ Q_{kl}(t) &= H_{kl}^Q(t) X_{kl}^Q(t), \end{aligned} \quad (25)$$

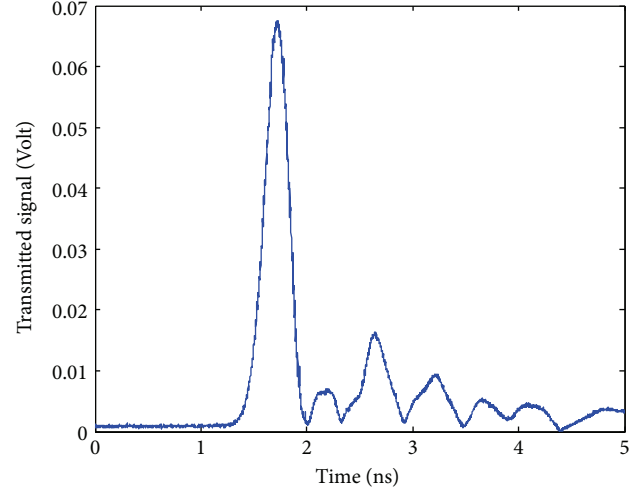


FIGURE 1: Transmitted signal of a 300-picosecond Gaussian pulse shape.

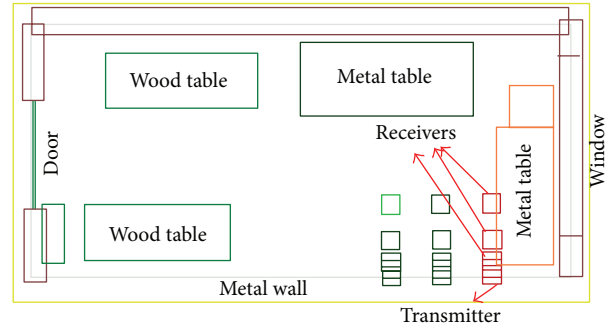


FIGURE 2: The indoor environment considered in our experiment.

where $I_{kl}(t)$ and $Q_{kl}(t)$ are, respectively, the inphase and quadrature component processes, $X_{kl}^I(t)$ and $X_{kl}^Q(t)$ are, respectively, the state vectors of the inphase and quadrature components, $\{W_{kl}^I(t)\}_{t \geq 0}$ and $\{W_{kl}^Q(t)\}_{t \geq 0}$ are two independent standard Brownian motions which correspond to the inphase and quadrature components, respectively, and $A_{kl}^I(t), A_{kl}^Q(t), B_{kl}^I(t), B_{kl}^Q(t), H_{kl}^I(t)$, and $H_{kl}^Q(t)$ are matrices of appropriate dimensions. Note that $I_{kl}(t)$ and $Q_{kl}(t)$ are two independent Gaussian processes with zero-mean and equal variances; that is, $\text{Var}(I_{kl}(t)) = \text{Var}(Q_{kl}(t)) = \text{Var}(N_{kl}(t))$, where $N_{kl}(t)$ is either $I_{kl}(t)$ or $Q_{kl}(t)$ [13]. They are related to the tap weight $a_{kl}(t, \tau)$ and phase $\phi_{kl}(t, \tau)$ by the expressions $a_{kl}(t, \tau) = \sqrt{I_{kl}^2(t, \tau) + Q_{kl}^2(t, \tau)}$ and $\phi_{kl}(t, \tau) = \arctan(Q_{kl}(t, \tau)/I_{kl}(t, \tau))$, respectively. In the next section, the stochastic narrowband and UWB indoor channel models are developed.

4. Stochastic State-Space Models for UWB Indoor Wireless Channels

In narrowband systems, the equivalent indoor complex baseband representation consists of Rayleigh-distributed amplitude and uniformly distributed phase [20]. Thus, the

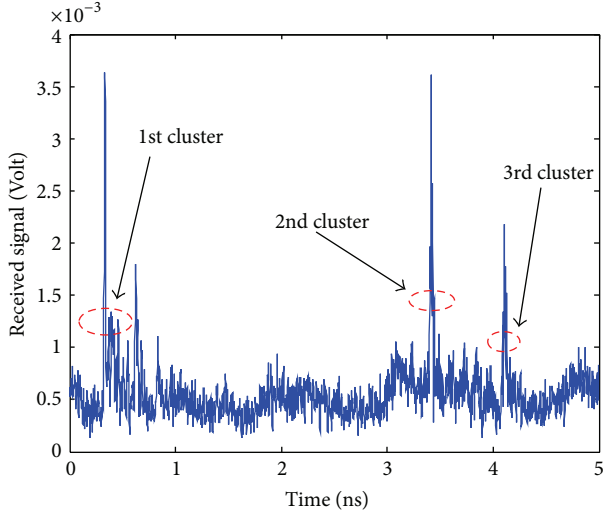


FIGURE 3: The measured UWB received signal.

stochastic narrowband indoor state-space channel model can be represented as

$$\begin{aligned}
 dX_{kl}(t) &= A_{kl}(t) X_{kl}(t) dt + B_{kl}(t) dW_{kl}(t), \\
 y(t) &= \sum_{l=1}^L \sum_{k=1}^{K_l} \sqrt{(C_{kl}^I(t) X_{kl}(t))^2 + (C_{kl}^Q(t) X_{kl}(t))^2} \\
 &\quad \times e^{j \arctan(C_{kl}^Q(t) X_{kl}(t) / C_{kl}^I(t) X_{kl}(t))} \\
 &\quad \times s(t - T_l(t) - \tau_{kl}(t)) + D(t) v(t),
 \end{aligned} \quad (26)$$

where

$$X_{kl}(t) = [X_{kl}^I(t)^T \ X_{kl}^Q(t)^T]^T,$$

$$W_{kl}(t) = [W_{kl}^I(t)^T \ W_{kl}^Q(t)^T]^T,$$

$$A_{kl}(t) = \begin{bmatrix} A_{kl}^I(t) & 0 \\ 0 & A_{kl}^Q(t) \end{bmatrix},$$

$$B_{kl}(t) = \begin{bmatrix} B_{kl}^I(t) & 0 \\ 0 & B_{kl}^Q(t) \end{bmatrix},$$

$$C_{kl}^I(t) = [H_{kl}^I(t) \ 0], \quad C_{kl}^Q(t) = [0 \ H_{kl}^Q(t)],$$

$$I_{kl}(t, \tau) = C_{kl}^I(t) X_{kl}(t), \quad Q_{kl}(t, \tau) = C_{kl}^Q(t) X_{kl}(t), \quad (27)$$

where $v(t)$ is the measurement noise which is assumed to be Gaussian with zero-mean and unit variance and the tap weight process $a_{kl}(t, \tau) = \sqrt{(C_{kl}^I(t) X_{kl}(t))^2 + (C_{kl}^Q(t) X_{kl}(t))^2}$ and the phase process $\phi_{kl}(t, \tau) = \arctan(C_{kl}^Q(t) X_{kl}(t) / C_{kl}^I(t) X_{kl}(t))$ are independent Rayleigh- and uniform-distributed random processes,

respectively. In this case, the tap weight process $a_{kl}(t, \tau)$ has the following statistics [25]:

$$E\{a_{kl}(t, \tau)\} = \sqrt{\frac{\pi}{2} \text{Var}(N_{kl}(t))},$$

$$E\{(a_{kl}(t, \tau))^p\} = (2 \text{Var}(N_{kl}(t)))^{p/2} \Gamma\left(1 + \frac{1}{2}p\right), \quad (28)$$

$$\text{Var}\{a_{kl}(t, \tau)\} = \left(2 - \frac{\pi}{2}\right) \text{Var}(N_{kl}(t)),$$

where $\Gamma(p)$ is the gamma function.

In UWB systems, as mentioned earlier, the most common amplitude distribution of the received signal is Nakagami distribution [6–8]. Its probability density function is given by [26]

$$f(x) = \frac{2}{\Gamma(m)} \left(\frac{m}{\Omega}\right)^m x^{2m-1} \exp\left(-\frac{m}{\Omega} x^2\right), \quad (29)$$

where $m \geq 0.5$ is the shape parameter, $\Gamma(m)$ is the Gamma function, and Ω controls the spread of distribution. The m -parameter is often modeled as a random variable [6]. For integer value of m , the distribution describes m orthogonal independent Rayleigh-distributed random variables. That is, for M Rayleigh-distributed random variables Z_i , the probability density function of random variable Y , defined as $Y = \sqrt{\sum_{i=1}^M Z_i^2}$, is given by a Nakagami distribution with parameter $m = M$ [27].

Since multiple orthogonal independent Rayleigh-distributed random variables can generate Nakagami distribution, the stochastic UWB indoor state-space channel model can be represented by

$$dX_{ikl}(t) = A_{ikl}(t) X_{ikl}(t) dt + B_{ikl}(t) dW_{ikl}(t),$$

$$\begin{aligned}
 y(t) &= \sum_{l=1}^L \sum_{k=1}^{K_l} \sqrt{\sum_{i=1}^{M_{kl}} (C_{ikl}^I(t) X_{ikl}(t))^2 + (C_{ikl}^Q(t) X_{ikl}(t))^2} \\
 &\quad \times e^{j \arctan(C_{ikl}^Q(t) X_{ikl}(t) / C_{ikl}^I(t) X_{ikl}(t))} \\
 &\quad \times s(t - T_l(t) - \tau_{kl}(t)) + D(t) v(t),
 \end{aligned} \quad (30)$$

where

$$X_{ikl}(t) = [X_{ikl}^I(t)^T \ X_{ikl}^Q(t)^T]^T,$$

$$W_{ikl}(t) = [W_{ikl}^I(t)^T \ W_{ikl}^Q(t)^T]^T,$$

$$A_{ikl}(t) = \begin{bmatrix} A_{ikl}^I(t) & 0 \\ 0 & A_{ikl}^Q(t) \end{bmatrix},$$

$$B_{ikl}(t) = \begin{bmatrix} B_{ikl}^I(t) & 0 \\ 0 & B_{ikl}^Q(t) \end{bmatrix},$$

$$C_{ikl}^I(t) = [H_{ikl}^I(t) \ 0], \quad C_{ikl}^Q(t) = [0 \ H_{ikl}^Q(t)],$$

$$I_{ikl}(t, \tau) = C_{ikl}^I(t) X_{ikl}(t), \quad Q_{ikl}(t, \tau) = C_{ikl}^Q(t) X_{ikl}(t), \quad (31)$$

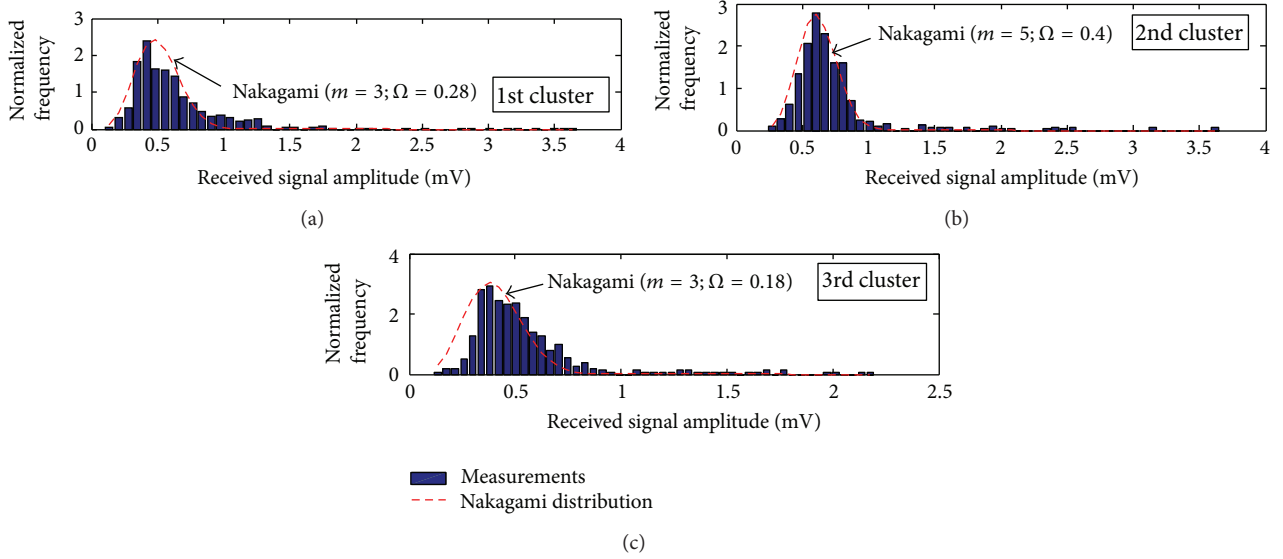


FIGURE 4: Histogram of measurement data for the dominant paths within the three clusters that are best fit to Nakagami distributions.

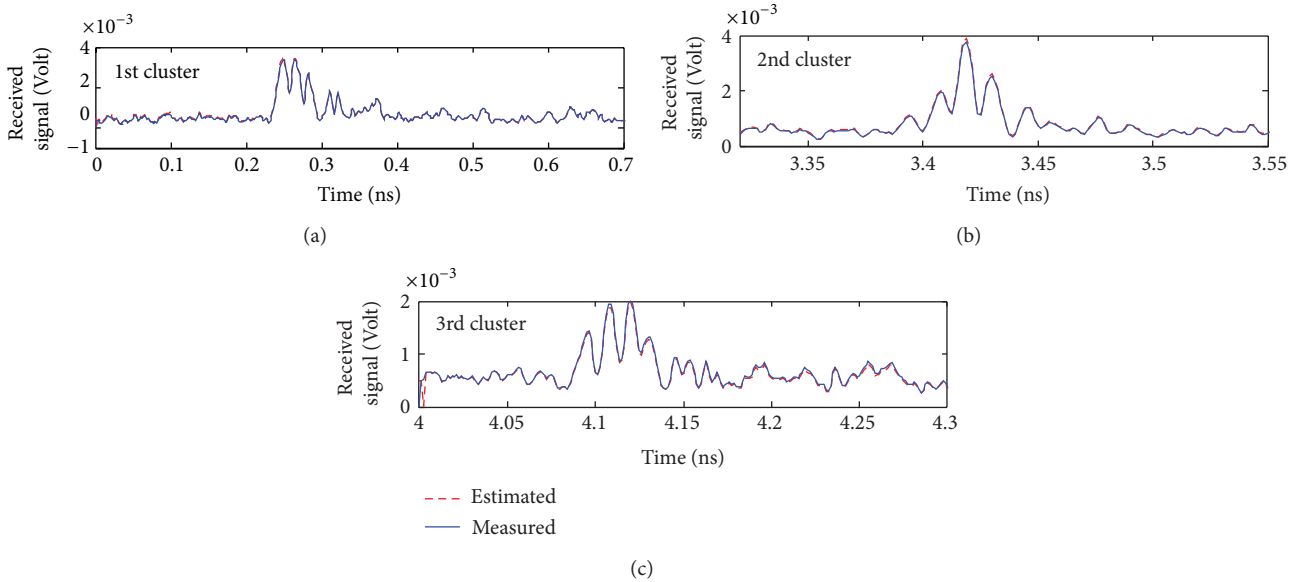


FIGURE 5: Measured and estimated received signals using the EM algorithm combined with the EKF for the 1st, 2nd, and 3rd clusters.

where L is the total number of clusters, K_l is the total number of resolvable delay bins (paths), and M_{kl} is the number of nonresolvable delay bins within the resolvable delay bin k in cluster l . In this case, the tap weight process $a_{kl}(t, \tau)$ has the following statistics [25]:

$$E \{a_{kl}(t, \tau)\} = \sqrt{2 \text{Var}(N_{kl}(t))} \frac{\Gamma((1/2)(2M_{kl} + 1))}{\Gamma(M_{kl})},$$

$$E \{(a_{kl}(t, \tau))^p\} = (2 \text{Var}(N_{kl}(t)))^{p/2} \frac{\Gamma((1/2)(2M_{kl} + p))}{\Gamma(M_{kl})},$$

$$p \geq 0,$$

$$\Omega_{kl} = 2 \text{Var}(N_{kl}(t)) \frac{\Gamma(M_{kl} + 1)}{\Gamma(M_{kl})}.$$
(32)

It can be noticed in (30) that the received signal measurement, $y(t)$, is a nonlinear function of the state variables of the model. The UWB channel parameters are estimated using the EM algorithm, and the inphase and quadrature components are estimated directly from received signal measurements using the EKF. A filter-based EM algorithm together with the EKF is employed to estimate the channel model parameters and states in (30). These filters use only the first- and second-order statistics and are also recursive and therefore can be implemented online. These algorithms have been recently utilized in [11–13] to estimate the channel parameters and states in narrowband environments, and therefore the formulations of these algorithms are not presented in this paper. Experimental results demonstrating the applicability of these algorithms in UWB indoor environments are discussed in the next section.

5. Experimental Setup and Numerical Results

A simple Gaussian pulse with clean pulse shape and narrow pulse width is chosen as UWB source signal. The experimental setup is similar to the one in [28]. It comprises a 300-picosecond Gaussian pulse (see Figure 1) that modulates a carrier signal centered at 8 GHz and is transmitted through an omnidirectional UWB antenna. Multiple directional Vivaldi subarray receiving antennas are located at distinct locations in an indoor environment to receive the modulated pulse signal. Each received modulated Gaussian pulse is amplified through a low noise amplifier (LNA) and then stored in a multichannel Tektronix TDS8200 sampling oscilloscope.

The transmitter is located next to a metal wall. The receiving antenna is placed 10 cm away from the transmitter and then moved along the same direction away from the transmitter for 20 cm, 50 cm, 1 m, and 2 m. This scenario is demonstrated in Figure 2. In this environment, the transmitted signal suffers from reflection from the metal wall, ceiling, or floor or is scattered by the corner of the metal table, and then it reaches the receiver. Figure 3 shows the measured received signal which consists of three clusters. The measurement data are amplified by 30 dB and it can be seen in Figure 4 that the dominant path in each cluster is best fit to Nakagami distribution with different parameters. For example, the dominant path in the first cluster is best fit to Nakagami distribution with parameters $m = 3$ and $\Omega = 0.28$. This indicates that there are three nonresolvable delay bins within this path (i.e., $M_{11} = 3$). Figure 5 shows the measured and estimated received signals using the EM algorithm together with the EKF for the three clusters using a 4th-order model. It can be noticed that the UWB received signal has been estimated with very high accuracy and it takes little iteration for the estimation algorithm to converge. At a certain time instant, the system parameters for the dominant path in the 1st cluster, which consists of three nonresolvable delay bins, are estimated as follows:

$$\begin{aligned}\widehat{A}_{111} &= \begin{bmatrix} 0 & 1 & 0 & 0 \\ 0.1928 & 0.0556 & 0 & 0 \\ 0 & 0 & 0 & 1 \\ 0 & 0 & 0.1484 & -0.0966 \end{bmatrix}, \\ \widehat{A}_{211} &= \begin{bmatrix} 0 & 1 & 0 & 0 \\ 0.2917 & 0.0556 & 0 & 0 \\ 0 & 0 & 0 & 1 \\ 0 & 0 & 0.3563 & -0.0682 \end{bmatrix}, \\ \widehat{A}_{311} &= \begin{bmatrix} 0 & 1 & 0 & 0 \\ 0.2014 & -0.0586 & 0 & 0 \\ 0 & 0 & 0 & 1 \\ 0 & 0 & 0.1881 & -0.2669 \end{bmatrix}, \\ \widehat{B}_{111}^2 &= \begin{bmatrix} 0.1699 & 0.2451 & 0.0122 & 0.0009 \\ 0.0004 & 0.0961 & 0.0287 & -0.0004 \\ 0.0122 & 0.0087 & 0.1628 & 0.0213 \\ 0.0077 & 0.0254 & 0.2959 & -0.0066 \end{bmatrix},\end{aligned}$$

$$\widehat{B}_{211}^2 = \begin{bmatrix} 0.0006 & 0.0182 & 0.1429 & 0.0077 \\ 0.0043 & -0.0256 & 0.0076 & -0.2597 \\ 0.0795 & 0.0056 & 0.0043 & 0.0218 \\ -0.0177 & 0.0192 & 0.1541 & -0.1632 \end{bmatrix},$$

$$\widehat{B}_{311}^2 = \begin{bmatrix} 0.2561 & 0.0013 & 0.3310 & 0.0069 \\ 0.0129 & 0.0213 & -0.0107 & 0.0921 \\ 0.0044 & 0.0015 & 0.0824 & 0.0076 \\ 0.1541 & 0.1429 & 0.1632 & -0.3334 \end{bmatrix},$$

$$\widehat{C}_{111}^I = \widehat{C}_{211}^I = \widehat{C}_{311}^I = [1 \ 0 \ 0 \ 0],$$

$$\widehat{C}_{111}^Q = \widehat{C}_{211}^Q = \widehat{C}_{311}^Q = [0 \ 0 \ 1 \ 0],$$

$$\widehat{D}^2 = [0.8765].$$

(33)

Notice that the EM algorithm estimates \widehat{B}^2 and \widehat{D}^2 instead of \widehat{B} and \widehat{D} . Also note that the parameters L , K_l , M_{kl} , T_l , and τ_{kl} are assumed known through the estimation process. In fact, the parameters L , K_l , and M_{kl} can be estimated by various estimation algorithms such as minimum description length [29], multiple hypothesis testing [30], exponential fitting test [31], and linear piecewise variation [32]. And a sounding device is usually dedicated to estimate the time delay of each discrete path (i.e., T_l and τ_{kl}) such as the rake receiver [33].

6. Conclusion

This paper describes a general scheme for extracting mathematical UWB indoor channel models from noisy received signal measurements. The UWB channel models are represented in stochastic state-space form, in which its system output produces Nakagami-distributed received signal strength and it is shown to approximate the general TV IR of the channel as close as desired. Experimental results indicate that the measured data can be regenerated with high accuracy.

Acknowledgments

This paper has been authored by employees of UT-Battelle, LLC, under Contract no. DE-AC05-00OR22725 with the US Department of Energy. Also, this work was supported in part by NSF Grant no. CMMI-1334094.

References

- [1] Federal Communications Commission, "First report 02-48," 2002.
- [2] M. Z. Win and R. A. Scholtz, "Impulse radio: how it works," *IEEE Communications Letters*, vol. 2, no. 2, pp. 36–38, 1998.
- [3] A. F. Molisch, *Wireless Communications*, IEEE Press/Wiley, New York, NY, USA, 2005.
- [4] R. C. Qiu, "A generalized time domain multipath channel and its application in ultra-wideband (UWB) wireless optimal receiver—part III: system performance analysis," *IEEE Transactions on Wireless Communications*, vol. 5, no. 10, pp. 2685–2695, 2006.

- [5] A. F. Molisch, "Ultrawideband propagation channels-theory, measurement, and modeling," *IEEE Transactions on Vehicular Technology*, vol. 54, no. 5, pp. 1528–1545, 2005.
- [6] D. Cassioli, M. Z. Win, and A. F. Molisch, "The ultra-wide bandwidth indoor channel: from statistical model to simulations," *IEEE Journal on Selected Areas in Communications*, vol. 20, no. 6, pp. 1247–1257, 2002.
- [7] A. F. Molisch, D. Cassioli, C. C. Chong et al., "A comprehensive standardized model for ultrawideband propagation channels," *IEEE Transactions on Antennas and Propagation*, vol. 54, no. 11, pp. 3151–3166, 2006.
- [8] J. Kunisch and J. Pamp, "Measurement results and modeling aspects for the UWB radio channel," in *Proceedings of the IEEE Ultra Wide-Band Systems and Technologies (UWBST '02)*, pp. 19–23, 2002.
- [9] J. Karedal, S. Wyne, P. Almers, F. Tufvesson, and A. F. Molisch, "Statistical analysis of the UWB channel in an industrial environment," in *Proceedings of the 60th IEEE Vehicular Technology Conference (VTC '04)*, vol. 1, pp. 81–85, September 2004.
- [10] W. Wilson, *Linear System Theory*, Prentice Hall, 1996.
- [11] M. M. Olama, K. K. Jaladhi, S. M. Djouadi, and C. D. Charalambous, "Recursive estimation and identification of time-varying long-term fading channels," *Research Letters in Signal Processing*, vol. 2007, Article ID 17206, 5 pages, 2007.
- [12] M. M. Olama, L. Yanyan, S. M. Djouadi, and C. D. Charalambous, "Time varying wireless channel modeling, estimation, identification, and power control from measurements," in *Proceedings of the American Control Conference (ACC '07)*, pp. 3100–3105, July 2007.
- [13] M. M. Olama, S. M. Djouadi, and C. D. Charalambous, "Stochastic differential equations for modeling, estimation and identification of mobile-to-mobile communication channels," *IEEE Transactions on Wireless Communications*, vol. 8, no. 4, pp. 1754–1763, 2009.
- [14] T. R. Field and R. J. A. Tough, "Stochastic dynamics of the scattering amplitude generating k-distributed noise," *Journal of Mathematical Physics*, vol. 44, no. 11, pp. 5212–5223, 2003.
- [15] K. E. Baddour and N. C. Beaulieu, "Autoregressive modeling for fading channel simulation," *IEEE Transactions on Wireless Communications*, vol. 4, no. 4, pp. 1650–1662, 2005.
- [16] T. Feng, T. R. Field, and S. Haykin, "Stochastic differential equation theory applied to wireless channels," *IEEE Transactions on Communications*, vol. 55, no. 8, pp. 1478–1483, 2007.
- [17] C. D. Charalambous, S. M. Djouadi, and S. Z. Denic, "Stochastic power control for wireless networks via SDEs: probabilistic QoS measures," *IEEE Transactions on Information Theory*, vol. 51, no. 12, pp. 4396–4401, 2005.
- [18] M. M. Olama, S. M. Djouadi, and C. D. Charalambous, "Stochastic power control for time-varying long-term fading wireless networks," *Eurasip Journal on Applied Signal Processing*, vol. 2006, Article ID 89864, 2006.
- [19] Y. Li, M. Olama, S. Djouadi, A. Fathy, and T. Kuruganti, "Stochastic UWB wireless channel modeling and estimation from received signal measurements," in *Proceedings of the IEEE Radio and Wireless Symposium (RWS '09)*, pp. 195–198, January 2008.
- [20] A. A. M. Saleh and R. A. Valenzuela, "A statistical model for indoor multipath propagation," *IEEE Journal on Selected Areas in Communications*, vol. 5, no. 2, pp. 128–137, 1987.
- [21] S. Venkatesh, J. Ibrahim, and R. M. Buehrer, "A new 2-cluster Model for indoor UWB channel measurements," in *Proceedings of the IEEE Antennas and Propagation Society International Symposium*, pp. 946–949, June 2004.
- [22] S. M. Djouadi, M. M. Olama, and Y. Li, "Optimal approximation of the impulse response of wireless channels by stochastic differential equations," *IEEE Signal Processing Letters*, vol. 15, pp. 896–899, 2008.
- [23] R. Schatten, *Norm Ideals of Completely Continuous Operators*, Springer, Berlin, Germany, 1960.
- [24] E. Schmidt, "Zur Theorie der linearen und nicht linearen Integralgleichungen," *Mathematische Annalen*, vol. 64, no. 2, pp. 161–174, 1907 (German).
- [25] K. J. Astrom, *Introduction to Stochastic Control Theory*, Dover Publications, New York, NY, USA, 1970.
- [26] M. D. Yacoub, J. E. V. Bautista, and L. Guerra de Rezende Guedes, "On higher order statistics of the Nakagami-m distribution," *IEEE Transactions on Vehicular Technology*, vol. 48, no. 3, pp. 790–794, 1999.
- [27] N. C. Beaulieu and C. Cheng, "Efficient nakagami- \mathcal{M} fading channel simulation," *IEEE Transactions on Vehicular Technology*, vol. 54, no. 2, pp. 413–424, 2005.
- [28] C. Zhang, M. Kuhn, B. Merk, M. Mahfouz, and A. E. Fathy, "Development of an UWB indoor 3D positioning radar with millimeter accuracy," in *Proceedings of the IEEE MTT-S International Microwave Symposium Digest*, pp. 106–109, June 2006.
- [29] E. Fishler and H. V. Poor, "Estimation of the number of sources in unbalanced arrays via information theoretic criteria," *IEEE Transactions on Signal Processing*, vol. 53, no. 9, pp. 3543–3553, 2005.
- [30] P.-J. Chung, J. F. Böhme, A. O. Hero, and C. F. Mecklenbräuker, "Detection of the number of signals using a multiple hypothesis test," in *Proceedings of the Sensor Array and Multichannel Signal Processing Workshop*, pp. 221–224, July 2004.
- [31] A. Quinlan, J.-P. Barbot, P. Larzabal, and M. Haardt, "Model order selection for short data: an Exponential Fitting Test (EFT)," *Eurasip Journal on Advances in Signal Processing*, vol. 2007, Article ID 71953, 11 pages, 2007.
- [32] E. Radoi and A. Quinquis, "A new method for estimating the number of harmonic components in noise with application in high resolution radar," *Eurasip Journal on Applied Signal Processing*, vol. 2004, no. 8, pp. 1177–1188, 2004.
- [33] B. Sklar, *Digital Communications: Fundamentals and Applications*, Prentice Hall, 2nd edition, 2001.

Research Article

A TDL Based Non-WSSUS Vehicle-to-Vehicle Channel Model

Yan Li,¹ Bo Ai,¹ Xiang Cheng,² Siyu Lin,³ and Zhangdui Zhong¹

¹ State Key Laboratory of Rail Traffic Control and Safety, Beijing Jiaotong University, No. 3 Shang Yuan Cun, Haidian District, Beijing 100044, China

² School of Electronics Engineering and Computer Science, Peking University, No. 5 Yiheyuan Road, Haidian District, Beijing 100871, China

³ School of Electronic and Information Engineering, Beijing Jiaotong University, No. 3 Shang Yuan Cun, Haidian District, Beijing 100044, China

Correspondence should be addressed to Bo Ai; aibo@ieee.org

Received 9 July 2013; Accepted 18 October 2013

Academic Editor: César Briso Rodríguez

Copyright © 2013 Yan Li et al. This is an open access article distributed under the Creative Commons Attribution License, which permits unrestricted use, distribution, and reproduction in any medium, provided the original work is properly cited.

This paper proposes a non-wide-sense-stationary-uncorrelated scattering (WSSUS) channel model for vehicle-to-vehicle (V2V) communication systems. The proposed channel model is based on the tapped-delay line (TDL) structure and considers the correlation between taps both in amplitude and phase. Using the relationship between the correlation coefficients of complex Gaussian, Weibull, and Uniform random variables (RVs), the amplitude and the phase of taps with different delays are modeled as correlated RVs to reflect the non-WSSUS properties of V2V channels. The effectiveness of the proposed channel model and simulation method is validated by the measurements in different scenarios.

1. Introduction

Vehicle-to-vehicle (V2V) communication system is a promising part of Intelligent Transportation Systems (ITS) [1], which can provide various of information services, such as the accident notification and the real-time road traffic reports, to improve the safety and the efficiency of the transportation system. The V2V communication system is a type of ad hoc communication network; different cars can exchange information with each other to provide a comfort and “infotainment” environment for driver. The IEEE 802.11p is a new V2V communication standard in the 5.9 GHz Unlicensed National Information Infrastructure (UNII) band, which is an approved amendment to the IEEE 802.11a standard by adding some extended functions to adapt to vehicle communication environment. IEEE 802.11p has been admitted as the communication standard for dedicated short range communications (DSRC) of the ITS in USA [2].

Channel modeling is the foundation for design and simulation of communication systems, whose accuracy plays a key role in optimizing and improving the performance of V2V communication systems [3]. The propagation characteristics of V2V channels in different scenarios, such as in the urban,

the suburban, and the highway, are quite different from those of traditional cellular channels. The characteristics of V2V channels contain (i) both the transmitter and the receiver are moving, (ii) the significant scatterers/reflectors are also changing continuously, (iii) the omnidirectional antennas for both Tx and Rx are at low heights, and (iv) the environment changes dynamically as vehicles move. In traditional channel modeling, the wide-sense stationary uncorrelated scattering (WSSUS) assumption has been widely used to describe random linear time-varying cellular channels [4]. In V2V channels, due to the dynamically changing environment, the statistics of channel changes over moderate time scales (non-WSS); due to the several taps interacting with one-and-the-same object, such as buildings on the road side, the taps at different delays show correlated fading property (non-US). Therefore, the WSSUS assumption is not valid for accurate description of V2V radio communication channels. This specific characteristics of V2V channels are not adequately reproduced by standard TDL models, which leads us to characterize the non-WSSUS properties of V2V channels by developing a non-WSSUS channel model.

To fill the aforementioned gap, this paper proposes a new TDL based non-WSSUS V2V channel model that for the first

time considers the amplitude and phase correlations between different taps. Using the relationship between the correlation coefficients of complex Gaussian, Weibull, and Uniform random variables (RVs), correlated taps are generated with arbitrary amplitude and phase correlation coefficients, arbitrary fading parameters, and arbitrary energies. In this model, the correlated taps represent the correlation at different delays, which is caused by the several taps interacting with one-and-the-same object. The model multiplies the switching function $z_l(t) = \{0, 1\}$ with the first-order two-state Markov chains to represent the non-WSS properties, which is caused by the short-time averaged power associated with a reflector fluctuates and the delays of the channel taps drift as the distances between the transmitter and the receiver.

The remainder of this paper is organized as follows. In Section 2, we review the related works of V2V channel models. In Section 3, we review the TDL models and the characteristics of V2V channels. Section 4 proposes a new non-WSSUS V2V channel model, whose taps at different delays are correlated in both the amplitude and phase. Section 5 validates the accuracy of the proposed channel model and evaluates the performances of OFDM systems under the condition of V2V channels.

2. Related Work

There are many literatures focusing on developing accurate models for V2V channels. V2V channel models can be classified as two classes, the geometry-based deterministic models (GBDMs) and the stochastic models, while the stochastic models can be further categorized as the geometry-based stochastic models (GBSMs) and the nongeometrical stochastic models (NGSMs) [5]. The GBDMs characterize typical channel parameters in a deterministic approach. A GBDM based on ray-tracing methods for V2V systems is the pioneering work by Maurer et al. [6, 7]; this model aims at developing a site-specific and actual physical radio propagation process for a given environment. However, the model cannot easily be generalized to more scenarios [8]. The GBSMs are used to simulate the channel by predefined stochastic distribution of effective scatters around the transmitter and the receiver. The GBSMs can be further divided into the regular-shaped GBSMs and the irregular-shaped GBSMs. The simplest regular-shaped GBSM is the two-ring model, which is proposed by Akki and Haber [9]. The two-ring and ellipse model constructs the received signal as a sum of the line-of-sight, single, and double bounced rays with different energies [10]. The classic two-ring model assumes that all scatters are placed in the horizontal plane, while in reality the scatters and reflectors are in different heights. Then the two-ring model is extended to the three-dimensional model, which places the scatters in the two-concentric cylinder around the transmitter and the receiver [11]. In the irregular-shaped GBSMs model, mobile discrete scatters, static discrete scatters, and diffuse scatters are randomly generated [12]. Due to the static nature of the geometry, the GBSMs can generalize to more scenarios; however, the model cannot represent the non-WSSUS properties of the

V2V channels. NGSMs determine the model parameters in a completely statistic manner with a certain delay and Doppler shift. In NGSMs, the impulse response of the V2V channel is modeled with taps at certain delays; hence the channel is modeled based on the tapped-delay line (TDL) structure [4]. The sum-of-sinusoids (SoS) simulation method can be used to simulate the V2V channel models [13]. Furthermore, the wideband channel model and channel statistics are discussed in [14, 15]. Among all kinds of channel models, NGSMs are widely used to mimic non-WSSUS for V2V channels due to its low complexity and acceptable accuracy.

IEEE 802.11p employs the 6-tap and 12-tap NGSMs [16, 17] as basic channel model; each tap consists of several paths, and each path has different types of Doppler spectrum (flat shape, round shape, classic 3 dB shape, and classic 6 dB shape). This allows almost arbitrary Doppler spectrum to be synthesized for each tap. However, these models are based on the WSSUS assumption, since they assume that the different taps in TDL structure are independent and uncorrelated to each other. David and coworkers describe the non-WSS property of channel by modeling multipath component persistence via Markov chains [18]. Over moderate time scales, the scatters and reflectors will be “Death and Birth” caused by dynamic blockage or obstacles nearby; the model describes the non-WSS phenomenon by random on/off process. Furthermore, the model generates multivariate Weibull variables with arbitrary fading parameters, arbitrary average fading powers, and arbitrary amplitude correlations to represent the non-WSSUS properties, while none of the above models considers the complex correlations between different taps, including both the amplitude correlations and the phase correlations. To accurately describe the channel characteristics of V2V communication systems, the V2V channel should be modeled as non-WSSUS process.

3. Channel Models

In this section, we first review the traditional TDL based models and discuss the non-WSS and non-US properties of V2V channels. Then the TDL based V2V channel model is proposed to represent the non-WSSUS properties.

3.1. TDL Based Models. The TDL based models are originated from the assumption that the resolvable taps of channels can be approximated as discrete taps with different delays [4]. The models are used to represent the WSSUS linear randomly time-varying channel. The channel impulse response (CIR) of the TDL models can describe completely the channel characteristics, which can be denoted as

$$\begin{aligned}
 h(\tau, t) &= \sum_{l=0}^{L(t)-1} \alpha_l(t) \delta[\tau - \tau_l(t)] \\
 &\quad \times \exp\{j[\omega_{D,l}(t)(t - \tau_l(t)) - \omega_c(t)\tau_l(t)]\} \\
 &= \sum_{l=0}^{L(t)-1} g_l(t) \delta[\tau - \tau_l(t)],
 \end{aligned} \tag{1}$$

where l represents the index of taps, $\alpha_l(t)$ represents the l th ($l = 1, \dots, L$) resolved amplitude, the exponential term represents the phase of the l th tap, and $\tau_l(t)$ represents the express delay of the l th tap. $\omega_c = 2\pi f_c$ is the radian carrier frequency; $\omega_{D,l}(t) = 2\pi f_{D,l}(t)$, where $f_{D,l}(t) = v(t)f_c \cos[\theta_l(t)]/c$ is the Doppler frequency induced by the motion of the Tx and Rx, $v(t)$ denotes the relative velocity, $\theta_l(t)$ is the aggregate phase angle of all components arriving in the l th tap, and c is the speed of light. The TDL model is illustrated in Figure 1.

In V2V channels, due to the dynamic environment and large obstacles, the channels are non-WSSUS. Traditional TDL models assume that the taps are independent, while this assumption cannot be hold in V2V channels.

3.2. Non-WSSUS Model. In V2V channels, the transmitter, receiver, reflectors, and scatters around are mobile, so the propagation environment changes dynamically. The significant characteristics of V2V channels are non-WSS and non-US. Non-WSS property describes the channel stochastic characteristics changed with time scale, which represents the time domain characteristics. While non-US property reflects the impacts of correlation on different paths, which represents the delay domain characteristics. In V2V channels, the scatterers and the reflectors will be “Death and Birth” over moderate time scales, which can be modeled by the multipath component persistence as a random on/off process. It can be described as the first-order two-state Markov chains [18]

$$\mathbf{TS} = \begin{bmatrix} p_{00} & p_{01} \\ p_{10} & p_{11} \end{bmatrix}, \quad \mathbf{SS} = \begin{bmatrix} p_0 \\ p_1 \end{bmatrix}, \quad (2)$$

where \mathbf{TS} is the state transition matrix, p_{uv} is the transition probability of transition from state u to state v , the state 0 represents the existence of taps, and state 1 represents the disappearance of taps. The \mathbf{SS} represents the steady-state matrix and p_u represents the steady-state probability of state u , which satisfies $p_{00} + p_{01} = 1$, $p_{10} + p_{11} = 1$, and $p_0 + p_1 = 1$.

The state decision interval of “Death and Birth” state is defined as channel coherence time $T_c = 9/16\pi f_m$, where f_m is the maximum Doppler frequency. Compared to traditional TDL models, a switching function $z_l(t) = \{0, 1\}$ is proposed to reflect the non-WSS property.

In V2V channels, the taps at different delays are correlated, due to the several taps interacting with one-and-the same object, such as buildings on the road side. As shown in Figure 2, the correlated complex Gaussian RVs can be generated with any desired correlation coefficients.

The process to generate correlated complex Gaussian RVs with correlation ρ^G from pairs of uncorrelated Gaussian RVs is as follows. (i) Generate uncorrelated complex Gaussian RVs, which are denoted as V . (ii) Determine the coloring matrix L by Cholesky decomposition of the correlation matrix $LL^H = \rho^G$ [19], where L^H is the Hermitian transpose of L . (iii) Generate correlated complex Gaussian RVs using $W = LV$. The channel correlation property can be realized with correlated taps.

According to the wireless propagation schemes between the transmitter and the receiver in V2V channels, the receivers receive the signal primarily from a particular direction

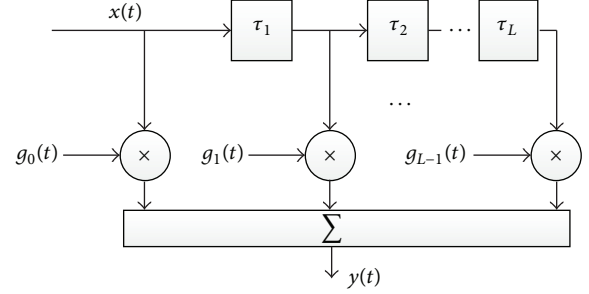


FIGURE 1: TDL based models.

through a narrow beamwidth. On the other hand, the scatters around may lead to different impacts of signal propagation toward the receiver. In the general environment of non-isotropic scattering, which corresponds to directional signal reception, the receivers receive the signal only from particular directions [20]. The uniform distribution is not suitable for the angle distribution of the taps in V2V channels, while the Laplace distribution is suitable for the description of the signal from a particular direction to the receiver. In this paper, the Laplace distribution is used to represent the angle distribution, which is an extension of the classic Uniform distribution model

$$f(x | \mu, b) = \frac{1}{2b} \exp\left(-\frac{|x - \mu|}{b}\right), \quad (3)$$

where μ is the location parameter and $b \geq 0$ which is the scale parameter referred to as the diversity.

In V2V channels, the Weibull distribution is a better fit over all empirical data than the Nakagami distribution [18]. The taps amplitude statistics can be modeled as the flexible Weibull distribution

$$f_W(\omega) = \frac{\beta}{\Omega} \omega^{\beta-1} \exp\left(-\frac{\omega^\beta}{\Omega}\right), \quad (4)$$

where β is the fading parameter. When $\beta = 2$, the Weibull distribution can be transformed to the Rayleigh distribution. With β being increased, the channel quality becomes better; when β is large enough, it means that there exists line-of-sight components. The average power is given by

$$E[W^2] = \Omega^{2/\beta} \Gamma\left[1 + \left(\frac{2}{\beta}\right)\right], \quad (5)$$

where $E(\cdot)$ is the expected value, $\Gamma(\cdot)$ is the gamma function, and $\Omega = E(\omega^\beta)$ is the power parameter. Rayleigh distribution can be transformed to Weibull distribution through the variable transformation $W = R^{2/\beta}$.

3.3. Proposed Channel Model. In this section, a TDL based non-WSSUS V2V channel model is proposed. The channel model is defined as CIR $h(\tau, t) = \sum_{l=0}^{L(t)-1} z_l(t)\alpha_l(t)e^{j\theta_l(t)}$, where the amplitude $\alpha_l(t)$ follows the Weibull distribution, the phase $\theta_l(t)$ follows the Laplace distribution, and $z_l(t)$ is the switching function. As shown in Figure 3, the model is

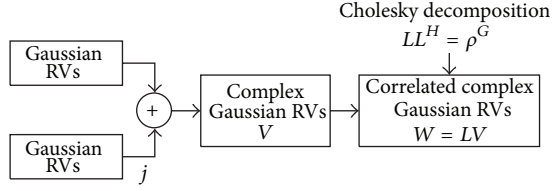


FIGURE 2: Generating correlated complex gaussian RVs.

used to generate correlated taps with arbitrary amplitude and phase correlation coefficients, fading parameters, and energy parameters.

The complex Gaussian correlation coefficients $\rho_{m,n}^{(Y)}$ can be derived with the desired Weibull correlation coefficients $\rho_{m,n}^{(W)}$, Uniform correlation coefficients $\rho_{m,n}^{(U)}$ and energy parameters Ω_m . Define $Y = ae^{j\theta}$ as complex Gaussian RVs, where the amplitude a follows Rayleigh distribution, and the phase θ follows Uniform distribution. The element $\rho_{m,n}^{(Y)}$ is the m th row and n th column of complex Gaussian correlation coefficients matrix $\rho^{(Y)}$, which is defined as

$$\rho_{m,n}^{(Y)} = \frac{E[Y_m Y_n] - E[Y_m]E[Y_n]}{\sqrt{\text{var}[Y_m] \text{var}[Y_n]}}, \quad (6)$$

where Y_m and Y_n are complex Gaussian RVs and $\text{var}(\cdot)$ denotes variance.

Since the complex random variables are generated from the independent Gaussian random variables, we can prove that the amplitude and phase of the complex random variables are independent on each other; then the first term of the numerator in (6) is given by

$$E[Y_m Y_n] = E[a_m a_n] E[e^{j\theta_m} e^{j\theta_n}]. \quad (7)$$

The Rayleigh RVs are a_m and a_n , respectively; using the transformation $R = W^{\beta/2}$ between Rayleigh RVs and Weibull RVs, the expected value $E[a_m a_n]$ is

$$E[a_m a_n] = \iint_0^\infty \omega_m^{\beta_m/2} \omega_n^{\beta_n/2} f_{W_m, W_n}(\omega_m, \omega_n) d\omega_m d\omega_n, \quad (8)$$

where $f_{W_m, W_n}(\omega_m, \omega_n)$ is the joint pdf of the bivariate Weibull distribution, which is given by [21] the following:

$$\begin{aligned} f_{W_m, W_n}(\omega_m, \omega_n) &= \frac{\beta_m \beta_n \omega_m^{\beta_m-1} \omega_n^{\beta_n-1}}{\Omega_m \Omega_n (1 - \rho_{m,n}^{(W)})} \exp \left[-\frac{1}{(1 - \rho_{m,n}^{(W)})} \times \left(\frac{\omega_m^{\beta_m}}{\Omega_m} + \frac{\omega_n^{\beta_n}}{\Omega_n} \right) \right] \\ &\times I_0 \left[\frac{2\sqrt{\rho_{m,n}^{(W)}} \omega_m^{\beta_m/2} \omega_n^{\beta_n/2}}{(1 - \rho_{m,n}^{(W)}) \sqrt{\Omega_m \Omega_n}} \right], \end{aligned} \quad (9)$$

where $I_0(x)$ is the zero-order modified Bessel function of the first kind. This joint bivariate Weibull distribution assumes

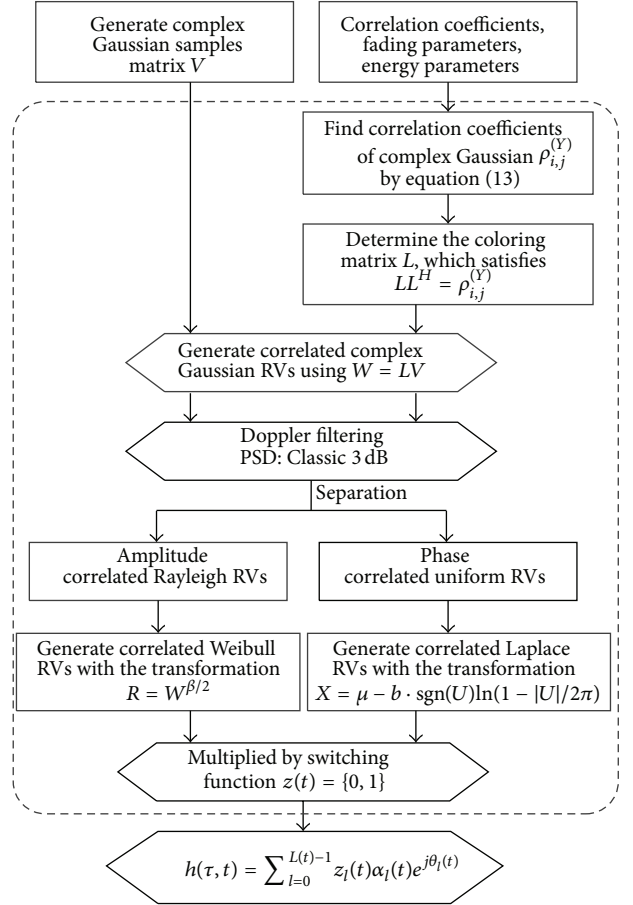


FIGURE 3: A TDL based non-WSSUS channel model.

that the correlation coefficients of the Rayleigh and Weibull RVs are identical. Even for $\beta_m = \beta_n = 2$, the joint pdf can be given by (9).

The Uniform distribution RVs are θ_m and θ_n ; then the second term of (7) is given as follows:

$$E[e^{j\theta_m} e^{j\theta_n}] = \iint_0^{2\pi} e^{j\theta_m} e^{j\theta_n} f_{U_m, U_n}(\theta_m, \theta_n) d\theta_m d\theta_n. \quad (10)$$

To calculate the joint distribution, a general family of bivariate joint distribution is proposed by Morgenstern's family found in [22] with specified marginal distributions $F_{U_m}(\theta_m)$ and $F_{U_n}(\theta_n)$ as

$$\begin{aligned} F_{U_m, U_n}(\theta_m, \theta_n) &= F_{U_m}(\theta_m) F_{U_n}(\theta_n) [1 + \alpha (1 - F_{U_m}(\theta_m)) \\ &\times (1 - F_{U_n}(\theta_n))], \end{aligned} \quad (11)$$

where $\alpha \in [-1, 1]$ is the association parameter between U_m and U_n . Then we can derive the bivariate uniform distribution which belongs to the Morgenstern's family.

Consider the following:

$$f_{U_m, U_n}(\theta_m, \theta_n) = \frac{1}{4\pi^2} \left[1 + \alpha \left(1 - \frac{\theta_m}{\pi} \right) \left(1 - \frac{\theta_n}{\pi} \right) \right], \quad (12)$$

where U_m and U_n are uniformly distributed RVs in the interval $[0, 2\pi]$. The correlation coefficients ρ for the bivariate uniform distribution under study are given by $\rho = \alpha/3$; that is, the correlation coefficients cannot exceed $1/3$.

Substitute the general expression for the joint Weibull distribution (9) into (8) to get the expectation of $E[a_m a_n]$. Use the classic expression of the joint Uniform distribution (12) into (10) to get the exponential expectation $E[e^{j\theta_m} e^{j\theta_n}]$. Then calculating (7), we can derive the element $\rho_{m,n}^{(Y)}$ of the complex Gaussian correlation coefficients matrix

$$\begin{aligned} \rho_{m,n}^{(Y)} = & -\frac{3}{8\pi} \sqrt{\Omega_m \Omega_n} (1 - \rho_{m,n}^{(W)})^2 \\ & \times \rho_{m,n}^{(U)} H\left(\left[\frac{3}{2}, \frac{3}{2}\right], 1, \rho_{m,n}^{(W)}\right), \end{aligned} \quad (13)$$

where $H(a, d, z)$ is the traditional Gaussian hypergeometric function. It is ideal to realise that the function is related to the Weibull RVs power Ω_m and the correlation coefficients $\rho_{m,n}^{(W)}$ and $\rho_{m,n}^{(U)}$.

As shown in Figure 2, generate correlated complex Gaussian RVs with the complex Gaussian correlation coefficients matrix $\rho^{(Y)}$ and the RVs of uncorrelated complex Gaussian V . The coloring matrix L can be generated by the Cholesky decomposition $LL^H = \rho^{(Y)}$; then the correlated complex Gaussian RVs are derived by $W = LV$.

Separate the correlated complex Gaussian RVs into the amplitude parts and the phase parts, where the amplitude parts follow Rayleigh distribution and the phase parts follow Uniform distribution.

Using the convenient transformation $R = W^{\beta/2}$ between Weibull and Rayleigh RVs, correlated Weibull RVs can be derived from the Rayleigh RVs.

The method for generating correlated Laplace RVs is to derive from the correlated Uniform RVs, because the convenient transformation from Uniform RVs to Laplace RVs. Assuming that U are uniformly distributed in the interval $[0, 2\pi]$, then we can find the Laplace distribution with parameters μ and b as follows:

$$X = \mu - b \cdot \text{sgn}(U) \ln\left(1 - \frac{|U|}{2\pi}\right), \quad (14)$$

where $\text{sgn}(\cdot)$ is Sgn function.

Multiply the switching function $z_l(t) = \{0, 1\}$, which is decided by the first-order two-state Markov chains illustrated in (2).

Then a TDL based non-WSSUS channel model is proposed by $h(\tau, t) = \sum_{l=0}^{L(t)-1} z_l(t) \alpha_l(t) e^{j\theta(t)}$, which considers the correlation between taps both in amplitude and phase.

4. Simulation Results and Analysis

In this section, we validate the accuracy of the TDL based non-WSSUS V2V channel model and evaluate the performances of the OFDM system under the proposed channel

model condition. Table 1 provides the channel parameters for 10 MHz bandwidth V2V channels [18]. The measurement scenarios are classified as the urban-antenna inside car (UIC), the urban-antenna outside car (UOC), the Small City (S), the open-area low traffic density (OLT), and the open-area high traffic density (OHT), which are conducted in five cities in different time and under different traffic conditions. The sum of all tap energies multiplied by their steady-state probabilities P_1 equals to unity, and the energy is concentrated in the first tap. The Weibull shape factors represent the fading property of the Weibull distribution. For the tap persistence process, we use the method of modeling an on/off process by Markov chains. $P_{uv,K}$ is the probability of transition from the state u to the state v , where the states u and v describe the existence of taps, $u = 0$ means the tap is not existing, $u = 1$ means the tap is existing, and K is the number of the tap. P_1 represents the probability of state 1 and $P_0 = 1 - P_1$ is the probability of state 0. The statistics of V2V channels change over time; the taps may be disappeared by the obstacles; then we use the random on/off process by Markov chains to describe the ‘‘Death and Birth’’ process.

Tables 2, 3, 4, 5 and 6, describe the matrices of the tap correlation coefficients for the scenarios: UIC, UOC, Small City, OHT, and OLT. Since the matrices of the correlation coefficients are symmetric about the diagonal, the tables are simplified as follows. The upper triangular part is phase correlation coefficients, which is generated randomly. The lower triangular part is amplitude correlation coefficients, which is measured from the scenarios: UIC, UOC, Small City, OHT, and OLT.

The procedure to develop a TDL based V2V channel model which considers the non-WSSUS channel characteristics is given as follows. (i) The correlated taps are generated with the amplitude and phase correlation coefficients and average energies, which represents the correlation at different delays (non-US). (ii) The amplitude and phase are separated from complex correlated taps; then the correlated Weibull RVs can be transformed from Rayleigh RVs and the correlated Laplace RVs can be transformed from Uniform RVs. (iii) Multiply the switching function $z_l(t) = \{0, 1\}$ with the first-order two-state Markov chains; the random on/off process represents the changing of fading process (non-WSS). The taps of the TDL based V2V channel model are correlated, where the amplitude of the generating taps follows Weibull distribution and the phase follows Laplace distribution. Then we calculate that the correlation coefficients matrix of the generated Weibull RVs is

$$\rho_{\text{Gen}}^{(W)} = \begin{bmatrix} 1 & 0.6255 & 0.6921 & 0.6303 \\ 0.6255 & 1 & 0.5418 & 0.4622 \\ 0.6921 & 0.5418 & 1 & 0.8130 \\ 0.6303 & 0.4622 & 0.8130 & 1 \end{bmatrix} \quad (15)$$

and the correlation coefficients matrix of the generated Uniform RVs is

$$\rho_{\text{Gen}}^{(U)} = \begin{bmatrix} 1 & 0.2705 & 0.0428 & 0.1077 \\ 0.2705 & 1 & 0.2683 & 0.1850 \\ 0.0428 & 0.2683 & 1 & 0.3069 \\ 0.1077 & 0.1850 & 0.3069 & 1 \end{bmatrix}. \quad (16)$$

TABLE 1: Channel models parameters.

TAP index K	Energy	Weibull fading factor β	$P_{00,K}$	$P_{11,K}$	P_1
UIC					
1	0.756	2.49	NA	1.0000	1
2	0.120	1.75	0.0769	0.9640	0.9625
3	0.051	1.68	0.3103	0.8993	0.8732
4	0.034	1.72	0.3280	0.8521	0.8199
5	0.019	1.65	0.5217	0.7963	0.7017
6	0.012	1.6	0.6429	0.7393	0.5764
7	0.006	1.69	0.6734	0.6686	0.4971
UOC					
1	0.88	3.19	NA	1.0000	1.0000
2	0.08	1.61	0.2717	0.9150	0.8956
3	0.03	1.63	0.4401	0.8171	0.7538
4	0.01	1.73	0.5571	0.7488	0.63825
Small city					
1	0.90	3.95	NA	1.0000	1.0000
2	0.08	1.91	0.4839	0.9446	0.9034
3	0.02	2.02	0.3452	0.7712	0.7383
OHT					
1	0.95	4.3	NA	1.0000	1.0000
2	0.04	1.64	0.3625	0.8366	0.7960
3	0.01	1.89	0.5999	0.6973	0.5696
OLT					
1	0.96	5.15	NA	1.0000	1.0000
2	0.04	1.63	0.3836	0.8525	0.8073

TABLE 2: Correlation matrix for UIC (lower/upper triangular part: amplitude/phase).

m, n	1	2	3	4	5	6	7
1	1.00	0.1328	0.2456	0.3106	0.2238	0.1092	0.1464
2	0.1989	1.00	0.2052	0.1478	0.0146	0.2508	0.1325
3	0.0555	0.1477	1.00	0.0254	0.3209	0.2981	0.1460
4	0.0481	0.1495	0.2298	1.00	0.1591	0.0769	0.3258
5	0.0977	0.0974	0.0106	0.2189	1.00	0.1471	0.1504
6	0.1074	0.2329	0.1368	0.2088	0.16	1.00	0.2059
7	0.3504	0.1999	0.1496	0.1143	0	0.26	1.00

A commonly used method to evaluate the performance is the mean-square error (MSE) between the estimated and the desired data

$$\text{MSE} = \frac{1}{L} \sum_{l=1}^L (\hat{Y}_l - Y_l)^2. \quad (17)$$

To evaluate the accuracy of the TDL based V2V channel model, we employ the UOC channel parameters to generate non-WSSUS channel model. The desired correlation coefficients matrix is in Table 3, and the generated correlation coefficients matrix is $\rho_{\text{Gen}}^{(W)}$ and $\rho_{\text{Gen}}^{(U)}$. The MSE between the desired correlation coefficients matrix and the generated correlation coefficients matrix can be used to show the

performance of the TDL based non-WSSUS V2V channel model. The MSE in matrix form is

$$\text{MSE}^{(W)} = \begin{bmatrix} 1 & 2.49 & 1.67 & 3.16 \\ 2.49 & 1 & 2.75 & 1.73 \\ 1.67 & 2.75 & 1 & 2.28 \\ 3.16 & 1.73 & 2.28 & 1 \end{bmatrix} \times 10^{-2}, \quad (18)$$

$$\text{MSE}^{(U)} = \begin{bmatrix} 1 & 1.42 & 2.55 & 1.30 \\ 1.42 & 1 & 2.14 & 1.71 \\ 2.55 & 2.14 & 1 & 0.92 \\ 1.30 & 1.71 & 0.92 & 1 \end{bmatrix} \times 10^{-2},$$

where the matrix $\text{MSE}^{(W)}$ is the MSE of the amplitude correlation coefficients matrix and the matrix $\text{MSE}^{(U)}$ is the MSE of the phase correlation coefficients matrix. The MSE

TABLE 3: Correlation matrix for UOC (lower/upper triangular part: amplitude/phase).

m, n	1	2	3	4
1	1.00	0.2831	0.0243	0.1355
2	0.6898	1.00	0.3046	0.1430
3	0.6518	0.4922	1.00	0.2741
4	0.5772	0.5142	0.8479	1.00

TABLE 4: Correlation matrix for Small City (lower/upper triangular part: amplitude/phase).

m, n	1	2	3
1	1.00	0.3011	0.2056
2	0.0338	1.00	0.1044
3	0.6813	0.0684	1.00

TABLE 5: Correlation matrix for OHT (lower/upper triangular part: amplitude/phase).

m, n	1	2	3
1	1.00	0.2152	0.0240
2	0.5441	1.00	0.3026
3	0.4157	0.1707	1.00

TABLE 6: Correlation matrix for OLT (lower/upper triangular part: amplitude/phase).

m, n	1	2
1	1.00	0.1044
2	0.1977	1.00

specifies that the generated taps have a good approximation to the desired correlated taps.

The accuracy of the proposed channel model with respect to measurements is compared with the basis of the simulated power delay profiles (PDPs). In Figure 4, we compare the PDPs of the proposed channel model with measurements in scenarios: UIC, UOC, Small City, OHT, and OLT. The spread delay in UIC scenario is more severe than others, because the UIC scenario is antenna inside the car, which leads to more obstacles in channel propagation. In OLT scenario, which is low traffic density, the scattering and reflection caused by moving cars are less than other scenarios, the spread delay is short, and the energies are centered in the first tap. The simulation results of PDPs are consistent with the measurements, which validates that the proposed channel model can accurately represent the non-WSSUS properties of V2V channels.

Furthermore we evaluate the performances of the OFDM systems under the proposed channel model condition. In simulation, the data rate is 20 Mb/s, the subcarrier number is $N = 64$, the cyclic prefix number is $N_{cp} = 16$, and channel bandwidth is under 10 MHz. The simulation of the TDL based non-WSSUS channel model in OFDM system is always compared on the basis of bit error ratio (BER).

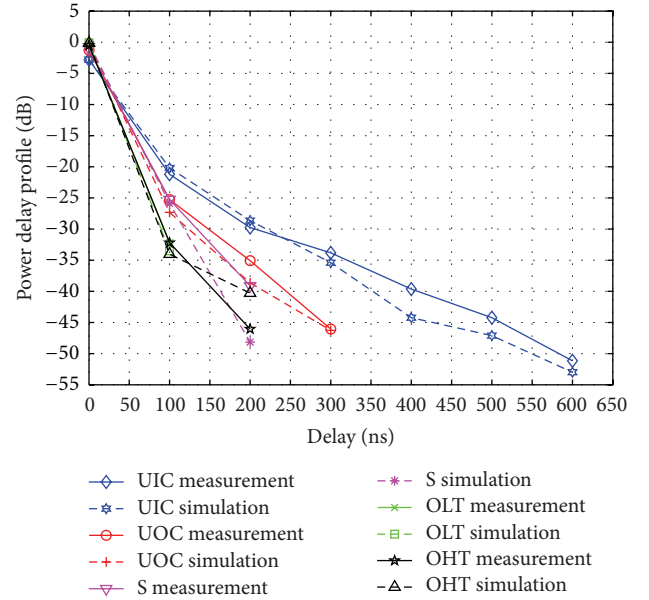


FIGURE 4: Power delay profile of the TDL based non-WSSUS V2V channel model in OFDM system (five scenarios: UIC, UOC, Small City, OLT, and OHT).

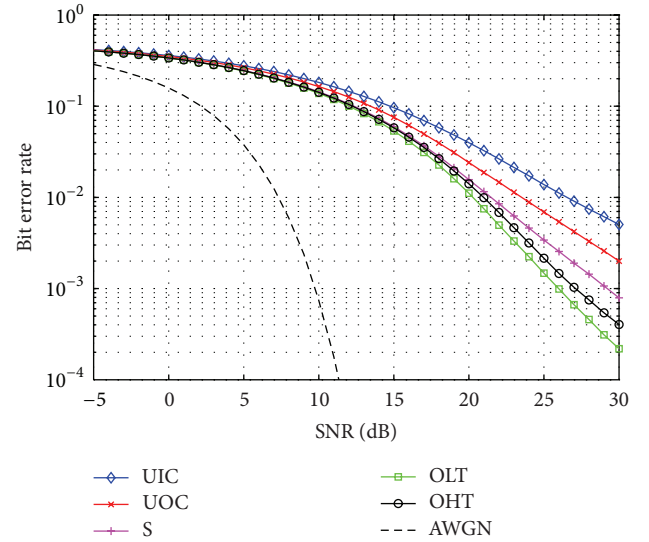


FIGURE 5: Bit error rate of the TDL based non-WSSUS V2V channel model in OFDM systems (five scenarios: UIC, UOC, Small City, OLT, and OHT).

Comparing the BER of simulating five scenarios and AWGN channels in Figure 5.

The presented results have been calculated with a SNR of -5 and 30 dB; it is clear that OLT scenario channel condition is the best and UIC scenario channel condition is the worst. The reason is that OLT is open-area low traffic density scenario; the obstacles such as moving cars are less than other scenarios; UIC is antenna inside the car; the propagation paths are all through the transmitter and receiver cars, which causes severe fading and strong reflections. Due

to the antenna inside the car, the channel condition of the UIC scenario presents a large spread delay and achieves the highest BER. The low traffic scenario presents a short delay spread and no further multipath contributions thus achieving a small BER.

5. Conclusions

In this paper, a TDL based channel model that characterized the non-WSSUS properties of V2V communications is proposed. The taps with different delays are correlated both in amplitude and phase. Utilizing the relationship between the correlation coefficients of complex Gaussian, Weibull, and Uniform RVs, the correlated taps are generated with arbitrary amplitude and phase correlation coefficients, fading parameters, and energy parameters. Using the MSE to evaluate the accuracy of the proposed channel model, the generated correlation coefficients are close to the desired correlation coefficients. The simulation results of the V2V channel PDPs show that the proposed channel model can simulate the V2V channel accurately and effectively.

Acknowledgments

This work is supported by the National Natural Science Foundation of China under Grant 61222105, the Fundamental Research Funds for the Central Universities under Grant 2013YJS005, Beijing Municipal Natural Science Foundation under Grant 4112048, Project of State Key Lab under Grant no. RCS2012ZT013, key Project for Railway Ministry of China under Grant 2012X008-A, interdisciplinary cooperation projects of the New-Star of Science and Technology supported by Beijing Metropolis under Grant no. xxhz201201, and the Key Grant Project of Chinese Ministry of Education under Grant 313006.

References

- [1] ITS Project, 2007, <http://www.its.dot.gov/index.htm>.
- [2] IEEE P802.11p/D2.01, "Standard for wireless local area networks providing wireless communication," in *Proceedings of the 5th European Congress Exhibition Intelligent Transportation System Services*, Hannover, Germany, June 2005.
- [3] J. Wang, S. Jia, and J. Song, "Signal vector based detection scheme for spatial modulation," *IEEE Communications Letters*, vol. 16, no. 1, pp. 19–21, 2012.
- [4] P. A. Bello, "Characterization of randomly time-variant linear channels," *IEEE Transactions on Communications*, vol. 11, no. 4, pp. 360–393, 1963.
- [5] C.-X. Wang, X. Cheng, and D. Laurenson, "Vehicle-to-vehicle channel modeling and measurements: recent advances and future challenges," *IEEE Communications Magazine*, vol. 47, no. 11, pp. 96–103, 2009.
- [6] J. Maurer, T. Fügen, T. Schäfer, and W. Wiesbeck, "A new inter-vehicle communications (IVC) channel model," in *Proceedings of the IEEE 60th Vehicular Technology Conference (VTC '04)*, pp. 9–13, September 2004.
- [7] J. Maurer, T. Fügen, M. Porebska, T. Zwick, and W. Wisebeck, "A ray-optical channel model for mobile to mobile communications," in *Proceedings of the 4th MCM COST*, vol. 2100, pp. 6–8, 2008.
- [8] J. Wang, S. Jia, and J. Song, "Generalised spatial modulation system with multiple active transmit antennas and low complexity detection scheme," *IEEE Transactions on Wireless Communications*, vol. 11, no. 4, pp. 1605–1615, 2012.
- [9] A. S. Akki and F. Haber, "A statistic model for mobile-to-mobile land communication channel," *IEEE Transactions on Vehicular Technology*, vol. 35, no. 1, pp. 2–7, 1986.
- [10] X. Cheng, C.-X. Wang, D. I. Laurenson, S. Salous, and A. V. Vasilakos, "An adaptive geometry-based stochastic model for non-isotropic MIMO mobile-to-mobile channels," *IEEE Transactions on Wireless Communications*, vol. 8, no. 9, pp. 4824–4835, 2009.
- [11] A. G. Zajić and G. L. Stüber, "Three-dimensional modeling and simulation of wideband MIMO mobile-to-mobile channels," *IEEE Transactions on Wireless Communications*, vol. 8, no. 3, pp. 1260–1275, 2009.
- [12] J. Karedal, F. Tufvesson, N. Czink et al., "A geometry-based stochastic MIMO model for vehicle-to-vehicle communications," *IEEE Transactions on Wireless Communications*, vol. 8, no. 7, pp. 3646–3657, 2009.
- [13] X. Cheng, Q. Yao, C. X. Wang et al., "An improved parameter computation method for a MIMO V2V rayleigh fading channel simulator under non-isotropic scattering environments," *IEEE Communications Letters*, vol. 17, no. 2, pp. 265–268, 2013.
- [14] X. Cheng, C. X. Wang, B. Ai, and H. Aggoune, "Envelope level crossing rate and average fade duration of non-isotropic vehicle-to-vehicle ricean fading channels," *IEEE Transactions on Intelligent Transportation*, no. 99, pp. 1–11.
- [15] X. Cheng, Q. Yao, M. Wen, C. X. Wang, L. Song, and B. Jiao, "Wideband channel modeling and ICI cancellation for vehicle-to-vehicle communication systems," *IEEE Journal on Selected Areas in Communications*, vol. 31, no. 9.
- [16] G. Acosta and M. A. Ingram, "Model development for the wideband expressway vehicle-to-vehicle 2.4 GHz channel," in *Proceedings of the IEEE Wireless Communications and Networking Conference (WCNC '06)*, pp. 1283–1288, April 2006.
- [17] G. Acosta-Marum and M. A. Ingram, "Six time- and frequency-selective empirical channel models for vehicular wireless LANs," *IEEE Vehicular Technology Magazine*, vol. 2, no. 4, pp. 4–11, 2007.
- [18] I. Sen and D. W. Matolak, "Vehicle-vehicle channel models for the 5-GHz band," *IEEE Transactions on Intelligent Transportation Systems*, vol. 9, no. 2, pp. 235–245, 2008.
- [19] E. Kreyszig, *Advanced Engineering Mathematics*, Wiley, New York, NY, USA, 8th edition, 1988.
- [20] J. Fühl, J.-P. Rossi, and E. Bonek, "High-resolution 3-d direction-of-arrival determination for urban mobile radio," *IEEE Transactions on Antennas and Propagation*, vol. 45, no. 4, pp. 672–682, 1997.
- [21] N. C. Sagias and G. K. Karagiannidis, "Gaussian class multivariate Weibull distributions: theory and applications in fading channels," *IEEE Transactions on Information Theory*, vol. 51, no. 10, pp. 3608–3619, 2005.
- [22] N. L. Johnson and S. Kotz, *Distributions in Statistics: Continuous Multivariate Distributions*, Wiley, New York, NY, USA, 1972.

Research Article

A Novel Transformation Electromagnetic Theory-Based Coverage Optimization Method for Wireless Network

Yuanxuan Li,¹ Gang Zhu,¹ Siyu Lin,² Ke Guan,¹ and Yan Li¹

¹ State Key Laboratory of Rail Traffic Control and Safety, Beijing Jiaotong University, Beijing, China

² School of Electronic and Information Engineering, Beijing Jiaotong University, Beijing, China

Correspondence should be addressed to Yuanxuan Li; g.liyuanxuan@gmail.com

Received 8 July 2013; Accepted 29 September 2013

Academic Editor: Ai Bo

Copyright © 2013 Yuanxuan Li et al. This is an open access article distributed under the Creative Commons Attribution License, which permits unrestricted use, distribution, and reproduction in any medium, provided the original work is properly cited.

Improving the reliability of the radio coverage in shadow area is always an important issue for the wireless communications. The emergence of the transformation electromagnetic (TE) technique provides a new method to control the propagation direction of the radio signal. This paper proposes a coverage optimization method based on the TE technique; a cloak which covers the surface of obstacle is designed to improve the coverage performance in shadow area. The material parameters of cloak are calculated by the transformation electromagnetic method. To solve the calculation problem for the rectangular obstacle, the Fourier series is used to approximately describe the rectangular boundaries. The effectiveness of the proposed cloak for the coverage optimization is validated by the theoretical analysis and simulation results. The simulation results show that the coverage performance can be improved significantly.

1. Introduction

In wireless communication systems, the electromagnetic waves cannot always transmit from the transmission antenna to the receiving antenna directly. When the obstacles block the line-of-sight path, it will bring a significant strength reduction for transmission signal [1]. The signal power may suddenly decrease in the “shadow area,” which will lead to the wireless devices losing their connections with the base station [2]. Therefore, improving the coverage quality in shadow area is an important task to ensure the requirement of quality of experience (QoE) of users.

In order to cope with the coverage problem, there are two traditional methods to improve the signal strength in the shadow area: increase the transmission power at the transmitter and deploy the relay nodes for the coverage extension [3]. Several literatures addressed the power allocation scheme for the coverage optimization in different scenarios [4–8], such as femtocell networks [4], sensor networks [5, 6], and cellular networks [7, 8]. Due to the fact that relay scheme do not need to increase the transmission power, it is suitable for the coverage extension in the shadow area. However, for the optimization of the wireless communication system, there

are two main objects: the energy-saving and the interference minimization [9–11]. To ensure the QoE of users in the shadow area, the transmitters increase their transmission power which will consume more energy for the coverage and bring a higher interference power from the adjacent cells. Moreover, the relay scheme for the coverage optimization needs more infrastructures which increase the cost of the network construction and increase the risk of security for entire networks [12, 13]. Therefore, the optimization of the network coverage is still a challenging task.

Transformation electromagnetic theory brings a new view to understand the propagation process with the electromagnetic wave. It is based on the coordinate transformations operation on the Maxwell's equations which can be interpreted as the anisotropic compression and stretching of the constituent materials in the original space [14]. By the design of the materials interpretation, the propagation direction of electromagnetic wave can be controlled. The transformation electromagnetic theory is used for an invisibility cylindrical optical-cloak in flat space [15–17]. The arbitrary geometries cloak is designed by transformation electromagnetic technique in [18, 19]. These results approved that the transformation electromagnetic theory has many advantages to design

the cloak in the optical area. So, referring to the optical results, the transformation electromagnetic theory can be extended to be use in the ultra high frequency (UHF) bands. In [20], by using the transformation electromagnetic theory, the forward and/or backward scattering of the objects is reduced to improve the antenna performance at 2 GHz. Therefore, the transformation electromagnetic techniques can be used to design a special cloak (e.g., covering the surface of obstacles) to improve the signal coverage in the shadow area. Compared with the increasing the transmission power method or the relay-assisted scheme, the transformation electromagnetic techniques bring a new method for the coverage optimization which do not need to increase the transmission power or build more network infrastructures.

In this paper, in order to solve the coverage problem in the shadow area at UHF bands, a special cloak that covers the surface of obstacles is designed to improve the performance for the signal coverage performance in the shadow area. The main contributions are summarized as follows.

- (i) An electromagnetic cloak is designed for improving the coverage performance of network. It can be used to strengthen the signal power in the shadow area without increasing the transmission power or using relay. It provides a new point of view for the coverage optimization.
- (ii) Due to the fact that shapes of most obstacles are rectangular, the rectangular cloak is designed. In order to solve the calculation problem caused by the break point in the first-order derivative in the cylindrical coordinates system, the boundary functions of the rectangular cloak are approximately expressed by the Fourier fitting method. The discussion is extended to the gap-existed cloak situation.
- (iii) The simulation results show that the strength of signal coverage will not be reduced after across the designed cloak. Therefore, the effectiveness of the coverage optimization method which is based on transformation electromagnetic theory is proved.

The rest of this paper is organized as follows. The transformation electromagnetic theory is introduced in Section 2. In Section 3, a rectangular special cloak is designed for coverage optimization. The related material properties of cloak are calculated by the transformation electromagnetic technique. The performance of rectangular cloak in current mobile bands is validated by the simulation in Section 4. Finally, the conclusions are presented in Section 5.

2. Transformation Electromagnetic Theory for Coverage Optimization

Due to the fact that one of the most common shapes of the obstacles is rectangular, we consider the case that the shadow area is caused by the blocking of the rectangular obstacle which is marked with the grid in Figure 1. The performance of the plane wave propagation is used to evaluate the improvement of the coverage. In the time-harmonic field, the electric field varies periodically and sinusoidally with

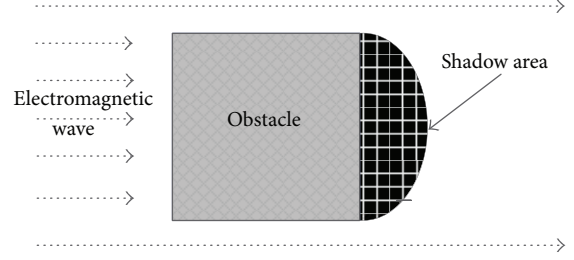


FIGURE 1: The obstacle blocks the electromagnetic waves and forms the shadow area.

time. The transformation electromagnetic theory provides a pathway to design the material parameters to control the electromagnetic wave propagation and improve the coverage reliability in the shadow area.

The transformation electromagnetic theory is based on two assumptions: the invariance of Maxwell's equations under coordinate transformations, and the material parameters in transformed coordinate system can be seen as a set of transformed material parameters in the original coordinate system [21].

In the time-harmonic field, the curl Maxwell's equations give the relationship between the electric field \mathbf{E} and the magnetic field \mathbf{H} [13]:

$$\begin{aligned}\nabla \times \mathbf{E} &= -j\omega\mu\mathbf{H}, \\ \nabla \times \mathbf{H} &= j\omega\varepsilon\mathbf{E}, \\ \mathbf{D} &= \varepsilon\mathbf{E}, \\ \mathbf{B} &= \mu\mathbf{H},\end{aligned}\tag{1}$$

where \mathbf{B} denotes the magnetic flux densities, \mathbf{D} denotes the electric flux densities, ω is angular frequency, μ denotes the electric-permittivity tensor, and ε denotes the magnetic-permeability tensor.

In the transformed coordinate system, Maxwell's equations have the same form as in the original coordinate system, which can be written as

$$\begin{aligned}\nabla \times \mathbf{E}' &= -j\omega\mu'\mathbf{H}', \\ \nabla \times \mathbf{H}' &= j\omega\varepsilon'\mathbf{E}'.\end{aligned}\tag{2}$$

The material property tensors (μ' and ε') in the transformed coordinate system are derived from the μ and ε tensor in the original space as follows:

$$\begin{aligned}\mu' &= \frac{\mathbf{A}\mu\mathbf{A}^T}{\det \mathbf{A}}, \\ \varepsilon' &= \frac{\mathbf{A}\varepsilon\mathbf{A}^T}{\det \mathbf{A}},\end{aligned}\tag{3}$$

where \mathbf{A} is the transformation matrix from the original coordinate system to the transformed coordinate system and $\det \mathbf{A}$ represents the determinant of the transformation matrix \mathbf{A} .

The transformation electromagnetic theory is based on the materials interpretation between the original coordinate system and the transformed coordinate system. Since the propagation characteristics in the media are related to the material parameters, designing the proper material parameters by the transformation electromagnetic theory can control the radio propagation in the space. Controlling with the propagation direction of electromagnetic wave by material brings a new way to consider the coverage optimization in the wireless network.

Generally speaking, the transformation electromagnetic design procedure can be summarized as follows.

- (i) Determine the model of transmission with electromagnetic wave in original coordinate system. Usually choose a plane wave propagation in the free space.
- (ii) Set a volume of space in the original coordinate system and the associated volume of space in the transformed coordinate system.
- (iii) Define the coordinate transformation from the original space to the transformed space.
- (iv) Calculate the material parameters in transformed space (the space of the cloak) via (3).
- (v) Interpret the material parameters in the original space, and obtain the desired propagation results (improve the coverage in the shadow area).

3. Design Rectangular Cloak via Transformation Electromagnetic Theory

The aim of the coverage optimization in networks is minimizing the transmission power and enlarging the coverage area (including the shadow area). In this section, a special cloak that covers the obstacle is designed to improve the coverage in the shadow area. Due to the fact that shapes of most obstacles are rectangular, the rectangular cloak is designed in this paper. It is hard to calculate the material parameters at the break point of the first-order derivative in the cylindrical coordinates system. Fortunately, the boundary functions of rectangular cloak can be expressed by calculating the approximated Fourier series boundary functions by the Fourier series fitting method. The transformed material parameters (including the electric-permittivity tensor and the magnetic-permeability tensor) are calculated by transformation electromagnetic theory by using the approximated boundary functions. The detail of design is described as the following parts.

The cylindrical coordinate system is proper to describe the original and the transformed spaces. As shown in Figure 2, the coordinate system transformation is between the original coordinate system (ρ, θ, z) and transformed coordinate system (ρ', θ', z') .

The transformed electric-permittivity tensor and the magnetic-permeability tensor are denoted by ϵ' and μ' , respectively. The electric-permittivity tensor ϵ' is transformed from ϵ . Usually, the magnetic-permeability tensor μ' equals

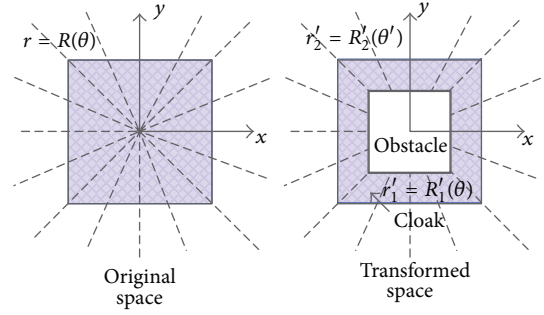


FIGURE 2: The generalized coordinate transformation.

electric-permittivity ϵ' . So, ϵ' is considered in the following analysis. The transformed electric-permittivity tensor ϵ' is

$$\epsilon' = \begin{pmatrix} \epsilon_{x'x'} & \epsilon_{x'y'} & \epsilon_{x'z'} \\ \epsilon_{y'x'} & \epsilon_{y'y'} & \epsilon_{y'z'} \\ \epsilon_{z'x'} & \epsilon_{z'y'} & \epsilon_{z'z'} \end{pmatrix}. \quad (4)$$

In the cylindrical coordinate system, the original space $r \leq R(\theta)$ is transformed into the transformed space (cloak) $R'_1(\theta') \leq r' \leq R'_2(\theta')$, where $R'_1(\theta')$ and $R'_2(\theta')$ denote the inner and the outer boundary function of cloak, respectively [18]. By the coordinate transformation, the original space $r \leq R(\theta)$ is transformed into the transformed space which can be described as

$$r' = R'_1(\theta') + \frac{R'_2(\theta') - R'_1(\theta')}{R'_2(\theta')} r, \quad \theta' = \theta, \quad z' = z. \quad (5)$$

The values of the transformed permittivity tensor for two-dimensional (2D) cloak are calculated mathematically as follows:

$$\begin{aligned} \epsilon'_{x'x'} &= \left(\left\{ [r' - R'_1(\theta')]^2 + U^2 \right\} \cos^2 \theta' \right. \\ &\quad \left. - 2Ur' \sin \theta' \cos \theta' + r'^2 \sin^2 \theta' \right) \\ &\quad \times (r' [r' - R(\theta')])^{-1}, \\ \epsilon'_{x'y'} &= \epsilon_{y'x'} \\ &= \left(\{U^2 - R'_1(\theta') [2r' - R'_1(\theta')]\} \sin \theta' \cos \theta' \right. \\ &\quad \left. + Ur' (\cos^2 \theta' - \sin^2 \theta') \right) \\ &\quad \times (r' [r' - R'_1(\theta')])^{-1}, \end{aligned}$$

$$\begin{aligned}
\varepsilon'_{y'y'} &= \left(\left[r' - R'_1(\theta') \right]^2 + U^2 \right) \sin^2 \theta' \\
&\quad + 2Ur' \sin \theta' \cos \theta' + r'^2 \cos^2 \theta' \\
&\quad \times \left(r \left[r' - R'_1(\theta') \right] \right)^{-1}, \\
\varepsilon'_{z'z'} &= \frac{r' - R'_1(\theta')}{r'} \left[\frac{R'_2(\theta')}{R'_2(\theta') - R'_1(\theta')} \right]^2, \\
\varepsilon'_{x'z'} &= \varepsilon'_{y'z'} = \varepsilon'_{z'x'} = \varepsilon'_{z'y'} = 0,
\end{aligned} \tag{6}$$

where

$$\begin{aligned}
U &= \left(\left[r' - R'_1(\theta') \right] R'_1(\theta') (dR'_2(\theta')/d\theta') \right. \\
&\quad \left. - \left[r' - R'_2(\theta') \right] (dR'_1(\theta')/d\theta') R'_2(\theta') \right) \\
&\quad \times \left(R'_2(\theta') \left[R'_2(\theta') - R'_1(\theta') \right] \right)^{-1}.
\end{aligned} \tag{7}$$

The $dR'_1(\theta')/d\theta'$ and $dR'_2(\theta')/d\theta'$ denote the first-order derivative of $R'_1(\theta)$ and $R'_2(\theta)$, respectively. When the first-order derivative of boundary function is continuous, the electric-permittivity tensor and the magnetic-permeability tensor of the cloak can be solved by (6)-(7). In fact, in wireless communication environments, many shapes do not have the first-order continual derivative of boundary function at the sharp corners (such as triangle, rectangle, and pentagon). These kinds of mathematical functions cannot be solved when calculating the results at the break point of the first-order derivative.

In traditional cellular communication scenarios, the rectangular shape is one of the most common shapes of the obstacle. Since the cloak covers the rectangular obstacle, the cloak is like a rectangular ring. The inner boundary and the outer boundary can be described as

$$\begin{aligned}
R'_1(\theta') &= \begin{cases} \frac{a}{2 \cos \theta'}, & \theta' \in \left(-\frac{\pi}{4}, \frac{\pi}{4} \right), \\ \frac{a}{2 \sin \theta'}, & \theta' \in \left(\frac{\pi}{4}, \frac{3\pi}{4} \right), \\ -\frac{a}{2 \cos \theta'}, & \theta' \in \left(\frac{3\pi}{4}, \frac{5\pi}{4} \right), \\ -\frac{a}{2 \sin \theta'}, & \theta' \in \left(\frac{5\pi}{4}, \frac{7\pi}{4} \right), \end{cases} \\
R'_2(\theta') &= \begin{cases} \frac{b}{2 \cos \theta'}, & \theta' \in \left(-\frac{\pi}{4}, \frac{\pi}{4} \right), \\ \frac{b}{2 \sin \theta'}, & \theta' \in \left(\frac{\pi}{4}, \frac{3\pi}{4} \right), \\ -\frac{b}{2 \cos \theta'}, & \theta' \in \left(\frac{3\pi}{4}, \frac{5\pi}{4} \right), \\ -\frac{b}{2 \sin \theta'}, & \theta' \in \left(\frac{5\pi}{4}, \frac{7\pi}{4} \right), \end{cases}
\end{aligned} \tag{8}$$

where a and b denote the side length of the inner rectangular boundary and the outer rectangular boundary, respectively.

There are four break points where the first-order derivative of the boundary is discontinued. Take the square shape as an example, the value of $(dR'_1(\theta')/d\theta')$ and $(dR'_2(\theta')/d\theta')$ with cloak inner boundary and outer boundary are discontinued when $\theta = \theta' = ((2n-1)\pi)/4$, $n \in N$, $\theta \in [0, 2\pi)$, and $\theta' \in [0, 2\pi)$. It is hard to get the value of electric-permittivity $\varepsilon'_{x'x'}$, $\varepsilon'_{x'y'}$, $\varepsilon'_{y'x'}$, $\varepsilon'_{y'y'}$, $\varepsilon'_{z'z'}$.

In order to solve this calculation problems, the inner boundary function $R'_1(\theta')$ and the outer boundary function $R'_2(\theta')$ of the cloak can be replaced by the Fourier approximated continuous functions with period 2π . The Fourier series can be described as

$$f(\theta') = a_0 + \sum_{n=1}^{\infty} (a_n \cos n\theta' + b_n \sin n\theta'), \tag{9}$$

where a_n and b_n are the Fourier series coefficients.

The Fourier series coefficients of the approximated boundary functions is determined by the least-square-fitting method. A number of the feature points (must include the break points, $\theta' = n\pi/4$, $n \in N$) are used to describe the boundary shape as shown in Figure 3. After using the least-square-fitting method, the a_n and b_n are determined for the approximate boundary functions. The $f_1(\theta')$ and $f_2(\theta')$ denote the inner boundary and the outer boundary, respectively. The first-order derivatives of boundary functions ($f_1(\theta')$ and $f_2(\theta')$) are the continuous functions. In Figure 4, it shows approximated boundaries of cloak which are described by $f_1(\theta')$ and $f_2(\theta')$. Then by substituting the approximated boundary functions $f_1(\theta')$ and $f_2(\theta')$ into the (6)-(7), the material parameters of the cloak can be calculated.

Based on the previous calculation, the calculation flow-chart is shown in the Figure 5. This designing method is limited not only to the rectangular cloak but also for all the shapes which have the discontinuous boundary functions in first-order derivative.

4. Electric Field Performances with the Rectangular Cloak in Wireless Communication Frequency

The rectangular cloak performances are evaluated in UHF bands. The radio frequency is chosen as 900 MHz. Since the obstacles are usually far from the base station in the cellular networks, the propagation process of electromagnetic wave can be seen as a plane wave transmission process. The cloak is assumed to cover the obstacle to enhance the coverage in shadow area, so the inner boundary of cloak has the same boundary function with the obstacle. Due to the fact that cloak performance is not related to the size of the obstacle, to facilitate processing with simulation, a small square obstacle is chosen as an example. The inner and the outer boundary functions of the cloak are denoted by $R'_1(\theta')$ and $R'_2(\theta')$.

The size of obstacle is 0.2 m \times 0.2 m. The side length of the inner boundary and the outer boundary of cloak are 0.2 m

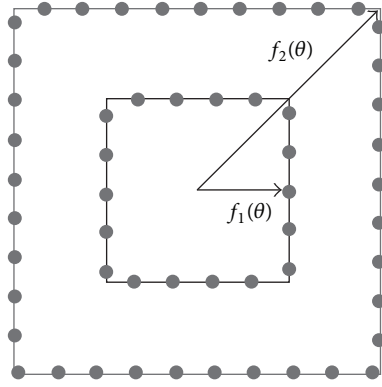


FIGURE 3: A large number of the feature points describe the boundary functions.

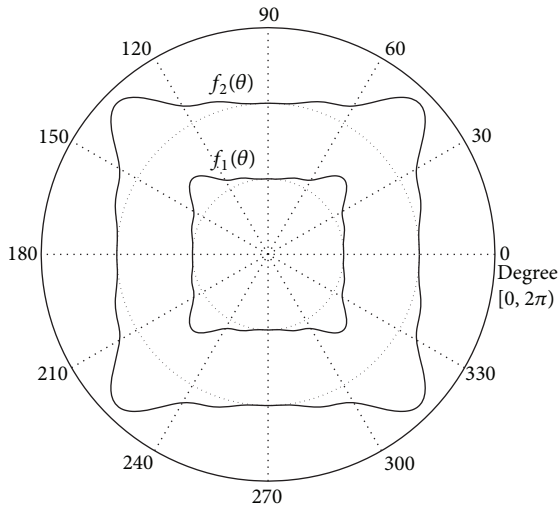


FIGURE 4: The approximate boundaries of the cloak.

and 0.4 m, respectively. The cloak boundary functions can be expressed as

$$R_1'(\theta') = \begin{cases} \frac{0.2}{2 \cos \theta'}, & \theta' \in \left(-\frac{\pi}{4}, \frac{\pi}{4}\right), \\ \frac{0.2}{2 \sin \theta'}, & \theta' \in \left(\frac{\pi}{4}, \frac{3\pi}{4}\right), \\ -\frac{0.2}{2 \cos \theta'}, & \theta' \in \left(\frac{3\pi}{4}, \frac{5\pi}{4}\right), \\ -\frac{0.2}{2 \sin \theta'}, & \theta' \in \left(\frac{5\pi}{4}, \frac{7\pi}{4}\right), \end{cases} \quad (10)$$

$$R_2'(\theta') = \begin{cases} \frac{0.4}{2 \cos \theta'}, & \theta' \in \left(-\frac{\pi}{4}, \frac{\pi}{4}\right), \\ \frac{0.4}{2 \sin \theta'}, & \theta' \in \left(\frac{\pi}{4}, \frac{3\pi}{4}\right), \\ -\frac{0.4}{2 \cos \theta'}, & \theta' \in \left(\frac{3\pi}{4}, \frac{5\pi}{4}\right), \\ -\frac{0.4}{2 \sin \theta'}, & \theta' \in \left(\frac{5\pi}{4}, \frac{7\pi}{4}\right). \end{cases}$$

There are four break points in the first-order derivative of boundary functions (both R_1' and R_2') when $\theta' = n\pi/4$ ($n = 1, 2, 3, \dots$). After using the Fourier least-square-fitting method, the approximate boundary functions of cloak are calculated as

$$\begin{aligned} R_1'(\theta') &\approx f_1(\theta') \\ &= 0.4512 - 0.06732 \cos 4\theta' + 0.02494 \cos 8\theta' \\ &\quad - 0.01553 \cos 12\theta' + 0.006722 \cos 16\theta', \\ R_2'(\theta') &\approx f_2(\theta') \\ &= 0.2256 - 0.03366 \cos 4\theta' + 0.01247 \cos 8\theta' \\ &\quad - 0.007764 \cos 12\theta' + 0.003361 \cos 16\theta'. \end{aligned} \quad (11)$$

Finally, the material parameters of cloak (ϵ' and μ') can be calculated via (6)-(7).

As shown in Figure 6, the transverse-electric (TE) plane wave transmits from the left to the right with unit amplitude. The signal strength is decreased at the back side of obstacle.

The coverage performance with cloaked obstacle is shown in Figure 7. Compared with the performance in noncloak situation, the signal strength in the shadow area with cloaked obstacle is improved. The electromagnetic wave is smoothly guided by the cloak and transmitted into the shadow area. It shows a more stable and predictable coverage performance in the shadow area.

Due to the fact that cloak cannot always keep perfectly all the time, the imperfect situation that the cloak has a gap should be considered as well. In Figure 8, there is a gap in the cloak whose width is 0.1 m. The TE plane waves transmit from the left to the right. It can be simply described as a situation that the TE plane waves transmit across a semi-infinite space which is shown in Figure 8. The electric-permittivity and magnetic-permeability in medium I and medium II are ϵ_1'' , μ_1'' and ϵ_2'' , μ_2'' , respectively. The thickness of the middle medium material is d , and the material properties are described as ϵ'' , μ'' . When the TE plane electromagnetic waves transmit from left to right ($+\hat{z}$ direction, from medium I to medium II), the reflection occurs at the place of two boundaries $z = 0$ and $z = d$. The transmission coefficient is always less than 1 [22] which means that only a part of electromagnetic waves can transmit into the medium II. When electromagnetic waves pass through the gap, a part of electromagnetic waves are blocked. As shown in Figure 9, the signal coverage performance in the shadow area is deteriorated slightly because a part of signal power is leaked into the surrounding space at the gap area.

As shown in Figure 10, the strength of the electromagnetic wave in the shadow area is compared. When the obstacle covers with the designed cloak, the signal power in the shadow area is more stable and stronger than in the case without cloaked obstacle situation. And when there is a gap on the cloak, the performance of cloak is still acceptable. The simulation results prove that the designed cloak can improve the performance of the coverage in the shadow area.

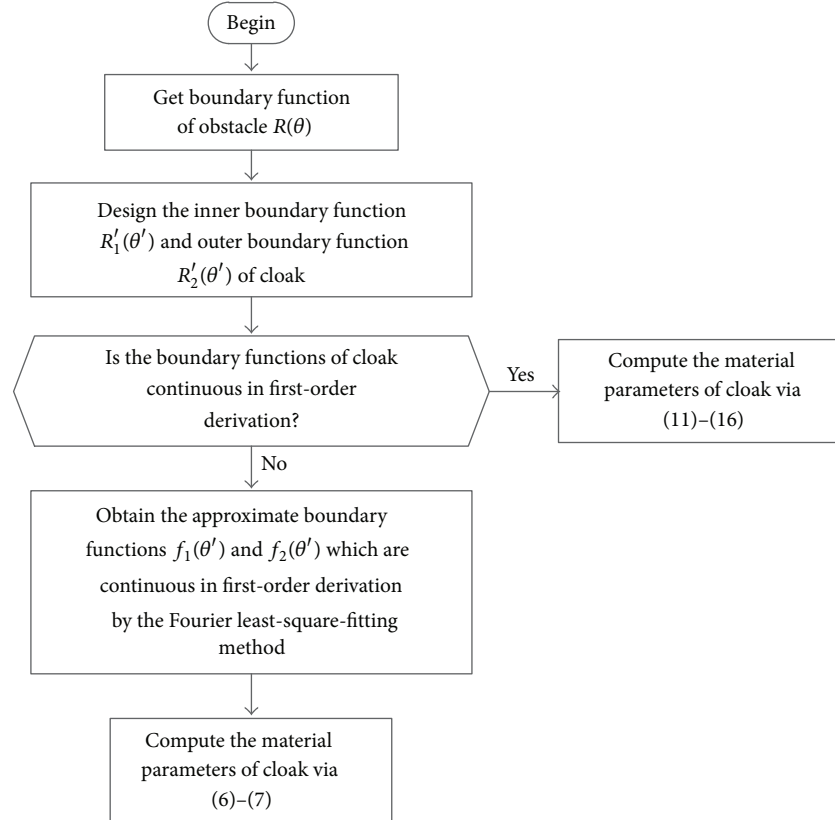


FIGURE 5: The calculation flowchart of the material parameters for the cloak.

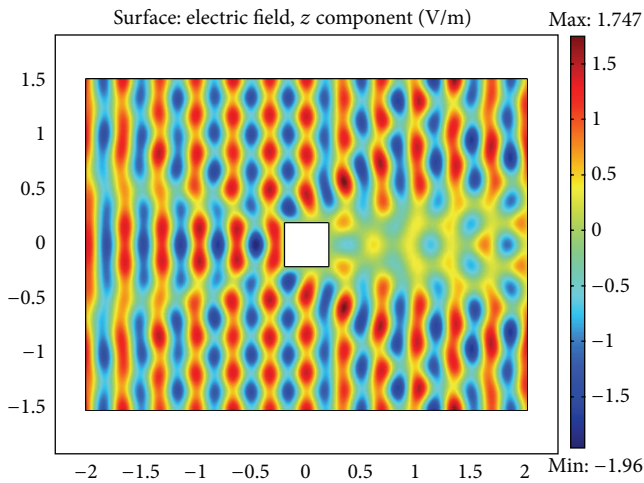


FIGURE 6: The coverage performance when the obstacle block the electromagnetic wave.

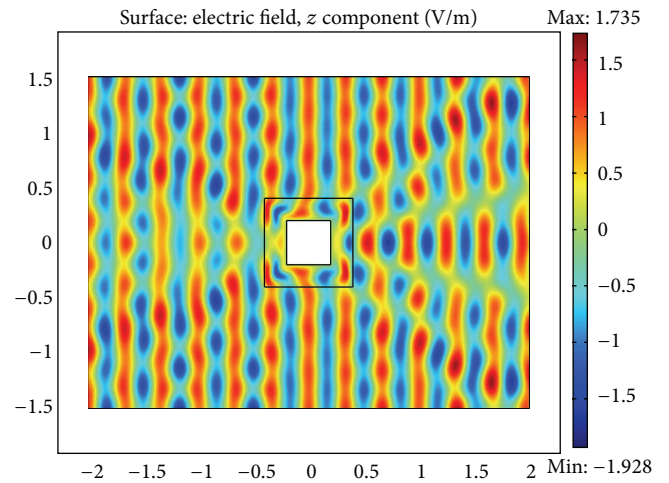


FIGURE 7: The coverage performance when using the cloak to enhance the signal strength in the shadow area.

5. Conclusion

This paper presents a special rectangular cloak design for the improvement of the signal coverage in wireless communications. In order to solve the calculation problem with the rectangular shape in the electromagnetic transformation theory, the approximated boundary functions which use the the

Fourier least-square-fitting method to approximate describe the rectangular boundary function of the rectangular cloak are proposed. The simulation results prove that the designed cloak can improve the coverage performance in the shadow area effectively. In addition, the gap-existed cloak also brings an acceptable performance in the shadow area. Compared with the transmission power optimizing or relay-assisted

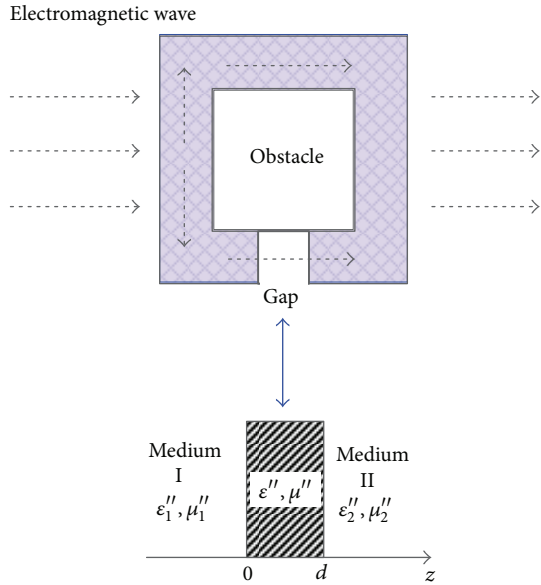


FIGURE 8: The situation of gap in the bottom of cloak.

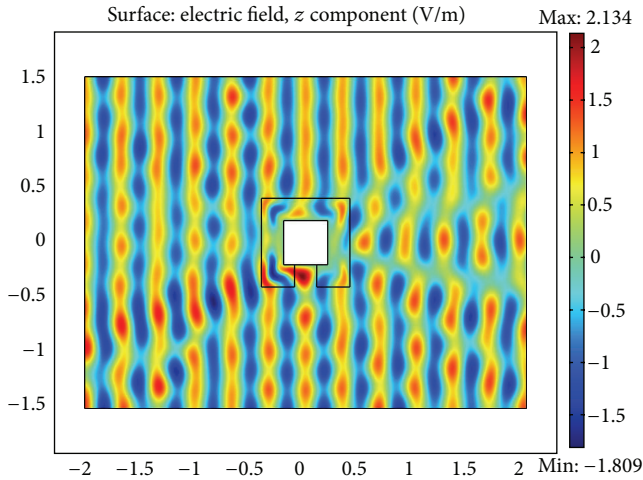


FIGURE 9: The coverage performance with the gap-existed cloak situation.

scheme, the transformation electromagnetic theory provides a new viewpoint and gives an efficient tool for the coverage optimization in the shadow area.

Acknowledgments

This work is supported by the Fundamental Research Funds for the Central Universities under Grant nos. 2012YJS017 and 2010JBZ008, Key Project of State Key Lab of Rail Traffic and Control under Grant nos. RCS2012ZZ004 and RCS2011ZZ008, the Key Grant Project of Chinese Ministry of Education no. 313006, the National Natural Science Foundation of China under Grant no. 61222105, the Natural Science Foundation of China under Grant no. U1334202, and

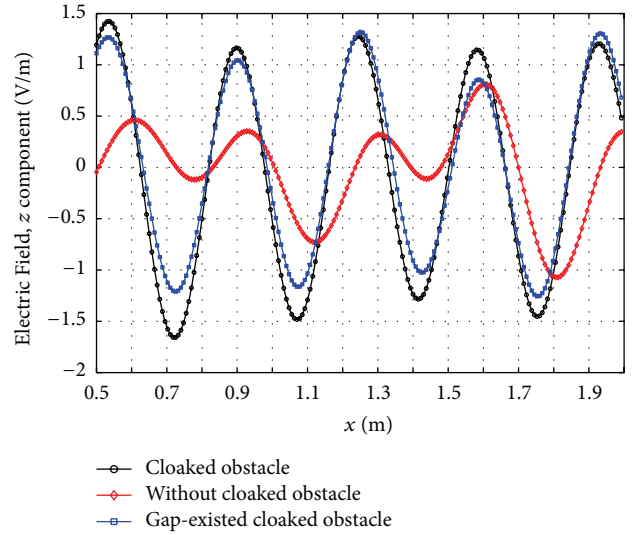


FIGURE 10: The comparison of signal strength in the shadow area.

Program for New Century Excellent Talents in University under Grant no. NCET-09-0206.

References

- [1] M. Pätzold, *Mobile Fading Channels: Modelling, Analysis, Simulation*, Wiley, New York, NY, USA, 2002.
- [2] T. S. Rappaport, *Wireless Communications: Principles and Practice*, Prentice-Hall, Endlewood Cliffs, NJ, USA, 2nd edition, 2001.
- [3] A. Goldsmith, *Wireless Communications*, Cambridge University Press, New York, NY, USA, 2005.
- [4] I. Ashraf, H. Claussen, and L. T. W. Ho, "Distributed radio coverage optimization in enterprise femtocell networks," in *Proceedings of the IEEE International Conference on Communications (ICC '10)*, May 2010.
- [5] Z. Guoping, K. Sivanand, F. Chin, and C. C. Ko, "Quality of service and coverage optimization in wireless sensor networks," in *Proceedings of the 67th IEEE Vehicular Technology Conference (VTC '08)*, pp. 2824–2828, May 2008.
- [6] J. Habibi, H. Mahboubi, and A. G. Aghdam, "A nonlinear optimization approach to coverage problem in mobile sensor networks," in *Proceedings of the IEEE Conference on Decision and Control and European Control Conference (CDC-ECC '11)*, pp. 7255–7261, December 2011.
- [7] D. Fagen, P. A. Vicharelli, and J. Weitzen, "Automated coverage optimization in wireless networks," in *Proceedings of the 64th IEEE Vehicular Technology Conference (VTC '06)*, pp. 1043–1047, September 2006.
- [8] R. Atawia, M. El Azab, T. Elshabrawy, and A. Mohamed, "Ranked overlapping coverage based construction of efficient neighboring cell list for GSM/UMTS cellular networks," in *International Conference on Communications and Information Technology (ICCIT '12)*, pp. 254–259, June 2012.
- [9] X. Cheng, Q. Yao, M. Wen, C.-X. Wang, L. Song, and B. Jiao, "Wideband channel modeling and ICI cancellation for vehicle-to-vehicle communication systems," *IEEE Journal on Selected Areas in Communication*, vol. 31, no. 9, pp. 434–448, 2013.

- [10] X. Cheng, C.-X. Wang, H. Wang et al., "Cooperative MIMO channel modeling and multi-link spatial correlation properties," *IEEE Journal on Selected Areas in Communications*, vol. 30, no. 2, pp. 388–396, 2012.
- [11] X. Cheng, C.-X. Wang, D. I. Laurenson, S. Salous, and A. V. Vasilakos, "An adaptive geometry-based stochastic model for non-isotropic MIMO mobile-to-mobile channels," *IEEE Transactions on Wireless Communications*, vol. 8, no. 9, pp. 4824–4835, 2009.
- [12] L. Xiao, T. E. Fuja, and D. J. Costello Jr., "An analysis of mobile relaying for coverage extension," in *Proceedings of the IEEE International Symposium on Information Theory (ISIT '08)*, pp. 2262–2266, July 2008.
- [13] Ö. Bulakci, S. Redana, B. Raaf, and J. Hämäläinen, "Impact of power control optimization on the system performance of relay based LTE-Advanced heterogeneous networks," *Journal of Communications and Networks*, vol. 13, no. 4, pp. 345–360, 2011.
- [14] J. B. Pendry, D. Schurig, and D. R. Smith, "Controlling electromagnetic fields," *Science*, vol. 312, no. 5781, pp. 1780–1782, 2006.
- [15] D. Schurig, J. B. Pendry, and D. R. Smith, "Calculation of material properties and ray tracing in transformation media," *Optics Express*, vol. 14, no. 21, 2006.
- [16] S. A. Cummer, B.-I. Popa, D. Schurig, D. R. Smith, and J. Pendry, "Full-wave simulations of electromagnetic cloaking structures," *Physical Review E*, vol. 74, no. 3, Article ID 036621, 2006.
- [17] M. Yan, Z. Ruan, and M. Qiu, "Cylindrical invisibility cloak with simplified material parameters is inherently Visible," *Physical Review Letters*, vol. 99, no. 23, Article ID 233901, 2007.
- [18] C. Li, K. Yao, and F. Li, "Two-dimensional electromagnetic cloaks with non-conformal inner and outer boundaries," *Optics Express*, vol. 16, no. 23, pp. 19366–19374, 2008.
- [19] W. X. Jiang, J. Y. Chin, Z. Li, Q. Cheng, R. Liu, and T. J. Cui, "Analytical design of conformally invisible cloaks for arbitrarily shaped objects," *Physical Review E*, vol. 77, no. 6, Article ID 066607, 2008.
- [20] D.-H. Kwon and D. H. Werner, "Restoration of antenna parameters in scattering environments using electromagnetic cloaking," *Applied Physics Letters*, vol. 92, no. 11, Article ID 113507, 3 pages, 2008.
- [21] D.-H. Kwon and D. H. Werner, "Transformation electromagnetics: an overview of the theory and applications," *IEEE Antennas and Propagation Magazine*, vol. 52, no. 1, pp. 24–46, 2010.
- [22] D. Su, A. Cheng, and Sh. Xie, *Electromagnetic Field and Electromagnetic Wave*, Higher Education Press, Beijing, China, 2009.

Research Article

Propagation and Wireless Channel Modeling Development on Wide-Sense Vehicle-to-X Communications

Wenyi Jiang, Ke Guan, Zhangdui Zhong, Bo Ai, Ruisi He, Binghao Chen, Yuanxuan Li, and Jia You

State Key Laboratory of Rail Traffic Control and Safety, Beijing Jiaotong University, Beijing 100044, China

Correspondence should be addressed to Ke Guan; myecone@hotmail.com

Received 22 June 2013; Revised 6 September 2013; Accepted 11 September 2013

Academic Editor: César Briso Rodríguez

Copyright © 2013 Wenyi Jiang et al. This is an open access article distributed under the Creative Commons Attribution License, which permits unrestricted use, distribution, and reproduction in any medium, provided the original work is properly cited.

The need for improving the safety and the efficiency of transportation systems has become of extreme importance. In this regard, the concept of vehicle-to-X (V2X) communication has been introduced with the purpose of providing wireless communication technology in vehicular networks. Not like the traditional views, the wide-sense V2X (WSV2X) communications in this paper are defined by including not only vehicle-to-vehicle (V2V) and vehicle-to-infrastructure (V2I) communications but also train-to-X (T2X) communications constituted of train-to-train (T2T) and train-to-infrastructure (T2I) communications. All the information related to the wide-sense V2X channels, such as the standardization, scenarios, characters, and modeling philosophies, is organized and summarized to form the comprehensive understanding of the development of the WSV2X channels.

1. Introduction

Over the past few years, both the V2X and T2X have gained popularity in their attempts to improve road safety and railway safety, respectively. As shown in Figure 1, in order to form the comprehensive understanding, V2X and T2X are collected together to constitute the complete concept—wide-sense vehicle-to-X (WSV2X). The idea behind the WSV2X communications is the deployment of wireless communication technology in vehicular and railway networks. In this manner, the vehicles, trains, and infrastructures build up a wireless network enabling them to exchange controlling and traffic information, such as road obstacles, accidents, and so forth, via the wireless communication links.

Following are the situation of the standardization and the application related to WSV2X.

- (i) Intelligent transport systems (ITSs) [1] for V2X communications: ITSs are advanced applications which, without embodying intelligence as such, aim to provide innovative services relating to different modes of transport and traffic management and enable various users to be better informed and make safer, more coordinated, and “smarter” use of transport networks. In order to realize the ITSs, Institute of Electrical and

Electronics Engineers (IEEE) and European Telecommunications Standards Institute (ETSI) have selected the same MAC and PHY layers for road traffic safety applications: IEEE 802.11p [2] and ETSI ITS G5 [3]. In the USA, in 1999, the Federal Communications Commission (FCC) allocated 75 MHz of licensed spectrum, from 5.85 to 5.925 GHz, as part of the ITS to use for Dedicated Short Range Communications (DSRC) [4]. Hence, IEEE 802.11p, part of the Wireless Access in Vehicular Environments (WAVE) initiative [5], is developed to operate at this 5.9 GHz band, with 75 MHz bandwidth and seven 10 MHz channels. In Europe, “ITS-G5 mode of operation” is defined by ETSI ES 202 663 (European profile standard for PHY and MAC layer of 5 GHz ITS), operating at the 5.9 GHz band, with 30 MHz bandwidth and five 10 MHz channels. Systems based on IEEE 802.11p as well as alternative systems are also being developed in the USA, European Union, and some Asian countries.

- (ii) For T2X communications, the three main standard systems are communication based train control (CBTC) system [6], global system for mobile communications railway (GSM-R) [7], and Terrestrial

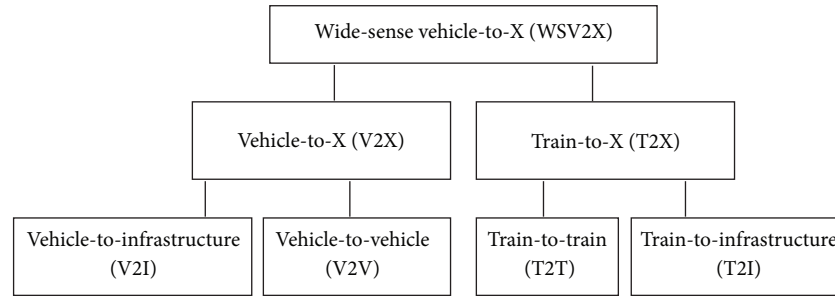


FIGURE 1: Block diagram of the constitution of the concept of wide-sense vehicle-to-X (WSV2X).

Trunked Radio (TETRA, formerly known as Trans-European Trunked Radio [8]). (i) As one part of European Train Control System (ETCS) [9], CBTC is a railway signalling system that makes use of the telecommunications between the train and track equipment for the traffic management and infrastructure control. By means of the CBTC systems, the exact position of a train is known more accurately than with the traditional signalling systems. This results in a more efficient and safe way to manage the railway traffic. Normally, CBTC works at 2.4 GHz. (ii) As a subsystem of European Rail Traffic Management System (ERTMS) [10], GSM-R is an international wireless communications standard for railway communication and applications, used for communication between train and railway regulation control centers. GSM-R is based on GSM and thus works at the 900 MHz band. In EIRENE-MORANE specifications, GSM-R can guarantee performance at speeds up to 500 km/h, without any communication loss. (iii) As a standard of ETSI, TETRA is a professional mobile radio and two-way transceiver (colloquially known as a walkie talkie) specification. TETRA was specifically designed for use by government agencies, emergency services (police forces, fire departments, and ambulance) for public safety networks, rail transportation staff for train radios, transport services, and the military. Normally, TETRA works at the 400 MHz band.

- (iii) So far, there is no official standard for T2T communications, but on the basis of the thought of the ad hoc intervehicle communication, many academic efforts have been made to achieve the direct T2T communications. The most representing system is called Railway Collision Avoidance System (RCAS) [11], studied by German Aerospace Center (DLR). Using the global satellite navigation system GALILEO, this system determines and broadcasts information about position, movement vector to other trains around in its coverage for collision detection. When a collision is detected, the train transmits prewarning messages to others to avoid the accident.
- (iv) All the standard systems mentioned above are narrowband systems or at least are only implemented at the stage of the narrowband. However, various wideband systems, such as Long Term Evolution for

Railway (LTE-R) [12, 13] and LTE for V2X communications, are researched and under industrial consideration. Railway operators do benefit from the evolution in public networks. Fulfilling train control requirements, GSM-R is based on the mature GSM technology. This success is expected to be repeated with LTE/LTE-R [14]. International Union of Railways (UIC) has commenced to generate LTE-R requirements [15]. In [16], the authors discuss several technical challenges for LTE to be used for railroad communications because of fast mobility of train up to 430 km/h. Since signalling and train control system is related to public safety, very tight reliability requirement needs to be met. Correspondingly, the wideband channel for train communication systems has carried extensive research [17]. Authors in [18] emphasize the feasibility of a smooth evolution from GSM-R to LTE-R. According to the authors, it will not affect the system while the subcarrier interval in LTE is 15 kHz, above the 11 kHz recommended. Authors in [19] propose a combination of wireless technologies to provide broadband to the train communication systems. As clarified in [20], the Doppler effect is always a matter of study in this work. Apart from the effect from the academy, many industrial companies have been pushing the standardization of LTE-R, such as the work presented by Nokia Siemens in [14], by Alcatel-Lucent in [21] and by Huawei in [22]. In the near future, the time of the wideband WSV2X communications can be expected to come. For the preparation, the wideband channel characteristics of WSV2X communications are under research by a large number of scholars.

As the basis of WSV2X systems, the propagation and channel characterization are always a fundamental topic with high research interest. In the rest of the paper, all the related information, such as the scenarios, characters, and modeling philosophies of the propagation and wireless channel of WSV2X will be summarized to offer a panorama of the recent progress and the current state of the art. The aim of this paper is to help the designers of communications systems to gain an comprehensive understanding of the pertinent channel characteristics and propagation researchers to assess where the most urgent requirements for further work lie.

Wide-sense vehicle-to-X (WSV2X)		Propagation mechanisms
Vehicle-to-X (V2X)	Train-to-X (T2X)	
 Highways	  Viaduct Water	Few scatterers present, so the direct ray and reflection from the road surface, rail surface, or the water surface (much stronger than the reflection from concrete surface, vegetation, or soil) dominate the wave propagation, making typical LOS propagation scenarios.
 Suburban streets	  Suburban Cutting  Mountain	Cutting walls can form a big container with rich reflection and scattering. Diffraction owing to the terrain changes and scattering from the surface of mountain could be the main multipath components. Not many buildings present in these scenarios.
 Rural streets	 Rural	There are few or no buildings in these two scenarios. The vegetation could serve as some scatterers, but the main propagation mechanisms are still LOS and reflection from road surface or rail surface.
 Urban streets	  Tunnel Urban  Station	The channel appears strong multipath due to the presence of buildings. Walls of the tunnel or the station generate rich reflection. This gives the chance to employ the waveguide theory to explain the propagation. In the station scenario, the huge awnings are usually designed to stop the rain from reaching the passengers and the trains. These awnings have a big chance to block the LOS.

FIGURE 2: Typical scenarios of WSV2X channels. The scenarios in the same light colorful blocks are similar or comparable.

2. Scenarios of WSV2X Channels

Channel characteristics of WSV2X channels are dominated by the properties of the scenarios in which the cars, trains, and infrastructures communicate with each other. As shown in Figure 2, there are four main scenarios for the V2X channels (highways, suburban streets, rural streets, and urban streets, defined by [23]) and nine main scenarios for the T2X channels (viaduct, water, suburban, cutting, mountain, rural, tunnel, urban, and station, defined by [24]). The influence of these scenarios on the channel characteristics has been studied by many researchers. For instance, the channel characteristics of V2X in the highways are well summarized by the authors of [23]. The multipath in the rural streets from hills [25] and forests [26] is studied as well. A preliminary table of some narrowband channel characteristics of T2X is given by [24]. For the tunnel scenario, the propagation mechanism changes along with the different distance between transmitter (Tx) and receiver (Rx). Thus, the segmentation-based thought for modeling the propagation inside tunnels has been developed and purchased by many scholars [27–35].

As shown in Figure 2, the scenarios in the blocks with the same color are comparable. They have similarities on

the characters of the environments, so the channels are expected to show similar properties. However, up to now the authors cannot find any open publication of doing the comparative study on these channels in the similar scenarios, even though each single scenario has already been well researched independently. Some common senses of the propagation mechanisms in every group of comparable V2X and T2X scenarios are summarized in Figure 2 to give some rough inspirations of the joint analysis of the V2X and T2X scenarios.

In the future, the combination of the similar V2X and T2X scenarios is expected. In this way, a unified theory of interpreting and modeling the propagation in the WSV2X channels can come true. Thus, the corresponding researchers can use the same methodology and philosophy to characterize the channel, fulfill the network planning, and design the system of WSV2X communication systems.

3. Comparison of WSV2X Channels with Cellular Communication Channels

Characteristics of WSV2X channels differ from those of traditional cellular communications channels. These differences

can be summarized in accordance with the following dimensions.

- (i) Heights of Tx and Rx: the relation of heights of Tx and Rx in T2I channels is very similar to cellular communication (CC) channels—Tx is considerably higher than Rx. However, the Tx and the Rx in V2X channel and T2T channel are normally at the same height and in similar environments (peer-to-peer communications). This leads to different constitutions of the propagation mechanisms in these channels. (i) LOS: in CC channel and T2I channel, the Tx is much higher than the Rx. So, compared with V2X and T2T channels, the LOS is relatively easier to be kept in CC channel and T2I channel. (ii) Diffraction: in CC channel and T2I channel, the wave mainly propagates in the vertical plane, so the obstructions are the roof tops of buildings, top of the cutting walls, and terrain changes. Diffraction loss can be effectively estimated by the algorithms based on raster database, such as the classic multiedge models and their improved versions [37]. However, the propagation in V2X and T2T channels mainly happens in the horizontal plane; the diffraction loss owing to street corners and buildings cannot be predicted by raster-based algorithms; vector-based algorithms, such as geometrical theory of diffraction (GTD) and uniform theory of diffraction (UTD), are required. (iii) Distributions of scatterers: normally the area around the Tx in CC channel and T2I channel is free of scatterers, but in V2X and T2T channels, scattering and reflection can come from the scatterers around both the TX and the RX.
- (ii) Frequency of communication: compared with the main frequency bands for CC channel (700–2100 MHz) and T2X channel (400 MHz, 900 MHz, and 2.4 GHz), the carrier frequency of V2X channel which is at 5.9 GHz is very high. Hence, higher signal attenuation occurs in the V2X channel, and specific propagation processes like diffraction are less efficient.
- (iii) Distance between Tx and Rx: in the typical CC and T2I channels, the distance of communication is 1–3 km; however, in V2X and T2T channels, the distance over which communications can take place is normally dozens of meters or hundreds of meters. This makes the V2X and T2T channels more local, and therefore, the scatters far from Tx and Rx can be ignored.
- (iv) Nonstationarity: in V2X and T2T channels, both Tx and Rx as well as many scatterers (other vehicles or trains) are dynamic, while in CC channels, only one of the Tx or Rx is moving, and moving scatterers have less relative importance. In T2I channels, the speed of high-speed train can achieve 350 km/h, which is dramatically faster than the velocity of the user in the CC channel. As a consequence, the channel fluctuations in WSV2X channels are faster, so that the

commonly used assumptions on stationarity usually are not valid. The WSV2X channel is the typical nonstationary channel; that is, the channel statistics change within a rather short period of time [23].

4. WSV2X Channel Characterization

In the WSV2X channel, all the propagation effects are subsumed into the channel impulse response (CIR), which can be treated as the superposition of the contributions by all multipath components (MPCs). The CIR is time-variant since the channel changes as Tx, Rx, and scatterers are moving around. A complete description of the channel is thus given by the time variant CIR [38]. In order to facilitate the processing, several metrics are extracted to provide more condensed characterization of the WSV2X channel. Generally speaking, different systems require different metrics to support the channel characteristics. In this paper, we summarize all the typical metrics by classifications of the domains they belong to and the systems they serve.

Figure 3 offers a panorama of metrics for the WSV2X channel classified in accordance with the antenna configuration, bandwidth of the system, and different domains. All the parameters can be assigned to totally six domains:

- (i) loss and fading: path loss, shadow fading, and small-scale fading,
- (ii) time domain: coherence time and stationary time,
- (iii) frequency domain: coherence bandwidth and stationary bandwidth,
- (iv) doppler domain: Doppler shift and Doppler spread,
- (v) delay domain: RMS delay spread,
- (vi) angular domain: angle of arrival (AoA) and angle of departure (AoD).

It can be seen that for the narrow-band single input single output (SISO) systems, the knowledge of path loss, shadow fading, small-scale fading, coherence time, stationary time, coherence bandwidth, stationary bandwidth, and Doppler shift is enough to characterize the channel. But for the wide-band SISO systems, Doppler spread and RMS delay spread should be compensated. When the system evolves from SISO to multi-input multioutput (MIMO), the information of the angular domain, such as AoA and AoD is mandatory to 5 characterize the spatial correlations of the subchannels.

Note that the stationary time and the stationary bandwidth are the specific parameters exclusively for the nonstationary channel. Not like the coherence time and the coherence bandwidth which are extracted from the scattering function, the stationary time and the stationary bandwidth measure the amount of Doppler and delay correlation, respectively. They characterize the local scattering function (LSF) variation with respect to time and frequency. In the WSV2X channel, the channel statistics are valid only for a short period of time (“region of stationarity” determined by the stationary time and the stationary bandwidth). For instance, in each region of stationarity, the Doppler spectrum of the first delay tap can be different, because the Doppler shift

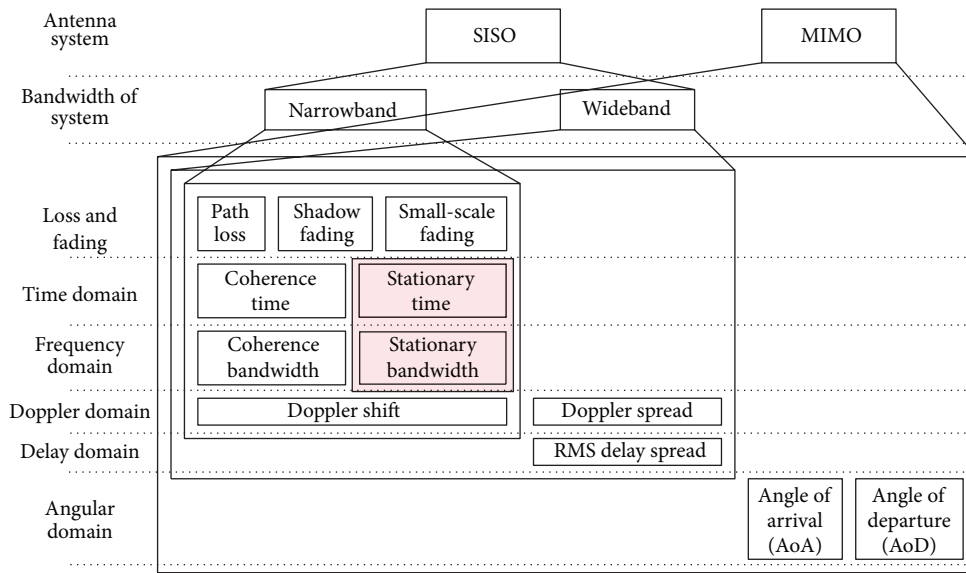


FIGURE 3: Panorama of metrics for WSV2X channel classified in accordance with the antenna configuration and bandwidth of the system and different domains. Stationary time and stationary bandwidth (in the block with light red color) are the two specific parameters in the nonstationary channel.

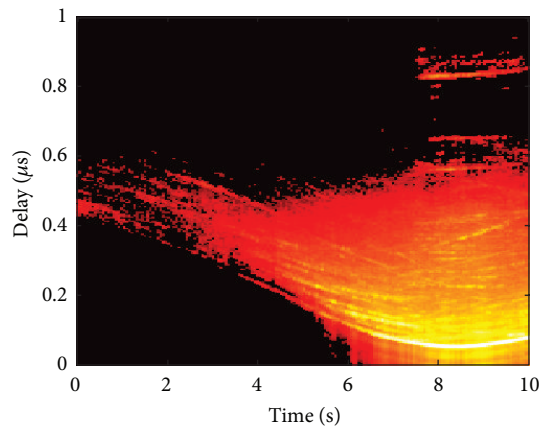


FIGURE 4: Example of the time-varying power delay profile (average squared magnitude of impulse response) in the WSV2X channel. It can be found that the delay of the first taps varies because the Tx and Rx approach each other firstly and move away from each other later. The LOS tap experiences fading, the gap in the delay domain between strong components (clusters), and the LOS tap changes with time, and there is splitting of clusters over time as well.

of the LOS component can change [23]. Figure 4 (which is the measured results in [39, 40]) gives an example of the time-varying power delay profile (average squared magnitude of impulse response) in the WSV2X channel. It can be found that the delay of the first taps varies because the Tx and Rx approach each other firstly and move away from each other later. The LOS tap experiences fading, the gap in the delay domain between strong components (clusters), and the LOS tap changes with time, and there is splitting of clusters over time as well [23].

Up till now, most of the metrics given by Figure 3 in the V2X channel have been well studied by many researchers, such as the metrics given by Table 1 in [23], where the wideband parameters, such as the delay spread and the

Doppler spread, have been extracted from extensive measurements. However, there is no deep insight or comprehensive understanding of these characters for wide-band MIMO T2X communication systems. The authors of [24] offer the narrowband parameters for T2X channels in high-speed railway at 930 MHz, but all the wideband parameters are still absent. Some researchers have started to do some efforts, such as the wideband channel characterization of LTE for high-speed railway at 2.35 GHz with the tapped delay line model [41] and the calculation of the stationary interval in high-speed railway scenario [42]. The ergodicity and the reliability of the experimental data and corresponding parameter extractions are still quite limited; more works in different scenarios at various frequencies are expected.

TABLE I: Channel characteristics of T2X, V2X, and standard scenarios.

Category	Scenarios	Path loss exponent	Standard deviation of shadowing [dB]	K -factor/Nakagami- m	Delay spread (mean) [ns]
T2X	Viaduct	2–4	2–4	K : 3.8–8.3 dB	192
V2X	Highway	1.8–4	4.0–6.1	K : 3.3–4.3 dB	30–340
V2X	Rural	1.79–4	—	—	20–150
Standard	Suburban	2.4–4.0	4–8	K : 9 dB	59–84
Standard	Rural macrocell	2.2–2.5	4–8	K : 7 dB	36.8–42.1
Standard	Moving networks BS-MRS, rural	1.9–2.2	4	K : 7 dB	40–55
T2X	Cutting	2.5–4	3–5	K : 1.88 dB	—
V2X	Suburban	2.1–3.9	—	K : 2.1 dB	20–150
Standard	Indoor to Outdoor/outdoor to indoor	2	7	K : 3.2 dB	34–40
Standard	Typical urban macrocell	2.6	4–8	K : 7 dB	85.4
T2X	Tunnel	1.8–3	5–8	m : 0.8–5.4	15–40
T2X	Station	3–5	3–5	K : 0.5–5.4 dB	—
V2X	Urban	1.61	4.2–6.7	K : 3–6.7 dB	3–1100
Standard	Indoor office/residential	1.9	3–4	K : 7 dB	14.2–43
Standard	Typical urban microcell	2.3–4	3–4	K : 9 dB	37–74
Standard	Large indoor/hall	1.4–3.8	3–4	K : 2 dB	23.7–40.8

Table 1 summarizes some channel parameters of T2X, V2X, and standard scenarios (WINNER) according to the research results of [23, 41, 43–47], respectively. Not like the traditional way of researching the scenarios of different systems independently, the similar or comparable scenarios of T2X, V2X, and standard scenarios are collected together in Table 1. There are three preliminary categories.

(i) “Relatively open scenarios”: this category is define by the scenarios with a relative wide open space but few scatterers or strong reflectors. The T2X viaduct, V2X highway, V2X rural, standard suburban, standard rural macrocell, and standard moving networks fall into this category. As shown in Table 1, the path loss exponent in this category is slightly larger than 2, similar to the case of two-ray model. This is because there are few scattering or strong reflections from the surrounding space, but the reflection from the rail surface or the road surface still contributes the power and, therefore, makes the channel close to the two-ray model. Since the LOS can be kept in most of the cases of this category, the Rician K -factor is the largest in the three categories. Furthermore, the delay spread is relatively large, because the space is wide.

(ii) “Semiclosed scenarios”: this category indicates that the scenario is surrounded by some walls, buildings, or terrain but still has some free or open space. This category is in the middle of the three categories, so

the values of the channel characteristics are basically between the “relatively open scenarios” and “relatively closed scenarios.”

(iii) “Relatively closed scenarios”: this category mainly includes the limited-space and closed scenarios, such as the T2X tunnel, T2X station, V2X urban, standard indoor office/residential, standard typical urban microcell, and standard large indoor/hall. Since these scenarios are mainly in a limited space, the delay spread is relatively small. Moreover, the tunnel walls, station structures, and building walls constitute a relatively closed space, which generates and contains the multipath waves and finally results in a relatively small Rician K -factor. Last but not least, most of the scenarios in this category have the path loss exponent smaller than 2; this indicates that certain waveguide effect is established by the surrounding walls of tunnels, stations, and buildings. This makes the path loss even smaller than the free space propagation.

This is the first effort to break the barrier of the V2X, T2X, and standard scenarios. As shown in Table 1, the new classification integrates the scenarios of different systems and redivides the categories according to the physical structure and propagation mechanisms. In the future, the comparative study is expected to gain a deeper insight to the channels in various scenarios and finally form a comprehensive concept of this work.

5. Modeling Approach for WSV2X Channel

There are primarily three types of channel modeling approaches for WSV2X channel: deterministic channel models, stochastic channel models, and geometry-based stochastic models.

5.1. Deterministic Channel Model for WSV2X Channels.

Deterministic channel models are based on ray-tracing techniques, which model the propagation channel in a specific location using the geographical and morphological information from a database. This kind of modeling approach was pioneered by Wiesbeck [48–50]. Normally, the 3D ray-optical approach covers the direct path, specular reflections, and diffuse scattering. Specular reflections can be calculated by the image method [51] up to the n th order, but in practice, only the first and second order reflections are considered in order to limit the computation time. The diffuse scattering is taken into account on surfaces seen by both the Tx and the Rx. Thus, all surfaces of the structures in the scenario, such as buildings, trees, vehicles, and traffic signs, are divided into tiles, and single scattering processes can be determined. For each ray, full-polarimetric antenna patterns are used and channel polarization matrices are computed. The output of the deterministic channel models for each communication link is a time-variant CIR $h(\tau, t)$, which well characterizes the frequency-selective channel and can be expressed as

$$h(\tau, t) = \sum_{k=1}^{N(t)} a_k(t) \cdot e^{j(2\pi f\tau_k(t) + \varphi_k(t))} \cdot \delta(\tau - \tau_k(t)), \quad (1)$$

where the k -th multipath component at time t is formulated by an amplitude $a_k(t)$, a delay $\tau_k(t)$, and an additional phase shift $\varphi_k(t)$. As the car or the train is running, the number of multipath components ($N(t)$) is also time variant. Since the amplitude and the phase term for each multipath component can be combined in a complex coefficient: $A_k(t) = a_k(t) \cdot e^{j(2\pi f\tau_k(t) + \varphi_k(t))}$, (1) can be rewritten as

$$h(\tau, t) = \sum_{k=1}^{N(t)} A_k(t) \cdot \delta(\tau - \tau_k(t)). \quad (2)$$

By involving the polarization, $A_k(t)$ can be expressed by

$$A_k(t) = L_k(t) \cdot \vec{e}(\theta_{\text{Rx},k}, \varphi_{\text{Rx},k})^H \cdot P_k \cdot \vec{e}(\theta_{\text{Tx},k}, \varphi_{\text{Tx},k}), \quad (3)$$

where the superscript H denotes the Hermitian transpose. P_k denotes the complex channel polarization matrix that includes the reflection or scattering losses of the considered path. $\vec{e}(\theta_{\text{Tx},k}, \varphi_{\text{Tx},k})$ and $\vec{e}(\theta_{\text{Rx},k}, \varphi_{\text{Rx},k})$ are the complex polarization vectors for the Tx and the Rx, respectively, that cover the gain and the polarization of the antennas at the angles of departure ($\theta_{\text{Tx},k}, \varphi_{\text{Tx},k}$) and the angles of arrival ($\theta_{\text{Rx},k}, \varphi_{\text{Rx},k}$) for the k -th multipath ray. $L_k(t)$ includes the propagation loss and the phase shift based on the delay $\tau_k(t)$ of the considered path. For the direct ray, P_k is the identity

matrix, whereas for reflected and scattered rays of the order n , P_k is derived by [52] using

$$P_k = R(\varphi_{n-m,k}) \cdot \prod_{m=0}^{n-2} (R_{n-m,k} \cdot R(\varphi_{n-m,k})) \cdot R_{1,k} \cdot R(\varphi_{\text{Tx},k}), \quad (4)$$

where $R(\varphi)$ is the rotation matrix that can be expressed as

$$R(\varphi) = \begin{pmatrix} \cos \varphi & \sin \varphi \\ -\sin \varphi & \cos \varphi \end{pmatrix}, \quad (5)$$

$\varphi_{\text{Tx},k}$ denotes the angle between the normal vector of the incidence plane and the field strength component E_θ at the first reflection or scattering point, and $\varphi_{\text{Rx},k}$ denotes the angle between the scattering or reflecting plane and E_θ at the last reflection or scattering point for the k -th multipath component, respectively. For the case of the multiple reflections or scattering, the term $\varphi_{i,k}$ denotes the angle between E_θ and the normal vector of the incidence plane at the i th reflection or scattering point for the k -th multipath ray. $R_{i,k}$ denotes the reflection or scattering matrix which is given by

$$R_{i,k} = \begin{pmatrix} r_{\perp,i,k} & \zeta_{1,i,k} \\ \zeta_{2,i,k} & r_{\parallel,i,k} \end{pmatrix}, \quad (6)$$

where the elements $r_{\perp,i,k}$ and $r_{\parallel,i,k}$ are the reflection or scattering coefficients of the surface belonging to the i th reflection or scattering point of the k -th multipath component for perpendicular and parallel components of the electric field, respectively. For reflection processes, these elements are determined based on the Fresnel equations; for scattering processes, these values depend on the radar cross-section (RCS) of the object. $\zeta_{1,i,k}$ and $\zeta_{2,i,k}$ are cross-polarization coupling coefficients, which are normally set to zero. More detailed information about the deterministic modeling approach can be found in [53, 54]. Figures 5(a) and 5(b) offer an example of a ray-tracing map of the realistic high-speed railway scenario, the partial enlarged drawing for direct, reflected, and scattering paths in one snapshot. Figure 5(c) gives a ray-tracing map of a typical urban V2V channel.

5.2. Stochastic Channel Models. The stochastic channel model does not determine the impulse response in a specific location. Rather, it models the propagation characteristics by assuming stochastic distributions of scatterers. Basically, the stochastic channel models can be divided into two types: narrowband stochastic channel models and wideband stochastic channel models.

Narrowband stochastic models do not concern the frequency selectivity of the channel but rather focus on characterization of the fading statistics as well as the Doppler spectrum. Not like the Jakes spectrum in the CC channel with a “bathtub” shape, the Doppler spectrum in V2V channels is more smoother [55, 56]. More efforts and interesting results are given in [57, 58].

Wideband stochastic channel models create the statistics of the received power with a certain delay, Doppler shift, and

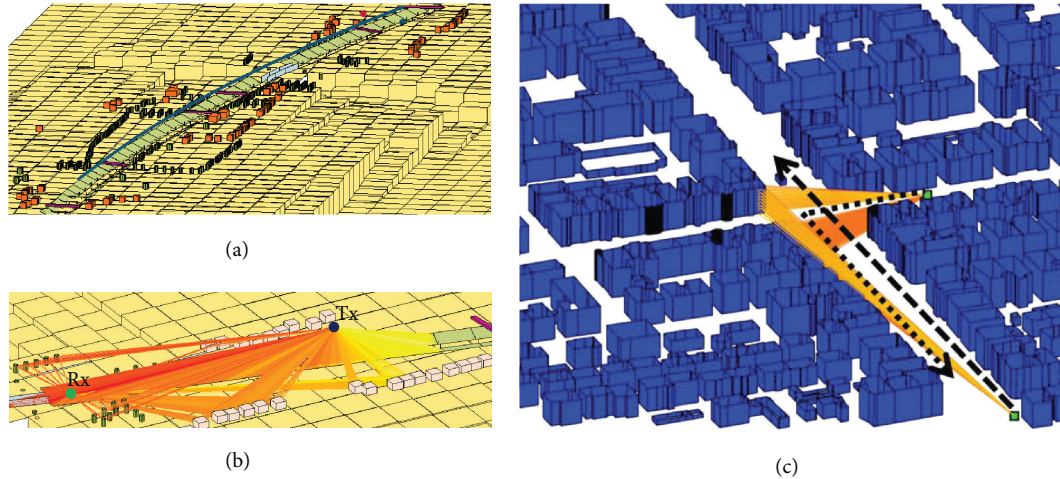


FIGURE 5: Example of (a) a ray-tracing map of the realistic high-speed railway scenario; (b) partial enlarged drawing for direct, reflected, and scattering paths in one snapshot; (c) and a ray-tracing map of a typical urban V2V channel.

angle of arrival. Based on the wide-sense stationary uncorrelated scattering (WSSUS) assumption [59], the tapped delay line model is developed and widespread used for cellular system simulations. This approach describes the CIR by means of a finite impulse response filter with a number of discrete taps, each of which is fading according to a prescribed probability density function and Doppler spectrum. In particular, the IEEE 802.11 p channel models employ the 6-tap and 12-tap models developed by Ingram and coworkers [60, 61] in different types of environments. Since each tap contains multiple paths and each path can have a different type of Doppler spectrum, almost arbitrary Doppler spectra can be synthesized for each tap. Due to the low complexity of the implementation, tapped delay line models are widely used, even though they may suffer from less accurate representation of the nonstationarity in WSV2X channels.

5.3. Geometry-Based Stochastic Models. Geometry-based stochastic modeling (GSCM) is similar to the stochastic modeling, but it uses a simplified ray tracing along with random scatterers. The GSCM is widely used in MIMO channel modeling [38]. Generally, the GSCM models can be divided into the regular-shaped GSCMs (RS-GSCMs) and irregular shaped GSCMs (IS-GSCMs) [62]. It depends on whether the effective scatterers distribute on a regular shape (one-ring, two-ring, and ellipses) or an irregular shape determined by the environment. RS-GSCMs are mathematically tractable and used for theoretical analysis. However, the IS-GSCM can easily handle the nonstationarity of WSV2X channel. Both the RS-GSCM and IS-GSCM models have been researched in the V2X channel and the T2I channel. Figure 6 gives sketches of the geometry-based stochastic model of T2I channel [36] in the cutting scenario and V2V channel [26] with scatterers in realistic positions.

5.4. Summary and Selecting a Suitable Modeling Approach. Each of the modeling methods offered above has specific advantages and disadvantages.

- (i) Deterministic channel models offer the most accurate simulation of the realistic channel model including the nonstationarity of the channel naturally. However, they require highly accurate topographical databases and are numerically intensive to process. Moreover, the high resolution digital elevation model (DEM) for the ray-tracing method is very expensive, and this limits the application of the deterministic models.
- (ii) Stochastic channel models, particularly the tapped delay line models, can be parameterized in a relatively flexible way to describe channels in different scenarios. However, the implementations of the tapped delay line models, especially in the IEEE 802.11 p channel models, do not consider the nonstationarity of the channel. This is the main drawback of the application of such kind of modeling method to the WSV2X channel and, therefore, more and more researchers, such as the authors in [63], are making efforts to introduce the nonstationarity to the stochastic channel models.
- (iii) Geometry-based stochastic models can reflect the realistic behavior of the WSV2X channel and implicitly describe the nonstationarity of the channel. They require more computation time than stochastic channel models to realize a CIR but normally are still much easier than the deterministic models.

Hence, it is hard to say which modeling method is the most outstanding. The choice always strongly depends on the concrete requirements of the application and the development of each method. For instance, the stochastic modeling methods can be a very simple and promising choice to realize the channel if the channel does not change fast or the nonstationarity can be successfully involved in the implementation. The deterministic modeling method can be more proper if the network planning or the system level simulation has a very high accurate requirement, and more effective acceleration techniques, such as the parallel processing and

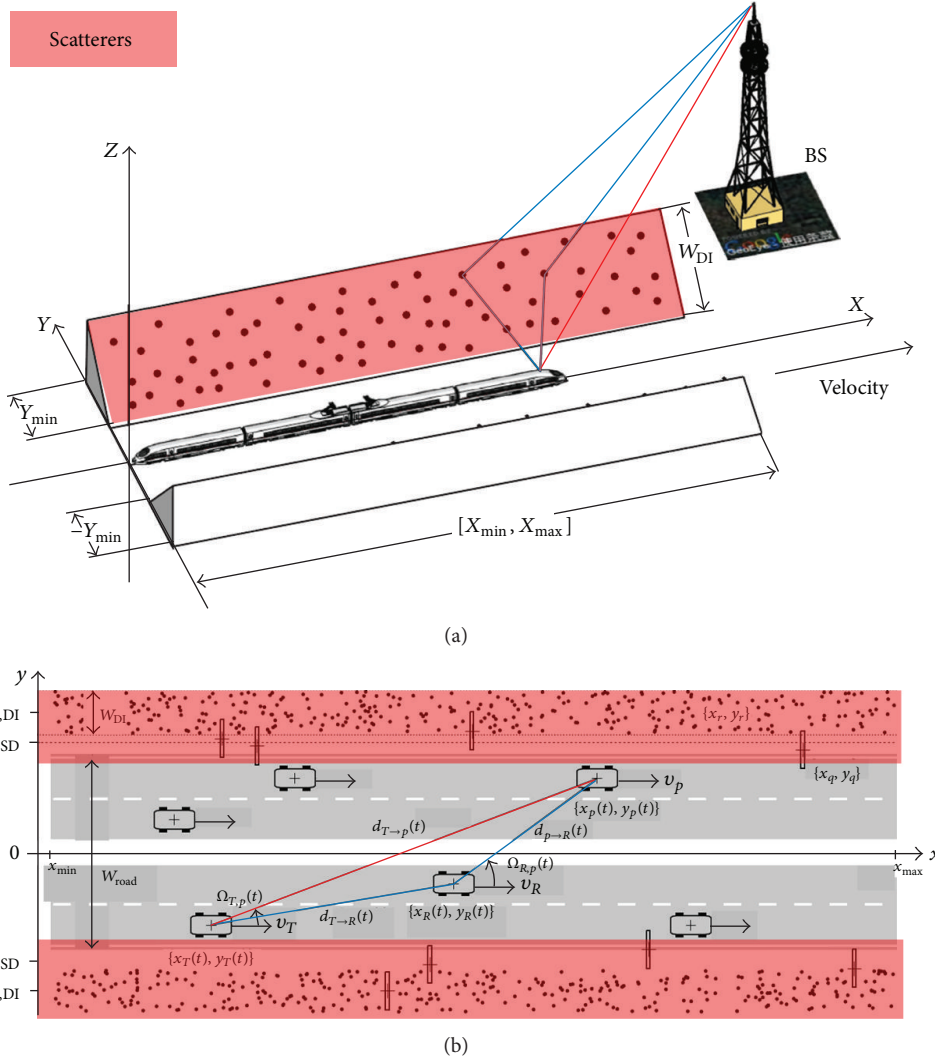


FIGURE 6: (a) Sketch of the geometry-based stochastic model of T2I channels in the cutting scenario with scatterers in realistic positions [36]. (b) Sketch of the geometry-based stochastic model of V2V channels [26].

backface culling [64], are implemented. According to the current level, the geometry-based stochastic model can be treated as a middle course of the other two kinds of modeling methods in the simulation, but it cannot be used for the network planning or the site-specific simulation.

6. Conclusion

Traditional concepts of V2X and T2X are summarized together to constitute a more general concept—wide-sense V2X (WSV2X). This paper offers an overview of the development of the WSV2X channels, such as the standardization, scenarios, characters, and modeling approaches. This paper integrates the common senses of V2X, T2X, and standard scenarios and forms a new panorama of the scenarios classified by the similar physical characters and propagation mechanisms. This effort is made to give some rough inspirations of the joint research of the V2X and T2X scenarios. Following this thought, it is expected to interpret and model the WSV2X channels in a uniform way. As a result,

the channel characterization, network planning, and system design of WSV2X communication systems can be realized by using the same methodology and philosophy. However, besides these results, the answers of more open questions are still missing. For instance, the developments of the V2X and T2X channels are not balanced, how can we compensate the corresponding research in T2X channels to fulfill a panorama of the WSV2X channel? How can we describe the nonstationarity of the WSV2X channel in an easy way? How can we break the limitations of each modeling approaches or develop some hybrid models integrating the advantages of various modeling methods? So many open questions, combined with the increasing importance of WSV2X communications, will surely make the WSV2X channels an exciting and promising research field in the next years.

Acknowledgments

The authors express their thanks to the support from the NNSF of China under Grant U1334202; NNSF of China

under Grant 61222105; Beijing Municipal NSF under Grant 4112048; the Key Grant Project of Chinese Ministry of Education (no. 313006); Project of State Key Lab under Grants RCS2012ZT013, RCS2011K008, and RCS2011ZZ008; and Key Project for Railway Ministry of China under Grant 2012X008-A.

References

- [1] T. Vaa, M. Penttinen, and I. Spyropoulou, "Intelligent transport systems and effects on road traffic accidents: state of the art," *IET Intelligent Transport Systems*, vol. 1, no. 2, pp. 81–88, 2007.
- [2] IEEE Std. 802. 11-2007, "Part 11: wireless LAN medium access control (MAC) and physical layer (PHY) specifications," IEEE Std. 802. 11, 2007.
- [3] ETSI ES 202 663, "Intelligent transport systems, european profile standard on the physical and medium access layer of 5 GHz ITS," Draft Version 0. 0. 6, October 2009.
- [4] U. S. Federal Communications Commission, "Report and order," Tech. Rep. FCC 03-324, 2003.
- [5] IEEE Std 1609. 4, "IEEE standard for wireless access in vehicular environments (WAVE)-multi-channel operation," February 2011.
- [6] "IEEE standard for communications-based train control (CBTC) performance and functional requirements," December 1999.
- [7] <http://www.uic.asso.fr>.
- [8] ETSI ETR 300-3 (2000-02), "Terrestrial trunked radio (TETRA), voice plus data (V+D), designers' guide, part 3: Direct Mode Operation (DMO)," 1st edition, 2000.
- [9] H. Zhou and B. Luo, "Design and budget analysis of RF receiver of 5.8 GHz ETC reader," in *Proceedings of the International Conference on Communication Technology (ICCT '10)*, pp. 354–357, Nanjing, China, November 2010.
- [10] ERTMS/ETCS—Class 1, FFFIS for Eurobalise. Subset-026, Issue 2. 4. 1. September 2007.
- [11] C. R. García, A. Lehner, T. Strang, and K. Frank, "Channel model for train to train communication using the 400 MHz band," in *Proceedings of the 2008 IEEE 67th Vehicular Technology Conference*, pp. 3082–3086, Singapore, May 2008.
- [12] *1st Year Research Report on Railroad Wireless Communication System*, Korea Railroad Research Institute, Seoul, Republic of Korea, 2011.
- [13] K. Guan, Z. Zhong, and B. Ai, "Assessment of LTE-R using high speed railway channel model," in *Proceedings of the 3rd International Conference on Communications and Mobile Computing*, pp. 461–464, Qingdao, China, 2011.
- [14] P. Tiberg, *GSM-Railway, Yesterday, Today and Tomorrow*, Nokia Siemens Networks, Banebranchen, Copenhagen, Denmark, 2009.
- [15] <http://www.uic.org>.
- [16] R. Y. Kim, J. S. Kwak, and H. C. Hwang, "Technical challenges of railroad communications using long term evolution," in *Proceedings of the IEEE International Conference on ICT Convergence (ICTC '12)*, pp. 1–2, Jeju, Republic of Korea, 2012.
- [17] M. Aguado, I. Liedo Samper, M. Berbineau, and E. Jacob, "4G communication technologies for train to ground communication services: LTE versus WIMAX, a simulation study," in *Proceedings of the 9th World Congress on Railway Research*, pp. 1–10, Lille, France, 2011.
- [18] T. Gao and B. Sun, "A high-speed railway mobile communication system based on LTE," in *Proceedings of the International Conference on Electronics and Information Engineering (ICEIE '10)*, pp. 414–417, Kyoto, Japan, August 2010.
- [19] J. Zhang, Z. Tan, Z. Zhong, and Y. Kong, "A multi-mode multi-band and multi-system-based access architecture for high-speed railways," in *Proceedings of the IEEE 72nd Vehicular Technology Conference Fall (VTC '10)*, pp. 1–5, Ottawa, Canada, September 2010.
- [20] UIC, *GSM-R Procurement Guide*, Union Internationale des Chemins de Fer, Paris, France, 2007.
- [21] O. Andre, *LTE and Its Applications in Railways, Networks and the New Economy*, Alcatel-Lucent, Cambridge, UK, 2010.
- [22] "Huawei eyes European market," September 2011, <http://www.railwaygazette.com/news/business/single-view/view/huawei-eyes-european-market.html>.
- [23] A. F. Molisch, F. Tufvesson, J. Karedal, and C. F. Mecklenbräuker, "A survey on vehicle-to-vehicle propagation channels," *IEEE Wireless Communications*, vol. 16, no. 6, pp. 12–22, 2009.
- [24] B. Ai, R. He, Z. Zhong et al., "Radio wave propagation scene partitioning for high-speed rails," *International Journal on Antennas and Propagation*, vol. 2012, Article ID 815332, 7 pages, 2012.
- [25] L. Cheng, B. E. Henty, D. D. Stancil, F. Bai, and P. Mudalige, "Mobile vehicle-to-vehicle narrow-band channel measurement and characterization of the 5.9 GHz dedicated short range communication (DSRC) frequency band," *IEEE Journal on Selected Areas in Communications*, vol. 25, no. 8, pp. 1501–1516, 2007.
- [26] J. Karedal, F. Tufvesson, N. Czink et al., "A geometry-based stochastic MIMO model for vehicle-to-vehicle communications," *IEEE Transactions on Wireless Communications*, vol. 8, no. 7, pp. 3646–3657, 2009.
- [27] K. Guan, Z. Zhong, B. Ai, and C. Briso, "Propagation mechanism analysis before the break point inside tunnels," in *Proceedings of the IEEE 74th Vehicular Technology Conference*, pp. 1–5, San Francisco, Calif, USA, 2011.
- [28] K. Guan, Z. Zhong, B. Ai, and C. Briso-Rodríguez, "Propagation mechanism modelling in the near region of circular tunnels," *IET Microwaves, Antennas and Propagation*, vol. 6, no. 3, pp. 355–360, 2012.
- [29] K. Guan, Z. Zhong, B. Ai, and C. Briso-Rodríguez, "Modeling of the division point of different propagation mechanisms in the near-region within arched tunnels," *Wireless Personal Communications*, vol. 68, no. 3, pp. 489–505, 2013.
- [30] K. Guan, Z. Zhong, B. Ai, R. He, Y. Li, and C. Briso, "Propagation mechanism modeling in the near-region of arbitrary cross-sectional tunnels," *International Journal of Antennas and Propagation*, vol. 2012, Article ID 183145, 11 pages, 2012.
- [31] K. Guan, Z. Zhong, B. Ai, and C. Briso-Rodríguez, "Research of propagation characteristics of break point; Near zone and far zone under operational subway condition," in *Proceedings of the 6th International Wireless Communications and Mobile Computing Conference (IWCMC '10)*, pp. 114–118, Caen, France, July 2010.
- [32] K. Guan, Z. Zhong, B. Ai, and C. Briso-Rodríguez, "Measurement and modeling of subway near shadowing phenomenon," in *Proceedings of the 5th International ICST Conference on Communications and Networking in China (ChinaCom '10)*, pp. 1–5, Beijing, China, August 2010.

- [33] K. Guan, Z. Zhong, B. Ai, and C. Briso, "Novel hybrid propagation model inside tunnels," in *Proceedings of the IEEE 75th Vehicular Technology Conference*, pp. 1–5, Yokohama, Japan, 2012.
- [34] K. Guan, Z. Zhong, B. Ai et al., "Complete propagation model structure inside tunnels," *Progress in Electromagnetics Research*, vol. 141, pp. 711–726, 2013.
- [35] K. Guan, Z. Zhong, B. Ai, R. He, and C. Briso-Rodriguez, "Five-zone propagation model for large-size vehicles inside tunnels," *Progress in Electromagnetics Research*, vol. 138, pp. 389–405, 2013.
- [36] B. Chen and Z. Zhong, "Geometry-based stochastic modeling for MIMO channel in high-speed mobile scenario," *International Journal of Antennas and Propagation*, vol. 2012, Article ID 184682, 6 pages, 2012.
- [37] K. Guan, Z. D. Zhong, B. Ai, and T. Kuerner, "Semi-deterministic propagation modeling for high-speed railway," *IEEE Antennas and Wireless Propagation Letters*, vol. 12, pp. 789–792, 2013.
- [38] P. Almers, E. Bonek, A. Burr et al., "Survey of channel and radio propagation models for wireless MIMO systems," *Eurasip Journal on Wireless Communications and Networking*, vol. 2007, Article ID 19070, 2007.
- [39] T. Abbas, J. Karedal, F. Tufvesson, A. Paier, L. Bernadó, and A. F. Molisch, "Directional analysis of vehicle-to-vehicle propagation channels," in *Proceedings of the IEEE 73rd Vehicular Technology Conference (VTC '11)*, pp. 1–5, Budapest, Hungary, May 2011.
- [40] J. Nuckelt, T. Abbas, F. Tufvesson, C. Mecklenbräuker, L. Bernadó, and T. Kürner, "Comparison of ray tracing and channel-sounder measurements for vehicular communications," in *Proceedings of the IEEE 77th Vehicular Technology Conference (VTC '13)*, pp. 1–5, Dresden, Germany, June 2013.
- [41] L. Liu, C. Tao, J. Qiu et al., "Position-based modeling for wireless channel on high-speed railway under a viaduct at 2.35 GHz," *IEEE Journal on Selected Areas in Communications*, vol. 30, no. 4, pp. 834–845, 2012.
- [42] B. Chen, Z. Zhong, and B. Ai, "Stationarity intervals of time-variant channel in high speed railway scenario," *China Communications*, vol. 9, pp. 64–70, 2012.
- [43] H. Wei, Z. Zhong, K. Guan, and B. Ai, "Path loss models in viaduct and plain scenarios of the high-speed railway," in *Proceedings of the 5th International ICST Conference on Communications and Networking in China (ChinaCom '10)*, pp. 1–5, Beijing, China, August 2010.
- [44] K. Guan, Z. Zhong, J. I. Alonso, and C. Briso-Rodríguez, "Measurement of distributed antenna systems at 2.4 GHz in a realistic subway tunnel environment," *IEEE Transactions on Vehicular Technology*, vol. 61, no. 2, pp. 834–837, 2012.
- [45] Y. Guo, J. Zhang, C. Tao, L. I. U. Liu, and L. Tian, "Propagation characteristics of wideband high-speed railway channel in viaduct scenario at 2.35 GHz," *Journal of Modern Transportation*, vol. 20, no. 4, pp. 206–212, 2012.
- [46] G. Acosta-Marum and M. A. Ingram, "Six time- and frequency-selective empirical channel models for vehicular wireless LANs," *IEEE Vehicular Technology Magazine*, vol. 2, no. 4, pp. 4–11, 2007.
- [47] IST WINNER II D1.1.2, "WINNER II channel models," <http://www.ist-winner.org/WINNER2-Deliverables/D1.1.2v1.1.pdf>.
- [48] J. Maurer, T. Fügen, and W. Wiesbeck, "Narrow-band measurement and analysis of the inter-vehicle transmission channel at 5.2 GHz," in *Proceedings of the IEEE 55th Vehicular Technology Conference (VTC '02)*, pp. 1274–1278, Birmingham, UK, May 2002.
- [49] J. Maurer, T. M. Schäfer, and W. Wiesbeck, "A realistic description of the environment for inter-vehicle wave propagation modelling," in *Proceedings of the IEEE 54th Vehicular Technology Conference (VTC '01)*, pp. 1437–1441, Atlantic, NJ, USA, October 2001.
- [50] J. Maurer, T. Fügen, T. Schäfer, and W. Wiesbeck, "A new inter-vehicle communications (IVC) channel model," in *Proceedings of the IEEE 60th Vehicular Technology Conference (VTC '04)*, pp. 9–13, Los Angeles, Calif, USA, September 2004.
- [51] J. W. McKown and R. L. Hamilton Jr., "Ray tracing as a design tool for radio networks," *IEEE Network*, vol. 5, no. 6, pp. 27–30, 1991.
- [52] A. Maltsev, R. Maslennikov, A. Lomayev, A. Sevastyanov, and A. Khoryaev, "IEEE 802.11-09/0431r0," April 2009.
- [53] J. Nuckelt, M. Schack, and T. Kürner, "Deterministic and stochastic channel models implemented in a physical layer simulator for Car-to-X communications," *Advances in Radio Science*, vol. 9, pp. 165–171, 2011.
- [54] K. Guan, Z. Zhong, B. Ai, and T. Kurner, "Deterministic propagation modeling for the realistic high-speed railway environment," in *Proceedings of the IEEE 77th Vehicular Technology Conference (VTC '13)*, pp. 1–5, Dresden, Germany, 2013.
- [55] W. C. Jakes, Ed., *Microwave Mobile Communications*, Wiley, New York, NY, USA, 1974.
- [56] A. S. Akki and F. Haber, "A statistical model of mobile-to-mobile land communication channel," *IEEE Transactions on Vehicular Technology*, vol. 35, no. 1, pp. 2–7, 1986.
- [57] A. S. Akki, "Statistical properties of mobile-to-mobile land communication channels," *IEEE Transactions on Vehicular Technology*, vol. 43, no. 4, pp. 826–831, 1994.
- [58] F. Vatalaro, "Doppler spectrum in mobile-to-mobile communications in the presence of three-dimensional multipath scattering," *IEEE Transactions on Vehicular Technology*, vol. 46, no. 1, pp. 213–219, 1997.
- [59] P. A. Bello, "Characterization of randomly time-variant linear channels," *IEEE Transactions on Communications*, vol. 11, pp. 360–393, 1963.
- [60] G. Acosta and M. A. Ingram, "Model development for the wide-band expressway vehicle-to-vehicle 2.4 GHz channel," in *Proceedings of the IEEE Wireless Communications and Networking Conference (WCNC '06)*, pp. 1283–1288, Las Vegas, Nev, USA, April 2006.
- [61] G. Acosta-Marum and M. A. Ingram, "Six time- and frequency-selective empirical channel models for vehicular wireless LANs," *IEEE Vehicular Technology Magazine*, vol. 2, no. 4, pp. 4–11, 2007.
- [62] C. Wang, X. Cheng, and D. Laurenson, "Vehicle-to-vehicle channel modeling and measurements: recent advances and future challenges," *IEEE Communications Magazine*, vol. 47, no. 11, pp. 96–103, 2009.
- [63] A. Chelli and M. Pätzold, "A non-stationary MIMO vehicle-to-vehicle channel model derived from the geometrical street model," in *Proceedings of the IEEE 74th Vehicular Technology Conference (VTC '11)*, pp. 1–6, San Francisco, Calif, USA, September 2011.
- [64] T. Kürner and M. Schack, "3D ray-tracing embedded into an integrated simulator for car-to-X communications," in *Proceedings of the 20th URSI International Symposium on Electromagnetic Theory (EMTS '10)*, pp. 880–882, Berlin, Germany, August 2010.

Research Article

Improved Pilot-Aided Channel Estimation for MIMO-OFDM Fading Channels

J. Mar,^{1,2} Chi-Cheng Kuo,¹ and M. B. Basnet¹

¹ Department of Communications Engineering, Yuan-Ze University, 135 Yuan-Tung Road, Jungli, Taoyuan 320, Taiwan

² Communications Research Center, Yuan-Ze University, 135 Yuan-Tung Road, Jungli, Taoyuan 320, Taiwan

Correspondence should be addressed to J. Mar; eejmar@saturn.yzu.edu.tw

Received 2 July 2013; Accepted 11 August 2013

Academic Editor: Ai Bo

Copyright © 2013 J. Mar et al. This is an open access article distributed under the Creative Commons Attribution License, which permits unrestricted use, distribution, and reproduction in any medium, provided the original work is properly cited.

An improved pilot-aided channel estimation scheme is proposed to enhance the channel estimation accuracy of multiple-input multiple-output-orthogonal frequency division multiplexing (MIMO-OFDM) fading channels. Based on the adaptive path number selection mechanism, the number of paths can be scalable and adaptively changed with the characteristics of MIMO-OFDM fading channels. The fine channel estimation formulas for all data subcarriers are derived. The 2×2 space-frequency block code-OFDM (SFBC-OFDM) system and a six-path fading channel model are considered as an example of the high mobility MIMO-OFDM wireless communications system. Through simulations it is shown that 2×2 SFBC-OFDM system using the proposed approach can satisfy the performance requirements over frequency selective and frequency nonselective fast fading channels.

1. Introduction

The cellular mobile communications industry has recently been one of the fastest growing industries of all time, with the number of users increasing incredibly rapidly. Orthogonal frequency division multiplexing access (OFDMA) was chosen as the spectrum access technology of the 4G cellular systems because its orthogonality eliminates intracell interference. The high mobility OFDM wireless communication system will operate in a fast fading channel, where the nonnegligible fluctuations of the channel gains are expected within each OFDM data block. Fast fading involves variations on the scale of a half-wavelength and frequently introduces variations as large as 35–40 dB [1]. The channel estimation in OFDM systems over time-varying fading channels is generally based on the use of pilot subcarriers in given positions of the frequency-time grid [2]. It is advisable to place pilot subcarriers in each OFDM data block in order to ensure adequate estimation accuracy. In [3], the effect of pilot power on the performance of 16-QAM OFDM system operating in two-ray Rayleigh slow fading channel is presented. The optimum pilot-to-data power ratio (PDR) is analytically derived. As an alternative, the channel estimation algorithm based on subspace tracking has been presented in

[4] for OFDM systems, which can effectively reduce channel estimation error by tracking the dominant delay-subspace spanned by the frequency responses.

Increasing demand for high performance 4G broadband wireless is enabled by the use of multiple antennas at both base station and user equipment ends. Multiple-input-multiple-output (MIMO) is one of the best ways to combat channel fading using transmit diversity and receive diversity. The use of MIMO technique in OFDM system is an efficient solution to meet the growing demand for high speed, spectral efficiency, and reliable communication [2] in future-generation wireless networks. The MIMO-OFDM wireless communications have the inherent signal variability generated from the multipath fading channel. The aim of this study is to investigate the channel estimation algorithm in the MIMO-OFDM fading channels. In [5], it is shown that the space-frequency block code-(SFBC-) OFDM system exhibits error floors caused by imperfect channel state estimation over frequency selective fading channels. Hence, we need a more robust frequency and phase synchronization technology for fast MIMO-OFDM fading channels. The optimum pilot allocation in terms of overhead and channel estimation error is analyzed in reference [6] that maximizes the channel

capacity for MIMO-OFDM system operating in frequency selective fading channel. Both perfect interpolation and non-perfect interpolation for pilot-aided channel estimations are considered. In [7], the sequential decision feedback sequence estimation with an adaptive threshold equalizer technique and pilot tone plus interpolation channel estimation scheme are used to design the Alamouti coded small constellation (BPSK and QPSK) OFDM receiver in fast fading channels.

An adaptive path number selection mechanism is proposed for channel estimation over MIMO-OFDM fading channels to provide the suboptimum system performance, whenever the high order modulation MIMO-OFDM system is operated either in frequency nonselective fast fading or in frequency selective fast fading channels. The 2×2 SFBC-OFDM system and a six-path fading channel model are considered as an example of the MIMO-OFDM system in the simulations to prove that the acceptable bit error rate (BER) can be achieved by employing 16-QAM and 64-QAM modulations in time-varying fast fading channels. We consider the vehicle speed of 200 km/h, resulting in the Doppler frequency of 1093 Hz to satisfy the fast fading condition for MIMO-OFDM channel [8, 9].

The rest of this paper is organized as follows. The proposed MIMO-OFDM channel estimation algorithm is described in Section 2, where the fine channel estimation for all data subcarriers is derived. The adaptive path number selection mechanism for the MIMO-OFDM fading channel is presented in Section 3. The BER performance of the MIMO-OFDM system using the proposed suboptimal channel estimation approach is simulated and discussed in Section 4. Finally, concluding remarks are given in Section 5.

2. MIMO-OFDM Channel Estimation

We consider a generic downlink multiuser MIMO-OFDM channel model. Let the number of transmit antennas be n_T and the number of receive antennas n_R . One OFDM symbol of each user is transmitted across N subcarriers. To simplify the formula derivations, the data vector \mathbf{X} for each user can be expressed in polyphase representation as

$$\mathbf{X} = [X_0 \ X_1 \ \cdots \ X_{N-2} \ X_{N-1}]^T, \quad (1)$$

where T denotes the transpose of the vector. Thus, the demodulated signal vector is given by

$$\mathbf{Y} = \mathbf{H}\mathbf{X} + \mathbf{V}, \quad (2)$$

where \mathbf{H} is a diagonal matrix whose diagonal elements are the N -DFT of the channel impulse response \mathbf{h} and \mathbf{V} is the N -DFT of the channel noise. With reference to the conventional channel estimation approach of a given OFDM system [9], ten short OFDM training signals are used for packet detection, coarse frequency offset estimation, and timing synchronization. Two periods of the long training signals are used for improving channel estimation accuracy of the short training symbols. A phase-locked loop is adopted in the receiver for estimating and compensating the carrier frequency offset. Each OFDM data block contains L pilot subcarriers, which are used to track the carrier phase.

A typical 2×2 SFBC-OFDM model, which consists of two transmit antennas and two receive antennas, is used to describe the theoretical analysis and the proposed channel estimation scheme. User data vector \mathbf{X} is first encoded into two spatial vectors \mathbf{X}_1 and \mathbf{X}_2 by the space-frequency encoder. Denote the transmitted signal vector of each user in a space-frequency block as

$$\begin{aligned} \mathbf{X}_1 &= [X_0 \ -X_1^* \ \cdots \ X_{N-2} \ -X_{N-1}^*]^T, \\ \mathbf{X}_2 &= [X_1 \ X_0^* \ \cdots \ X_{N-1} \ X_{N-2}^*]^T, \end{aligned} \quad (3)$$

where \mathbf{X}_1 is the data transmitted from the first antenna Tx_1 and \mathbf{X}_2 is the data transmitted from the second antenna Tx_2 , simultaneously. Let \mathbf{X}_e and \mathbf{X}_o be even and odd component vectors of \mathbf{X} ; that is,

$$\begin{aligned} \mathbf{X}_e &= [X_0 \ X_2 \ \cdots \ X_{N-4} \ X_{N-2}]^T, \\ \mathbf{X}_o &= [X_1 \ X_3 \ \cdots \ X_{N-3} \ X_{N-1}]^T. \end{aligned} \quad (4)$$

Similarly, $\mathbf{X}_{1,e}$, $\mathbf{X}_{1,o}$, $\mathbf{X}_{2,e}$, and $\mathbf{X}_{2,o}$ denote even and odd component vectors of \mathbf{X}_1 and \mathbf{X}_2 , respectively, which can then be expressed in terms of even and odd component vectors as

$$\begin{aligned} \mathbf{X}_{1,e} &= \mathbf{X}_e, & \mathbf{X}_{1,o} &= -\mathbf{X}_o^*, \\ \mathbf{X}_{2,e} &= \mathbf{X}_o, & \mathbf{X}_{2,o} &= \mathbf{X}_e^*. \end{aligned} \quad (5)$$

Note that since the two corresponding signals transmitted from two antennas at the same time slots are orthogonal, the maximum likelihood decoding is reduced to simple linear processing at the receiver. The received signal at the receiver is given by

$$\begin{aligned} \mathbf{Y}_1 &= \mathbf{H}_{1,1}\mathbf{X}_1 + \mathbf{H}_{2,1}\mathbf{X}_2 + \mathbf{V}_1, \\ \mathbf{Y}_2 &= \mathbf{H}_{1,2}\mathbf{X}_1 + \mathbf{H}_{2,2}\mathbf{X}_2 + \mathbf{V}_2, \end{aligned} \quad (6)$$

where \mathbf{Y}_1 and \mathbf{Y}_2 are the received signals in the first and second received antenna, $\mathbf{H}_{1,1}$ and $\mathbf{H}_{2,1}$ are the channel frequency response of the first and second antenna transmitted to the first received antenna, and $\mathbf{H}_{1,2}$ and $\mathbf{H}_{2,2}$ are the channel frequency response of the first and second antenna transmitted to the second received antenna. The channel frequency response at all data subcarriers for each transmit-receive antenna pair is defined as

$$\mathbf{H}_{p,q} = \begin{bmatrix} H_{p,q,0} & 0 & \cdots & 0 \\ 0 & H_{p,q,1} & \cdots & 0 \\ \cdots & \cdots & \cdots & \cdots \\ 0 & 0 & \cdots & H_{p,q,N-1} \end{bmatrix} \quad (7)$$

for $\begin{cases} p = 1, \dots, n_T \\ q = 1, \dots, n_R \end{cases}$.

Equivalently, (6) can be represented as

$$\begin{aligned} \mathbf{Y}_{1,e} &= \mathbf{H}_{1,1,e}\mathbf{X}_{1,e} + \mathbf{H}_{2,1,e}\mathbf{X}_{2,e} + \mathbf{V}_{1,e}, \\ \mathbf{Y}_{1,o} &= \mathbf{H}_{1,1,o}\mathbf{X}_{1,o} + \mathbf{H}_{2,1,o}\mathbf{X}_{2,o} + \mathbf{V}_{1,o}, \\ \mathbf{Y}_{2,e} &= \mathbf{H}_{1,2,e}\mathbf{X}_{1,e} + \mathbf{H}_{2,2,e}\mathbf{X}_{2,e} + \mathbf{V}_{2,e}, \\ \mathbf{Y}_{2,o} &= \mathbf{H}_{1,2,o}\mathbf{X}_{1,o} + \mathbf{H}_{2,2,o}\mathbf{X}_{2,o} + \mathbf{V}_{2,o}. \end{aligned} \quad (8)$$

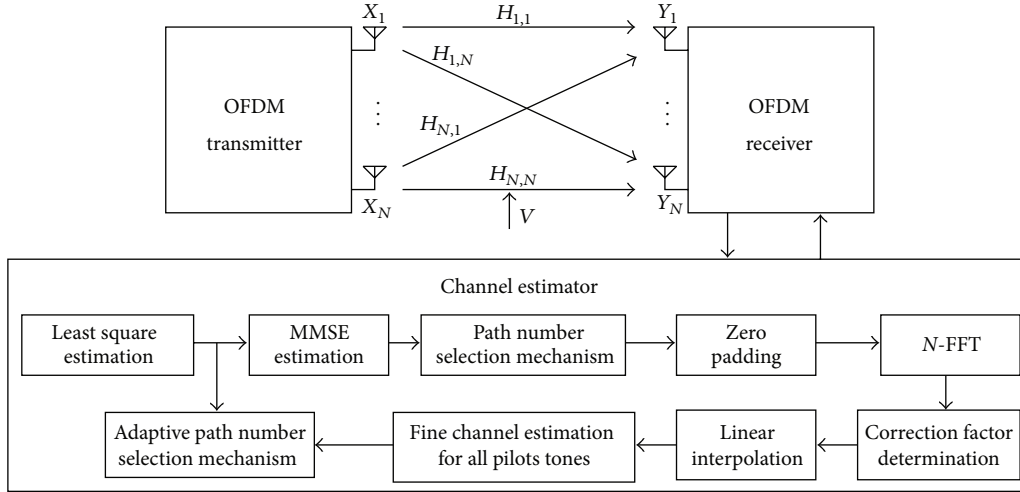


FIGURE 1: Block diagram of pilot tone channel estimation aided with adaptive path number selection mechanism for MIMO-OFDM fading channel.

The received signal at the q th receive antenna for the k th pilot tone transmitted from p th antenna can be written as

$$\begin{aligned} Y_{q,k} &= X_{p,k}H_{p,q,k} + V_{q,k}, \quad k = 0, 1, \dots, N-1, \\ p &= 1, \dots, n_T, \\ q &= 1, \dots, n_R, \end{aligned} \quad (9)$$

where N is the frequency tones in each OFDM data block, $X_{p,k}$ is the transmitted signal of p th transmitted antenna, $H_{p,q,k}$ is the channel frequency response from p th transmit antenna to q th receive antenna, and $V_{q,k}$ is the AWGN noise.

Then from (9), the channel estimation at pilot subcarriers based on the least square (LS) algorithm can be obtained as

$$\widehat{H}_{p,q,k} = \frac{Y_{q,k}}{X_{p,k}} = H_{p,q,k} + \frac{S_{q,k}}{\sqrt{\varepsilon_x}}, \quad k = 0, 1, \dots, N-1, \quad (10)$$

where $S_{q,k} = V_{q,k}/e^{j\angle X_{p,k}}$, $|X_{p,k}| = \sqrt{\varepsilon_x}$, and $X_{p,k} = |X_{p,k}|e^{j\angle X_{p,k}}$. Let $\{k_1, k_2, \dots, k_L\}$ be the set of L pilot tones, which is one of the sets $\{i, i + N/L, \dots, i + (L-1)N/L\}$, $i = 0, 1, \dots, N/L-1$, used for transmitting the training data. Collect these channel responses in a vector $\widehat{\mathbf{H}}_{p,q,k_p} = [\widehat{H}_{p,q,k_1}, \dots, \widehat{H}_{p,q,k_L}]^T$, which is obtained from the FFT matrix.

The intermediate processing steps between the LS estimates of the channel gains over the pilot subcarriers and interpolation processing are added in order to ensure adequate estimation accuracy for fast fading channel. The block diagram of the proposed pilot tone channel estimation aided with adaptive path number selection mechanism is shown in Figure 1. Here ℓ is defined as the number of dominant paths estimated from the adaptive channel path number selector, which chooses ℓ paths with larger power from $(\widehat{\mathbf{h}}_{p,q,k_p})_{\ell \times 1}$, and let $\{b_1, b_2, \dots, b_\ell\}$ be a set of the selected pilot index. Since

AWGN assumption for each subcarrier is adopted, and since each pilot tone carries data of constant modulus $\sqrt{\varepsilon_x}$, the minimum mean square error (MMSE) estimation of $\mathbf{h}_{p,q}$ is given by [10]

$$\begin{aligned} \widehat{\mathbf{h}}_{p,q,k_p} &= \mathbf{Q}_{p,q,k_p}^{-1} \widehat{\mathbf{H}}_{p,q,k_p} \\ &= \mathbf{h}_{p,q,k_p} + \mathbf{Q}_{p,q,k_p}^{-1} \frac{1}{\sqrt{\varepsilon_x}} \mathbf{S}_{k_p}, \end{aligned} \quad (11)$$

where $\mathbf{S}_{q,k_p} = [S_{q,k_1}, \dots, S_{q,k_L}]^T$, $(\widehat{\mathbf{h}}_{p,q,k_p})_{\ell \times 1} = [\widehat{h}_{p,q,k_1}, \widehat{h}_{p,q,k_2}, \dots, \widehat{h}_{p,q,k_\ell}]^T$, and \mathbf{Q}_{p,q,k_p} is a Vandermonde matrix with distinct L twiddle factor $W_N^{k_i}$:

$$\begin{aligned} & \left((\mathbf{Q}_{p,q,k_p})_{\ell \times L} \right)^{-1} \\ &= \begin{bmatrix} (\mathbf{Q}_{p,q,k_p})^{-1}(b_1, 1) & (\mathbf{Q}_{p,q,k_p})^{-1}(b_1, 2) & \dots & (\mathbf{Q}_{p,q,k_p})^{-1}(b_1, L) \\ (\mathbf{Q}_{p,q,k_p})^{-1}(b_2, 1) & (\mathbf{Q}_{p,q,k_p})^{-1}(b_2, 2) & \dots & (\mathbf{Q}_{p,q,k_p})^{-1}(b_2, L) \\ \vdots & \vdots & \vdots & \vdots \\ (\mathbf{Q}_{p,q,k_p})^{-1}(b_\ell, 1) & (\mathbf{Q}_{p,q,k_p})^{-1}(b_\ell, 2) & \dots & (\mathbf{Q}_{p,q,k_p})^{-1}(b_\ell, L) \end{bmatrix}. \end{aligned} \quad (12)$$

Other notations are represented as follows: $E\{\cdot\}$ is the expectation operator; $\text{tr}\{\cdot\}$ is the trace operator; $\|\cdot\|$ means 2-norm; \mathbf{I}_L represents the $L \times L$ identity matrix. Therefore, the mean square error (MSE) in the channel estimate can be derived as

$$E \left\{ \left\| (\widehat{\mathbf{h}}_{p,q})_{\ell \times 1} - (\mathbf{h}_{p,q})_{\ell \times 1} \right\|^2 \right\} = \frac{\sigma_s^2}{\varepsilon_x} \text{tr} \left\{ \left(\mathbf{Q}_{p,q,k_p}^* \mathbf{Q}_{p,q,k_p} \right)^{-1} \right\}, \quad (13)$$

where σ_s^2 is the variance of AWGN which is assumed to be known at the receiver, and

$$\begin{aligned} & \left(\mathbf{Q}_{p,q,k_p}^* \mathbf{Q}_{p,q,k_p} \right)_{\ell \times \ell}^{-1} \\ &= \begin{bmatrix} \left(\mathbf{Q}_{p,q,k_p}^* \mathbf{Q}_{p,q,k_p} \right)^{-1} (b_1, b_1) & \cdots & \left(\mathbf{Q}_{p,q,k_p}^* \mathbf{Q}_{p,q,k_p} \right)^{-1} (b_1, b_\ell) \\ \left(\mathbf{Q}_{p,q,k_p}^* \mathbf{Q}_{p,q,k_p} \right)^{-1} (b_2, b_1) & \cdots & \left(\mathbf{Q}_{p,q,k_p}^* \mathbf{Q}_{p,q,k_p} \right)^{-1} (b_2, b_\ell) \\ \vdots & \cdots & \vdots \\ \left(\mathbf{Q}_{p,q,k_p}^* \mathbf{Q}_{p,q,k_p} \right)^{-1} (b_\ell, b_1) & \cdots & \left(\mathbf{Q}_{p,q,k_p}^* \mathbf{Q}_{p,q,k_p} \right)^{-1} (b_\ell, b_\ell) \end{bmatrix}, \end{aligned} \quad (14)$$

where $(\cdot)^*$ denotes the Hermitian transposition and \mathbf{Q}_{p,q,k_p} depends on the choice of the set of pilot tones. Let the eigenvalues of $(\mathbf{Q}_{p,q,k_p}^* \mathbf{Q}_{p,q,k_p})_{\ell \times \ell}^{-1}$ be denoted by $\{\lambda_m, m = 0, 1, \dots, \ell - 1\}$. Then, the eigenvalues of $(\mathbf{Q}_{p,q,k_p}^* \mathbf{Q}_{p,q,k_p})_{\ell \times \ell}$ are $\{1/\lambda_m, m = 0, 1, \dots, \ell - 1\}$. Since the trace of a matrix is the sum of its eigenvalues, then

$$\text{tr} \left\{ \left(\mathbf{Q}_{p,q,k_p}^* \mathbf{Q}_{p,q,k_p} \right)_{\ell \times \ell} \right\} = \sum_{m=0}^{\ell-1} \frac{1}{\lambda_m} = \frac{L}{N} \ell, \quad (15)$$

$$\text{tr} \left\{ \left(\mathbf{Q}_{p,q,k_p}^* \mathbf{Q}_{p,q,k_p} \right)_{\ell \times \ell}^{-1} \right\} = \sum_{m=0}^{\ell-1} \lambda_m = \frac{N}{L} \ell. \quad (16)$$

Substituting (16) into (13) yields the MMSE in channel estimate, when such a pilot tone set is used:

$$E \left\{ \left\| \left(\hat{\mathbf{h}}_{p,q} \right)_{\ell \times 1} - \left(\mathbf{h}_{p,q} \right)_{\ell \times 1} \right\|^2 \right\} = \frac{\sigma_s^2 N \ell}{\varepsilon_x L}. \quad (17)$$

If $\ell = L$, then MMSE is

$$E \left\{ \left\| \hat{\mathbf{h}}_{p,q} - \mathbf{h}_{p,q} \right\|^2 \right\} = \frac{\sigma_s^2 N}{\varepsilon_x}. \quad (18)$$

Equations (17) and (18) show that using less pilot number in the pilot-aided channel estimation can get smaller MSE in the channel impulse response estimate. However, in the frequency selective fast fading channel, less pilot number may cause more linear interpolation loss. The case of $\ell = 1$ will not be considered for path number selection mechanism because it cannot reflect the variation of channel characterization of the frequency selective fading channel. The preliminary channel frequency response estimate $(\tilde{\mathbf{H}}_{p,q})_{N \times 1}$ is obtained by the N -FFT of an $N \times 1$ estimated channel impulse response $(\hat{\mathbf{h}}_{p,q}^\ell)_{N \times 1} = [(\hat{\mathbf{h}}_{p,q}^T)_{\ell \times 1} \mathbf{0}_{(N-\ell) \times 1}^T]^T$. It can be written as

$$\tilde{\mathbf{H}}_{p,q,k}^\ell = \frac{1}{\sqrt{N}} \sum_{n=0}^{\ell-1} \hat{h}_{p,q}^\ell(n) W_N^{kn}, \quad k = 0, 1, \dots, N-1. \quad (19)$$

The preliminary channel frequency response estimates at pilot tones for $k = k_1, k_2, \dots, k_L$ are $\tilde{\mathbf{H}}_{p,q,L \times 1}^\ell = [\tilde{\mathbf{H}}_{p,q,k_1}^\ell, \dots, \tilde{\mathbf{H}}_{p,q,k_L}^\ell]^T$. The correction factor for fine channel frequency response estimate at k_p th pilot tone is defined as

$$C_{p,q,k_p}^\ell = \frac{\hat{H}_{p,q,k_p}^\ell}{\tilde{H}_{p,q,k_p}^\ell} = \frac{(1/\sqrt{N}) \sum_{n=0}^{L-1} \hat{h}_{p,q}^\ell(n) W_N^{k_p n}}{(1/\sqrt{N}) \sum_{n=0}^{\ell-1} \hat{h}_{p,q}^\ell(n) W_N^{k_p n}}. \quad (20)$$

For example, the fine correction factor at k_1 th pilot tone for $L = 4$ and $\ell = 2$ is determined as

$$C_{p,q,k_1}^2 = \frac{\hat{H}_{p,q,k_1}^\ell}{\tilde{H}_{p,q,k_1}^2} = 1 + \frac{\hat{h}_{p,q}(2) W_N^{2k_1} + \hat{h}_{p,q}(3) W_N^{3k_1}}{\hat{h}_{p,q}(0) + \hat{h}_{p,q}(1) W_N^{k_1}}. \quad (21)$$

From (21), it is observed that the fine correction factor can compensate the power loss caused by less path employed in the preliminary channel estimates. When the number of paths chosen is ℓ , the fine correction factor in a vector for L pilot tones is

$$\left(C_{p,q}^\ell \right)_{L \times 1} = \left[C_{p,q,k_1}^\ell, \dots, C_{p,q,k_L}^\ell \right]^T. \quad (22)$$

The fine correction factors for all data subcarriers can be obtained through linear interpolation [11]. Two consecutive fine correction factors in L pilot tones are used to determine the fine correction factors for other data subcarriers that are located between the k_p th and $k_{(p+1)}$ th subcarriers

$$C_{p,q,k_p+u}^\ell = C_{p,q,k_p}^\ell + \left(\frac{C_{p,q,k_{p+1}}^\ell - C_{p,q,k_p}^\ell}{U} \right) \times u, \quad (23)$$

$$p = 1 \sim L-1, \quad u = 1, 2, \dots, U-1.$$

The fine channel estimations for all data subcarriers are

$$\begin{aligned} & \hat{H}_{p,q,k_p+u}^\ell \\ &= C_{p,q,k_p+u}^\ell \times \tilde{H}_{p,q,k_p+u}^\ell \\ &= \left(\frac{\hat{H}_{p,q,k_p}^\ell}{\tilde{H}_{p,q,k_p}^\ell} \right. \\ & \quad \left. + \left(\frac{(\hat{H}_{p,q,k_{p+1}}^\ell / \tilde{H}_{p,q,k_{p+1}}^\ell) - (\hat{H}_{p,q,k_p}^\ell / \tilde{H}_{p,q,k_p}^\ell)}{U} \right) \times u \right) \\ & \quad \times \tilde{H}_{p,q,k_p+u}^\ell, \\ & \quad p = 1 \sim L-1, \quad u = 1, 2, \dots, U-1, \end{aligned} \quad (24)$$

where U is the number of data subcarriers between two adjacent pilot subcarriers. The fine channel estimations at pilot tones are expressed as

$$\hat{H}_{p,q,k_p}^\ell = C_{p,q,k_p}^\ell \times \tilde{H}_{p,q,k_p}^\ell = \hat{H}_{p,q,k_p}^\ell, \quad p = 1 \sim L. \quad (25)$$

The fine channel estimations for those data subcarriers located in the intervals of $(0, k_1)$ and $(k_L, N - 1)$ are determined with the fine correction factors C_{p,q,k_1}^ℓ and C_{p,q,k_L}^ℓ , respectively. Therefore,

$$\begin{aligned}\widehat{H}_{p,q,k_1-b}^\ell &= C_{p,q,k_1-b}^\ell \times \widetilde{H}_{p,q,k_1-b}^\ell \\ &= \frac{\widehat{H}_{p,q,k_1}^\ell}{\widetilde{H}_{p,q,k_1}^\ell} \times \widetilde{H}_{p,q,k_1-b}^\ell, \quad b = 1, 2, \dots, k_1, \\ \widehat{H}_{p,q,k_L+c}^\ell &= C_{p,q,k_L+c}^\ell \times \widetilde{H}_{p,q,k_L+c}^\ell \\ &= \frac{\widehat{H}_{p,q,k_L}^\ell}{\widetilde{H}_{p,q,k_L}^\ell} \times \widetilde{H}_{p,q,k_L+c}^\ell, \quad c = 1, 2, \dots, N - 1 - k_L.\end{aligned}\quad (26)$$

Finally, the fine channel estimate vector is given by

$$\left(\widehat{\mathbf{H}}_{p,q}^\ell\right)_{N \times 1} = \text{diag} \left\{ \widehat{H}_{p,q,0}^\ell, \widehat{H}_{p,q,1}^\ell, \dots, \widehat{H}_{p,q,N-1}^\ell \right\}, \quad (27)$$

where $\widehat{H}_{p,q,k}^\ell$, $k = 0, 1, \dots, N - 1$ are obtained from (24), (25), and (26).

Assume that the channel frequency responses $\widehat{\mathbf{H}}_{p,q}$, for $p = 1, \dots, n_T$ and $q = 1, \dots, n_R$, are known or can be estimated accurately at the receiver, the space-frequency decoder block constructs the even and odd parts of the decision estimate vector $\widehat{\mathbf{X}}$ as

$$\begin{aligned}\widehat{\mathbf{X}}_e &= \widehat{\mathbf{H}}_{1,1,e}^* \mathbf{Y}_{1,e} + \widehat{\mathbf{H}}_{2,1,o}^* \mathbf{Y}_{1,o} + \widehat{\mathbf{H}}_{1,2,e}^* \mathbf{Y}_{2,e} + \widehat{\mathbf{H}}_{2,2,o}^* \mathbf{Y}_{2,o}, \\ \widehat{\mathbf{X}}_o &= \widehat{\mathbf{H}}_{2,1,e}^* \mathbf{Y}_{1,e} - \widehat{\mathbf{H}}_{1,1,o}^* \mathbf{Y}_{1,o} + \widehat{\mathbf{H}}_{2,2,e}^* \mathbf{Y}_{2,e} - \widehat{\mathbf{H}}_{1,2,o}^* \mathbf{Y}_{2,o}.\end{aligned}\quad (28)$$

Substituting (8) into (28) yields

$$\begin{aligned}\widehat{\mathbf{X}}_e &= \left(\left| \widehat{\mathbf{H}}_{1,1,e} \right| + \left| \widehat{\mathbf{H}}_{2,1,e} \right| + \left| \widehat{\mathbf{H}}_{1,2,e} \right| + \left| \widehat{\mathbf{H}}_{2,2,e} \right| \right) \mathbf{X}_e \\ &\quad + \widehat{\mathbf{H}}_{1,1,e}^* \mathbf{V}_{1,e} + \widehat{\mathbf{H}}_{2,1,o}^* \mathbf{V}_{1,o} + \widehat{\mathbf{H}}_{1,2,e}^* \mathbf{V}_{2,e} + \widehat{\mathbf{H}}_{2,2,o}^* \mathbf{V}_{2,o}, \\ \widehat{\mathbf{X}}_o &= \left(\left| \widehat{\mathbf{H}}_{1,1,o} \right| + \left| \widehat{\mathbf{H}}_{2,1,o} \right| + \left| \widehat{\mathbf{H}}_{1,2,o} \right| + \left| \widehat{\mathbf{H}}_{2,2,o} \right| \right) \mathbf{X}_o \\ &\quad + \widehat{\mathbf{H}}_{2,1,e}^* \mathbf{V}_{1,e} - \widehat{\mathbf{H}}_{1,1,o}^* \mathbf{V}_{1,o} + \widehat{\mathbf{H}}_{2,2,e}^* \mathbf{V}_{2,e} - \widehat{\mathbf{H}}_{1,2,o}^* \mathbf{V}_{2,o}.\end{aligned}\quad (29)$$

3. Adaptive Path Number Selection Mechanism

Although MSE in channel frequency response estimate decreases with the path number, under the more serious frequency selective fading channel condition, less selected path number may cause larger error when the interpolation of fine channel frequency response estimation is conducted for all the data subcarriers. Therefore, an adaptive path number selection mechanism is proposed to choose appropriate path number according to the characteristics of time-varying fading channel. The selection procedure of the path number is described as follows. In the first step of the proposed mechanism, the pilot signals in the first OFDM data block

```

Calculations of  $c_{p,q,\ell}$  and  $d_{p,q,\ell}$  for  $\ell = 2, 3, 4$ 
if  $c_{p,q,2} \geq c_{p,q,3}$  &  $c_{p,q,2} \geq c_{p,q,4}$  then
  if  $(d_{p,q,2} \leq d_{p,q,3} \parallel d_{p,q,2} \leq d_{p,q,4})$  then  $\ell = 2$ 
  elseif  $(d_{p,q,3} \leq d_{p,q,2}$  &  $d_{p,q,3} \leq d_{p,q,4})$  then  $\ell = 3$ 
  else
     $\ell = 4$ 
  end
elseif  $c_{p,q,3} \geq c_{p,q,2}$  &  $c_{p,q,3} \geq c_{p,q,4}$  then
  if  $(d_{p,q,3} \leq d_{p,q,2} \parallel d_{p,q,3} \leq d_{p,q,4})$  then  $\ell = 3$ 
  elseif  $(d_{p,q,4} \leq d_{p,q,2}$  &  $d_{p,q,4} \leq d_{p,q,3})$  then  $\ell = 4$ 
  else
     $\ell = 2$ 
  end
else
  if  $(d_{p,q,4} \leq d_{p,q,2} \parallel d_{p,q,4} \leq d_{p,q,3})$  then  $\ell = 4$ 
  elseif  $(d_{p,q,2} \leq d_{p,q,3}$  &  $d_{p,q,2} \leq d_{p,q,4})$  then  $\ell = 2$ 
  else
     $\ell = 3$ 
  end
end
end

```

ALGORITHM 1: Algorithm of adaptive path number selection mechanism for $L = 4$.

are used to estimate $(\widehat{\mathbf{h}}_{p,q})_{L \times 1}$. In the second step, the preliminary estimates of channel frequency response at pilot tones $(\widehat{\mathbf{H}}_{p,q}^\ell)_{L \times 1}$ for $\ell = 2, 3, \dots, L$ are obtained from (19), and in the third step, the fine correction factors at pilot tones $(C_{p,q}^\ell)_{L \times 1}$ are obtained from (20), and the fine channel frequency response estimations $(\widehat{\mathbf{H}}_{p,q}^\ell)_{N \times 1}$ are determined by (24), (25), and (26). In the fourth step, the estimated channel frequency transfer function $(\widehat{\mathbf{H}}_{p,q}^{\text{long}})_{N \times 1} = \{\widehat{H}_{p,q,k}^{\text{long}}, k = 0, 1, \dots, N - 1\}$ obtained from two continuous long training symbols, which are defined in [9], is compared with the fine channel estimation for path number selection. The difference values between the fine estimations of channel frequency response $(\widehat{\mathbf{H}}^\ell)_{N \times 1}$ and $(\widehat{\mathbf{H}}_{p,q}^{\text{long}})_{N \times 1} = \{\widehat{H}_{p,q,k}^{\text{long}}, k = 0, 1, \dots, N - 1\}$ are compared with two times of noise variance of the MIMO-OFDM receiver, respectively. The total number of counts $c_{p,q,\ell}$ which satisfy the condition of $\widehat{H}_{p,q,k}^\ell - \widehat{H}_{p,q,k}^{\text{long}} < 2\sigma_s^2$ is calculated:

$$\begin{aligned}c_{p,q,\ell} &= \text{Num} \left(\widehat{H}_{p,q,k}^\ell - \widehat{H}_{p,q,k}^{\text{long}} < 2\sigma_s^2 \text{ (threshold)}, \right. \\ &\quad \left. \text{for } k = 0, 1, \dots, N - 1 \right), \quad (30) \\ &\quad \text{for } \ell = 2, 3, \dots, L,\end{aligned}$$

where $2\sigma_s^2$ is defined as the threshold of $(\widehat{\mathbf{H}}_{p,q}^\ell)_{N \times 1} - (\widehat{\mathbf{H}}_{p,q}^{\text{long}})_{N \times 1}$. With reference to the algorithm of adaptive path number selection mechanism listed in Algorithm 1

TABLE 1: Six-path OFDM channel model.

Path number	Tap number	Tap power (dBm), K	Path power (dBm)	Excess delay (n s)	Path K factor	Freq. offset (f_d) in Hz	Spectrum half-width (f_f) in Hz	Spectrum shape
1	1	0, 102	-0.0424	0	0	264.6	—	Freq. shift
2	1		-24.892	0	0	-75.6	476.3	Rounded
3	1		-21.892	0	0	-37.8	1001.7	Flat
4	2	-6.5	-6.5	50	7.3	0	1088.6	Rounded
5	3	-14.4	-14.4	100	4.7	0	1266.3	Rounded
6	4	-17.5	-17.5	150	3.6	0	1266.3	Rounded

for $L = 4$, $d_{p,q,2}$, $d_{p,q,3}$, \dots , and $d_{p,q,L}$ are defined as the MSE between $(\widehat{\mathbf{H}}_{p,q}^\ell)_{N \times 1}$ and $(\widehat{\mathbf{H}}_{p,q}^{\text{long}})_{N \times 1}$ and given by

$$d_{p,q,\ell} = E \left\{ \left\| \widehat{\mathbf{H}}_{p,q,N \times 1}^\ell - \widehat{\mathbf{H}}_{p,q,N \times 1}^{\text{long}} \right\|^2 \right\}, \quad \text{for } \ell = 2, 3, \dots, L. \quad (31)$$

The number of paths can be adaptively selected for the largest $c_{p,q,\ell}$ and the smallest $d_{p,q,\ell}$ in the first OFDM data block or in each of the OFDM data blocks.

4. Simulation Results

The function of the proposed adaptive path number selection mechanism is simulated in MIMO-OFDM fading channel. The features for a mobile OFDM system include a bandwidth of 10 MHz and 64 subcarriers, the measured signal interval $T_m = \text{packet time} = 840 \mu\text{sec}$. Each transmitted packet contains 100 OFDM data blocks; the path number selections are conducted at the first data blocks. Four equally spaced pilot subcarriers, which are inserted in the positions of 8th, 24th, 40th, and 56th subcarriers in an OFDM data block, are applied for each of the transmitted OFDM data blocks. The six-path channel model listed in Table 1, where the first three paths have no path delay and the interpath delay time after path three is 50 nsec, is employed to simulate mobile OFDM performance, so that $L = 4$.

Two-ray Rayleigh fading channel and six-path fading channel with 13 nsec delay spread are used to test the bit error rate (BER) performance of the OFDM transceiver. In Figure 2, two-ray Rayleigh fading channel is used to validate six-path fading channel with 13 nsec delay spread. Figure 2(a) shows the BER performance of OFDM transceiver using 16-QAM. Figure 2(b) shows the BER performance of OFDM transceiver using 64-QAM. For demonstration we have chosen 120 km/hr and 200 km/hr; performance for high speed, that is, 200 km/hr, seems to degrade than the performance for system with less speed, that is, 120 km/hr, because at higher speed the channel behaves as a fast fading channel and for slower speed channel behaves as a slow fading channel [8]. The test results show that the BER performance of the OFDM transceiver in the high-speed time-varying fading channel will be reduced to less than 10^{-5} at the minimum SNR of 12 dB for 16-QAM and 28 dB for 64-QAM at 120 Km/hr. For 200 Km/hr user speed, the performance of 64-QAM OFDM

transceiver over six-path fading channel with 13 nsec delay spread degrades to unacceptable levels.

For the purpose of the diversity gain, a simple 2×2 SFBC is combined with the OFDM system, where the adaptive path number selection mechanism is employed for each transmit-receive antenna pair. Let two frequency-domain data signals at two consecutive subcarriers be encoded using Alamouti code and transmitted from two antennas. Since the channel response for that subcarrier within one SFBC block is stationary, then the maximum-likelihood symbol detector is used to detect the transmitted symbols.

The BER performance of the 2×2 SFBC-OFDM system in terms of 16-QAM and 64-QAM modulations over the six-path fading channel with 13 nsec and 26 nsec delay spread is shown in Figures 3 and 4, respectively, where the user speed is set as 200 km/h. The calculations of 13 nsec and 26 nsec root mean square (rms) delay spread are shown in the appendix. For OFDM system, the channel is frequency nonselective fading if the delay spread is in the range of (0, 20 nsec), and the channel is frequency selective fading if the delay spread exceeds 20 nsec [8]. It is observed that the acceptable BER ($<10^{-5}$) for QAM modulated MIMO-OFDM systems operated in fast-varying fading channels can always be achieved by employing the proposed path number selection mechanism. In Figure 4(a), the BER value of the 16-QAM modulated MIMO-OFDM systems employing the proposed path number selection mechanism over frequency nonselective fast fading channels with 13 nsec delay spread is lower than $\ell = 4$ and slightly higher than $\ell = 2$ and 3 in the region of interest ($\text{BER} < 10^{-5}$). The required E_b/N_0 for the acceptable BER is low for all cases. It indicates that the MIMO mode is not necessary to be used for the 16-QAM OFDM systems when the delay spread is small. In Figure 4(b), the gain of the 64-QAM modulated MIMO-OFDM system employed the proposed adaptive path number selection mechanism in frequency nonselective fast fading channel with 13 nsec delay spread exceeds 1 dB compared with $\ell = 4$, and its BER value is slightly higher than $\ell = 2$ and 3 in the region of interest. In frequency nonselective fast fading channel, choosing smaller number of paths can get the smaller mean square error in channel impulse response estimate. Figure 4 shows that the BER value of the QAM modulated MIMO-OFDM systems employing the proposed path number selection mechanism over frequency selective fast fading channels with 26 nsec delay spread is lower than $\ell = 2$ and 3 and slightly higher than $\ell = 4$ in the region

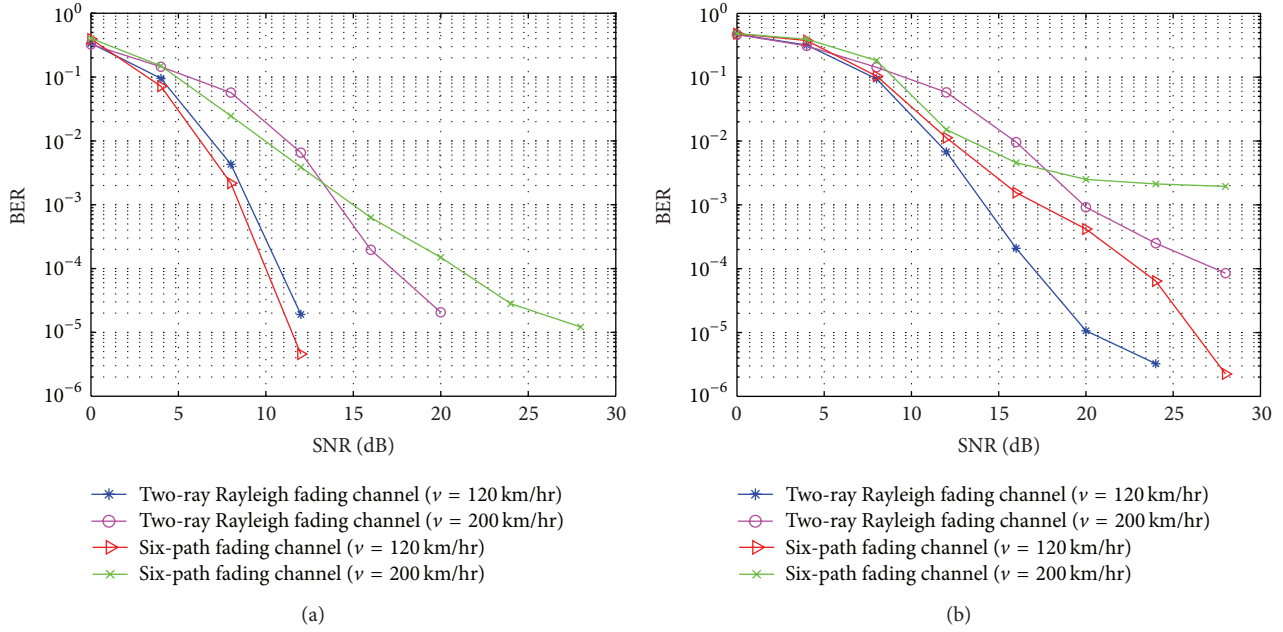


FIGURE 2: BER of the OFDM transceiver over two-ray Rayleigh fading channel and six-path fading channel with 13 nsec delay spread for (a) 16-QAM and (b) 64-QAM.

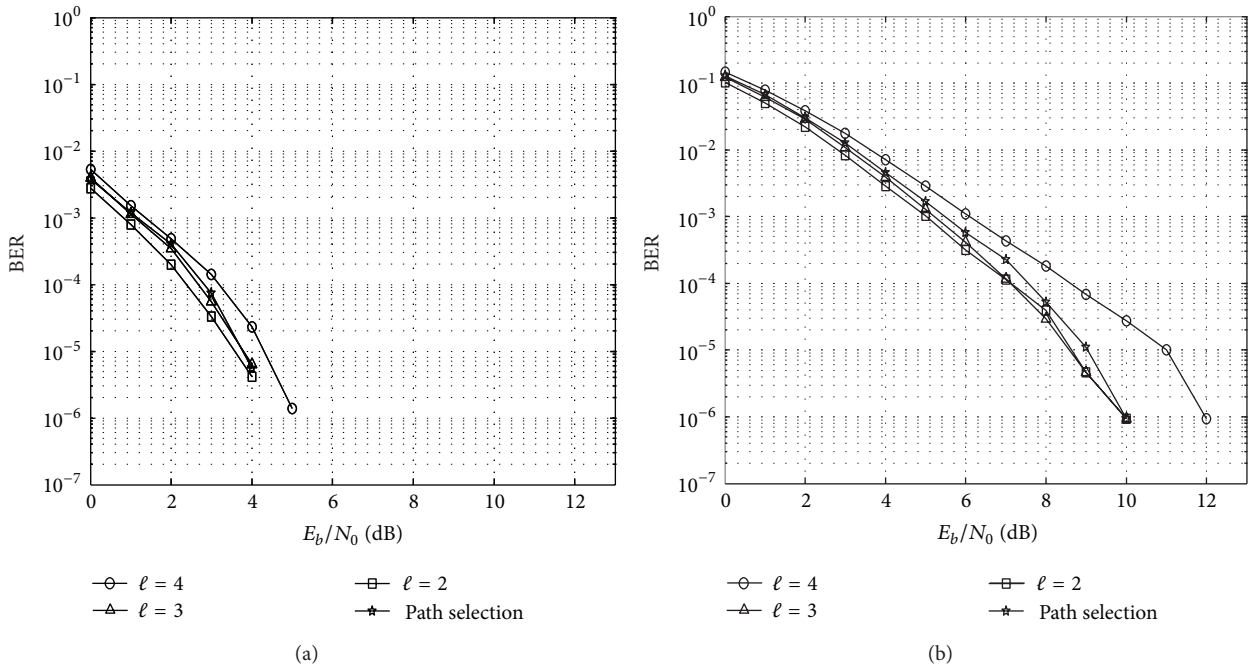
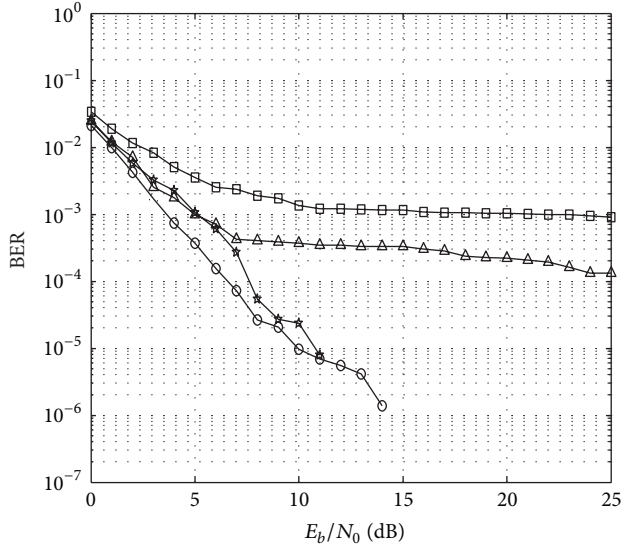


FIGURE 3: BER performance of 2×2 SFBC-OFDM system over the six-path fading channel with 13 nsec delay spread for (a) 16-QAM modulation and (b) 64-QAM modulation.

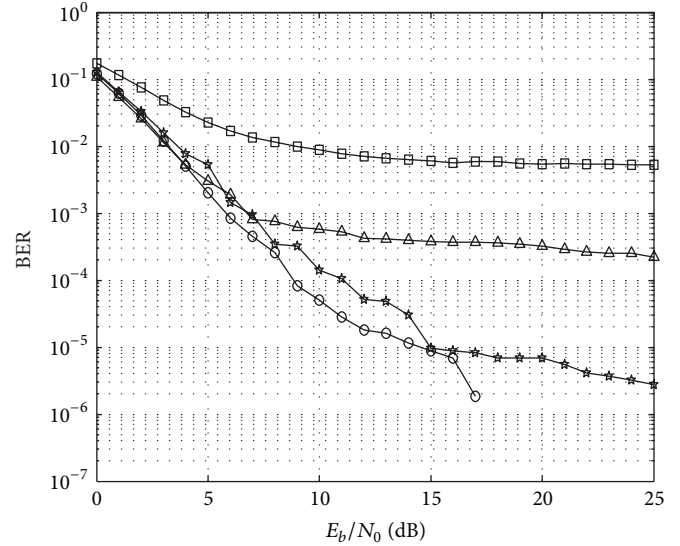
of interest. The error floors of the BER performance appear at an E_b/N_0 of about 8 dB for 16-QAM (curve $\ell = 2$) and about 15 dB for 64-QAM (curves $\ell = 2$ and 3), respectively. The frequency selectivity of the multipath fading channel increases with its delay spread. In a frequency selective fast fading channel, the BER of the MIMO-OFDM decreases with an increase of the path number due to more linear

interpolation loss are generated by using less path number in frequency selective fast fading channel. By examining Figures 3 and 4, it is concluded that the pilot-based channel estimate using the proposed path number selection mechanism at the first data block can satisfy the OFDM system performance requirements under different operating conditions of time-varying fast fading channels.



\circ $\ell = 4$ \square $\ell = 2$
 \triangle $\ell = 3$ \star Path selection

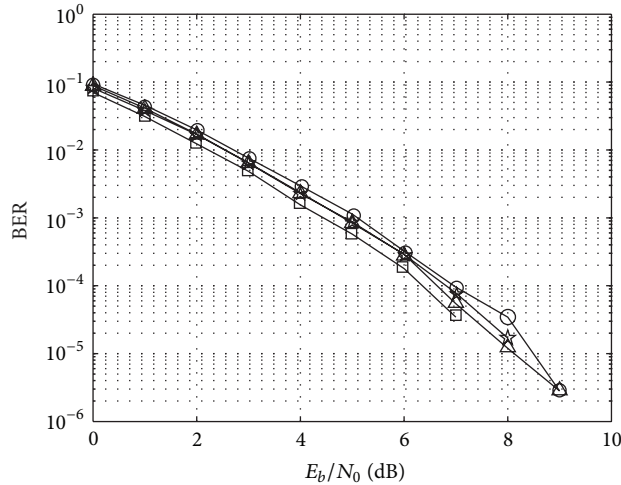
(a)



\circ $\ell = 4$ \square $\ell = 2$
 \triangle $\ell = 3$ \star Path selection

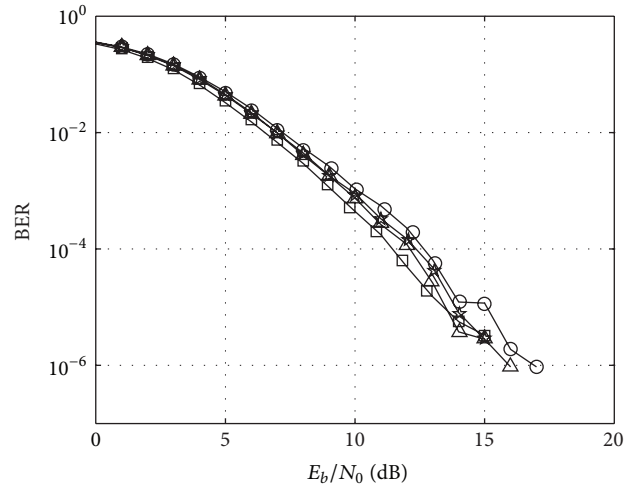
(b)

FIGURE 4: BER performance of 2×2 SFBC-OFDM system over the six-path fading channel with 26 nsec delay spread for (a) 16-QAM modulation and (b) 64-QAM modulation.



\circ $\ell = 4$ \square $\ell = 2$
 \triangle $\ell = 3$ \star Path selection

(a)



\circ $\ell = 4$ \square $\ell = 2$
 \triangle $\ell = 3$ \star Path selection

(b)

FIGURE 5: BER performance of OFDM system over the six-path fading channel with 13 nsec delay spread for (a) 16-QAM modulation and (b) 64-QAM modulation.

In Figure 5, the BER value of the QAM modulated OFDM system employing the proposed path selection mechanism over time-varying fading channels with 13 ns delay spread is lower than $\ell = 4$ and slightly higher than $\ell = 2$ and 3.

Figure 6 shows that the BER value of the QAM modulated OFDM systems employing the proposed path selection mechanism over time-varying fading channels with 26 ns delay spread is lower than $\ell = 2$ and 3 and slightly higher

than $\ell = 4$. The frequency selectivity of the multipath fading channel increases with its delay spread.

5. Conclusions

An adaptive path number selection mechanism is proposed to improve the accuracy of the pilot-based channel estimation approach for QAM modulated MIMO-OFDM systems

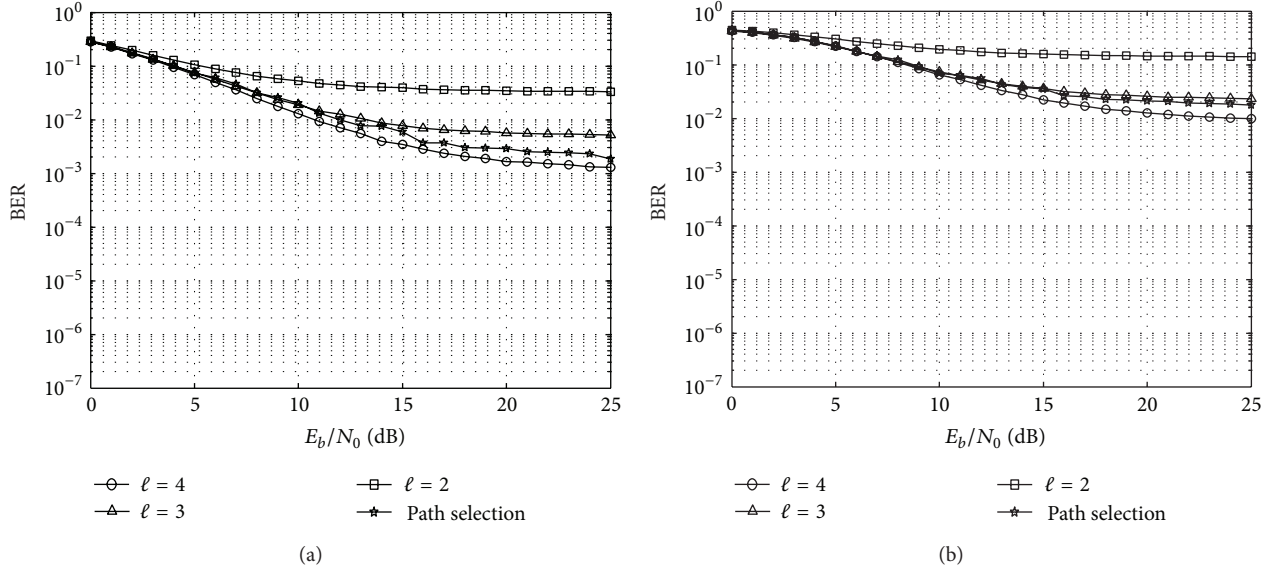


FIGURE 6: BER performance of OFDM system over the six-path fading channel with 26 nsec delay spread for (a) 16-QAM modulation and (b) 64-QAM modulation.

operating in time-varying fast fading channels. The fine correction factors are derived. It is demonstrated that the number of paths is scalable and adaptively changed with the characteristics of time-varying MIMO-OFDM fading channels to provide a suboptimum BER performance for QAM modulated 2×2 SFBC-OFDM systems operated either in frequency nonselective fast fading or in frequency selective fast fading channels.

Appendix

Calculations of Delay Spread 26 nsec and 13 nsec [8]

The fading channel generator at the i th path consists of two nonline-of-sight (NLOS) branches and a LOS branch. In NLOS branch, two independent and identically distributed (iid) Gaussian signal sources are connected to identical Doppler filters. The channel weighing factor $w_i[k']$ is determined by

$$w_i[k] = P_i (s_{i_NLOS}[k] + s_{i_LOS}[k]), \quad k = 1, 2, \dots, N, \quad (\text{A.1})$$

where the output of NLOS branch at the i th path in the fading channel weighing generator is

$$s_{i_NLOS}[k] = y_i[k] \times \left(\frac{1}{\sqrt{1+k_i}} \right), \quad k = 1, 2, \dots, N, \quad (\text{A.2})$$

where

$$y_i[k] = \left(\sum_{l=-\infty}^{\infty} x_1[l] \hat{h}_i[k-l] \right) + j \left(\sum_{l=-\infty}^{\infty} x_2[l] \hat{h}_i[k-l] \right) \quad k = 1, 2, \dots, N. \quad (\text{A.3})$$

x_1 and x_2 are independent Gaussian functions, and \hat{h}_i is impulse response of Doppler filter. The output of LOS branch at i th path in the fading channel weighing generator is

$$s_{i_LOS}[k] = \sqrt{\frac{k_i}{1+k_i}} \times \exp \left(j2\pi (f_{d_i} \cos \theta_i + f_{o_i}) \frac{k}{f_{s,dop}} \right) \quad k = 1, 2, \dots, N. \quad (\text{A.4})$$

Furthermore, $w_i[k]$ is interpolated by factor I to get the sequence $v_i[k']$ with sampling rate $f_{sig} = I \times f_{s,dop}$:

$$v_i[k'] = \begin{cases} w_i \left[\frac{k'}{I} \right] & k' = I, 2I, \dots, NI \\ 0 & \text{otherwise.} \end{cases} \quad (\text{A.5})$$

The image signal of $v_i[k']$ is removed by an interpolation low pass filter with unit impulse response $h_I[k']$. The interpolated fading envelop signal $r_i[k']$ is stored in the register bank as

$$r_i[k'] = \sum_{l=-\infty}^{\infty} v_i[l] h_I[k-l], \quad k' = 1, 2, \dots, NI, \quad (\text{A.6})$$

where the sampling interval of $r_i[k']$ is

$$\Delta t = \frac{1}{f_{\text{sig}}}. \quad (\text{A.7})$$

The parameters listed in Table 1 represent for rms delay spread $\tau_{\text{rms}} = 23$ nsec. As an example steps involved in the calculation of $\tau_{\text{rms}} = 23$ nsec using the values in Table 1 will be shown. From Table 1, the Tap powers (P_i) are 0 dB, -6.5 dB, -14.4 dB, and -17.5 dB at Excess delay 0 nsec, 50 nsec, 100 nsec, and 150 nsec, respectively. We first normalize these Tap powers to get values 0.9751 W, 0.2183 W, 0.0354 W, and 0.0173 W at Excess delay 0 nsec, 50 nsec, 100 nsec, and 150 nsec respectively.

Normalized tap delay powers are weighed using weighing factor $w_i[k']$. As an example, if weighing factors were found to be 0.7099-0.4263i, -0.6830-0.3211i, -0.393-0.4039i, and -0.0443-0.0841i for excess delay at 0 ns, 50 ns, 100 ns, and 150 ns, respectively. Taking the absolute values for the tap delay power and the weighing factor we get final tap powers 0.8074, 0.1648, 0.0200, and 0.0016 at Excess delay 0 nsec, 50 nsec, 100 nsec and 150 nsec, respectively thus, calculating rms delay spread using (A.8) [12]:

$$\tau_{\text{drms}} = \sqrt{\overline{\tau^2} - (\bar{\tau})^2}, \quad (\text{A.8})$$

where the mean excess delay $\bar{\tau}$ is defined as

$$\bar{\tau} = \frac{\sum_k a_k^2 \tau_k}{\sum_k a_k^2} = \frac{\sum_k P(\tau_k) \tau_k}{\sum_k P(\tau_k)} \quad (\text{A.9})$$

and $\overline{\tau^2}$ is defined as

$$\overline{\tau^2} = \frac{\sum_k a_k^2 \tau_k^2}{\sum_k a_k^2} = \frac{\sum_k P(\tau_k) \tau_k^2}{\sum_k P(\tau_k)}. \quad (\text{A.10})$$

Similarly, tap powers 0 db, -18.5 dB, -21.4 dB, and -24.5 dB for Excess delay 0 ns, 50 ns, 100 ns, and 150 ns, respectively, for $\tau_{\text{rms}} = 13$ nsec and tap powers 0 db, -6.5 dB, -7.5 dB, and -8.5 dB for Excess delay 0 ns, 50 ns, 100 ns, and 150 ns, respectively, for $\tau_{\text{rms}} = 26$ nsec.

Acknowledgment

This work is supported in part by research grants from National Science Council, Taiwan (NSC 102-2218-E-155-001).

References

- [1] S. R. Saunders and A. A. Zavala, *Antennas and Propagation for Wireless Communication Systems*, John Wiley & Sons, 2nd edition, 2007.
- [2] T. D. Chiueh and P. Y. Tsai, *OFDM Baseband Receiver Design for Wireless Communications*, John Wiley & Sons, 2007.
- [3] J. Chen, Y. Tang, and S. Li, "Analysis and optimization of pilot-symbol-assisted M-OAM for OFDM systems," *Wireless Communications and Mobile Computing*, vol. 5, no. 1, pp. 15–22, 2005.
- [4] O. Simeone, Y. Bar-Ness, and U. Spagnolini, "Pilot-based channel estimation for OFDM systems by tracking the delay-subspace," *IEEE Transactions on Wireless Communications*, vol. 3, no. 1, pp. 315–325, 2004.
- [5] M. Torabi, S. Aissa, and M. R. Soleymani, "On the BER performance of space-frequency block coded OFDM systems in fading MIMO channels," *IEEE Transactions on Wireless Communications*, vol. 6, no. 4, pp. 1366–1373, 2007.
- [6] I. Cosovic and G. Auer, "Capacity of MIMO-OFDM with pilot-aided channel estimation," *Eurasip Journal on Wireless Communications and Networking*, vol. 2007, Article ID 32460, 2007.
- [7] J. Kim, R. W. Heath Jr., and E. J. Powers, "Receiver designs for Alamouti coded OFDM systems in fast fading channels," *IEEE Transactions on Wireless Communications*, vol. 4, no. 2, pp. 550–559, 2005.
- [8] J. Mar, C.-C. Kuo, Y.-R. Lin, and T.-H. Lung, "Design of software-defined radio channel simulator for wireless communications: case study with DSRC and UWB channels," *IEEE Transactions on Instrumentation and Measurement*, vol. 58, no. 8, pp. 2755–2766, 2009.
- [9] "Standard Specification for Telecommunications and Information Exchange Between Roadside and Vehicle System—5Ghz Band Dedicated Short Range Communications (DSRC) Medium Access Control (MAC) and Physical Layer (PHY) Specifications," IEEE 802, December 2005.
- [10] R. Negi and J. Cioffi, "Pilot tone selection for channel estimation in a mobile ofdm system," *IEEE Transactions on Consumer Electronics*, vol. 44, no. 3, pp. 1122–1128, 1998.
- [11] J. Rinne and M. Renfors, "Pilot spacing in Orthogonal Frequency Division Multiplexing systems on practical channels," *IEEE Transactions on Consumer Electronics*, vol. 42, no. 4, pp. 959–962, 1996.
- [12] T. S. Rappaport, *Wireless Communications: Principles and Practice*, Prentice Hall, 2nd edition, 2002.